UNIVERSITY OF LJUBLJANA
FACULTY OF MATHEMATICS AND PHYSICS

Dejan Žontar

Study of radiation damage in silicon detectors for high luminosity experiments at LHC

Doctoral Thesis

Supervisors: prof. dr. Aleš Stanovnik
doc. dr. Marko Mikuž

Ljubljana, 1998

UNIVERZA V LJUBLJANI
FAKULTETA ZA MATEMATIKO IN FIZIKO

Dejan Žontar

Študij sevalnih poškodb silicijevih detektorjev za eksperimente z visoko luminoznostjo na trkalniku LHC

Disertacija

Mentor: prof. dr. Aleš Stanovnik
Somentor: doc. dr. Marko Mikuž

Ljubljana, 1998

Najprej gre moja zahvala delovnima mentorjema doc. dr. Vladimirju Cindru in doc. dr. Marku Mikužu. Prvi mi je s svojimi bogatimi izkušnjami z eksperimentalnim delom nudil neprecenjilvo pomoč predvsem v postavitvi eksperimenta ter načrtovanju in izvajanju meritev. Drugemu se še posebej zahvaljujem za neskončne pogovore o intrepretaciji rezultatov in njihovih posledicah. Brez njune pomoči in potrpežljivosti to delo gotovo ne bi bilo mogoče.

Univerzitetnemu mantorju prof. dr. Alešu Stanovniku se zahvaljujem za večkratno nadvse pozorno branje predstavljenega dela in številne koristne pripombe. S svojim širokim pogledom je gotovo močno pripomogel k celoviti predstavitvi opravljenega dela.

Seveda ne smem pozabiti mag. Gregorja Krambergerja, ki je prispeval levji delež pri vzpostavitvi računalniškega nadzora nad meritvami. Hkrati se zahvaljujem tudi Eriku Marganu, ki je s svojim globokim a praktičnem poznavanjem elektronike, zgradil vse manjše elektronske komponente, potrebne za nemoten potek poskusov.

To delo ne bi bilo mogoče tudi brez sodelovanja osebja reaktorskega centra v Podgorici. Mag. Marku Maučecu se zahvaljujem za simulacijo nevtronskega spektra v obsevalnem kanalu F19, ing. Edvardu Krištofu pa za meritve spektra in nevtronsko dozimetrijo. Operaterjem reaktorja, med njimi še posebej Bojanu Omanu, se zahvaljujem za izjemno sodelovanje in prilagajanje svojega delovnega časa potrebam obsevanj.

I would also like to thank A. Vasilescu for sending me data for Ougouag damage function and cross-checking my results with both Ougouag and Griffin values. My thanks also go to F. Lemmeilleur, who kindly provided MESA samples and helped with disscussion of results, obtained after their irradiation.

Nenazadnje pa se moram zahvaliti vsem sodelavcem odseka za eksperimentalno fiziko osnovnih delcev za izjemno delovno vzdušje in vzorne medsebojne odnose, katerih je deležen le redko kdo.

Abstract

Radiation damage of the silicon bulk will play an important role in the vertex detectors in the future experiments at LHC. To study its macroscopic effects, high resistivity p^+-n-n^+ diodes were irradiated with neutrons at the TRIGA research reactor of Jožef Stefan Institute in Ljubljana. Irradiation fluences were in the range from 10^{13} to $2.5{\cdot}10^{14}$ /cm^2 of equivalent 1 MeV neutrons. Development of effective doping concentration and reverse current during and after irradiations was studied under controlled conditions (bias, temperature).

Long term annealing of effective doping concentration was studied to determine the dynamics of the process responsible. Results obtained from a set of unbiased diodes kept at 20°C gave conslusive evidence that, at least during the initial stage, time development can be described by a first order process.

Flux dependence of defect creation has been checked in the flux range from $2{\cdot}10^8$ to $\approx 5{\cdot}10^{15}$ n/cm^{2}s. No significant difference among the samples was observed in any of the studied properties.

Influence of bias voltage on defect development was discovered. Fully biased samples were found to have about a factor 2 higher values of N_{eff} after beneficial annealing. After removal of bias, the difference anneals out exponentialy with two time constants of about 40h and 6 weeks at 20°C. No influence of bias voltage on reverse current was observed.

Keywords: silicon detectors, radiation hardness, neutron irradiation, LHC

PACS 29.40.Gx, 29.40.Wk

Povzetek

Sevalne poškodbe v siliciju bodo znatno vplivale na delovanje verteks detektorjev v bodočih eksperimentih na velikem hadronskem trkalniku LHC. Pričujoče delo obsega rezultate obsevanj visoko upornostnih p^+-n-n^+ diod v reaktorju TRIGA Instituta Jožef Stefan pri Ljubjani. Obsevalne fluence so bile ekvivalentne 10^{13} do $2.5{\cdot}10^{14}$ n/cm^2 1 MeV nevtronom. Pod nadzorovanimi pogoji sem spremljal razvoj efektivne koncentracije dopantov in zapornega toka tako med kot tudi po obsevanju.

Meritve počasnega razvoja efektivne koncentracije dopantov so bile namenjene določanju dinamike odgovorne reakcije. Dobljeni rezultati meritev diod, ki so bile hranjene pri 20°C brez napajalne napetosti, so dal1 prepričljive dokaze, da lahko razvoj vsaj v začetni fazi popišemo s procesom prvega reda.

Odvisnost tvorjenja poškodb od nevtronskega fluksa sem preverili za flukse med $2{\cdot}10^8$ in $\approx 5{\cdot}10^{15}$ n/cm^{2}s. V raziskanem področju med vzorci ni bilo opaznih razlik, ki bi jih lahko pripisali razlikam v fluksu.

V okviru dela je bil odkrit vpliv napajalne napetosti na časovni razvoj poškodb. Vpliv se odraža kot razlika v efektivni koncentraciji dopantov. Ta je za vzorce pod polno deplecijsko napetostjo po končanem okrevanju približno dvakrat večja kot za vzorce brez napetosti. Upadanje razlike po izklopu napetosti lahko popišemo z dvema eksponentnima funkcijama s časovnima konstantama okoli 40 ur in 6 tednov pri 20°C. Rezultati kažejo, da na razvoj zapornega toka prisotnost napajalne napetosti nima zaznavnega vpliva.

Ključne besede: silicijevi detektorji, sevalne poškodbe, nevtroni, LHC

PACS 29.40.Gx, 29.40.Wk

Contents

1

Introduction

Silicon detectors play an essential role in modern particle physics experiments. They exhibit fast and linear response to ionising particles, are compact and have good energy resolution. Highly developed techniques of semiconductor processing allow production of complex structures on a micron scale. Silicon detectors are thus an obvious choice for compact and fast tracking detectors with supreme spatial resolution[1] and are a part of basically all modern particle physics detectors. They are usually used as the innermost part of tracking systems and play a crucial role in reconstruction of interaction vertices.

In the first decade of the next millennium the Large Hadron Collider (LHC) [2] (figure 1.1) will be in operation at the European laboratory for particle physics (CERN). It will provide high energy (14 TeV) proton-proton collisions with high luminosity ($10^{33}/\mathrm{cm}^2\mathrm{s}$ during low and $10^{34}/\mathrm{cm}^2\mathrm{s}$ during high luminosity running). This opens a wide range of physics opportunities, among which the origin of mass is a major focus of interest. One of the possible manifestations of the spontaneous symmetry-breaking, responsible for the origin of mass, could be the existence of the Higgs boson. The ability to search for the Higgs boson is therefore used as a prime criterium in designing the detectors. Together with demands necessary for the study of some other processes (supersymmetry, B-physics) that will be accessible at LHC, it determines the basic design features of detectors at LHC [3, 4, 5]. Their main features are good electromagnetic calorimetry, efficient tracking at high luminosity, tau and heavy-flavour vertex reconstruction and stand-alone precision muon momentum measurements.

This work was done in scope of the ATLAS collaboration, which is building one of the large experiments at LHC. The overall design of the ATLAS detector (figure 1.2) is described in [4] and will not be discussed here. We shall only briefly describe the inner detector (ID) [6], used for charged particle tracking. A superconducting solenoid is

[1] Intrinsic resolutions as low as 1 μm were obtained with silicon strip detectors [1].

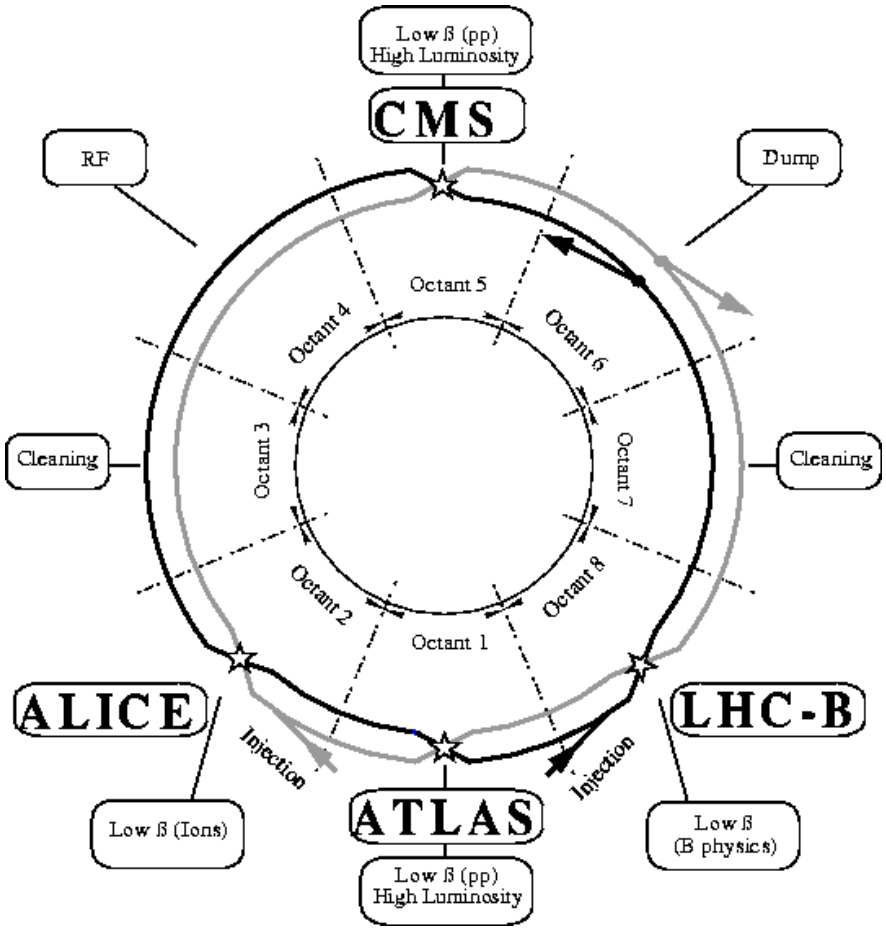

Figure 1.1: Schematic layout of the LHC.

contained within a cylinder of 6.8 m length and 1.15 m radius, with a magnetic field of 2 T. The inner detector provides pattern recognition, momentum and vertex measurements and electron identification. It consists of three parts (fig. 1.3). The outer part of the tracking volume contains the Transition Radiation Tracker (TRT), consisting of continuous straw-tube tracking detectors with transition radiation detection capability. The middle part (SCT - Semi-Conductor Tracker) consists of high-resolution semiconductor strip detectors, arranged in four concentric cylinders around the beam axis (Barrel SCT), and nine disks on each side (Forward SCT). Disks, used to cover the forward directions, are perpendicular to the beam axis. The Semi-Conductor Tracker covers radia from 30 to 52 cm. The innermost part consists of pixel detectors, arranged in three barrels at radii of 4, 11 and 14 cm, and four disks between radii of 11 and 20 cm on each side. Their two-dimensional segmentation gives unambiguous space points and the lower active area of an individual

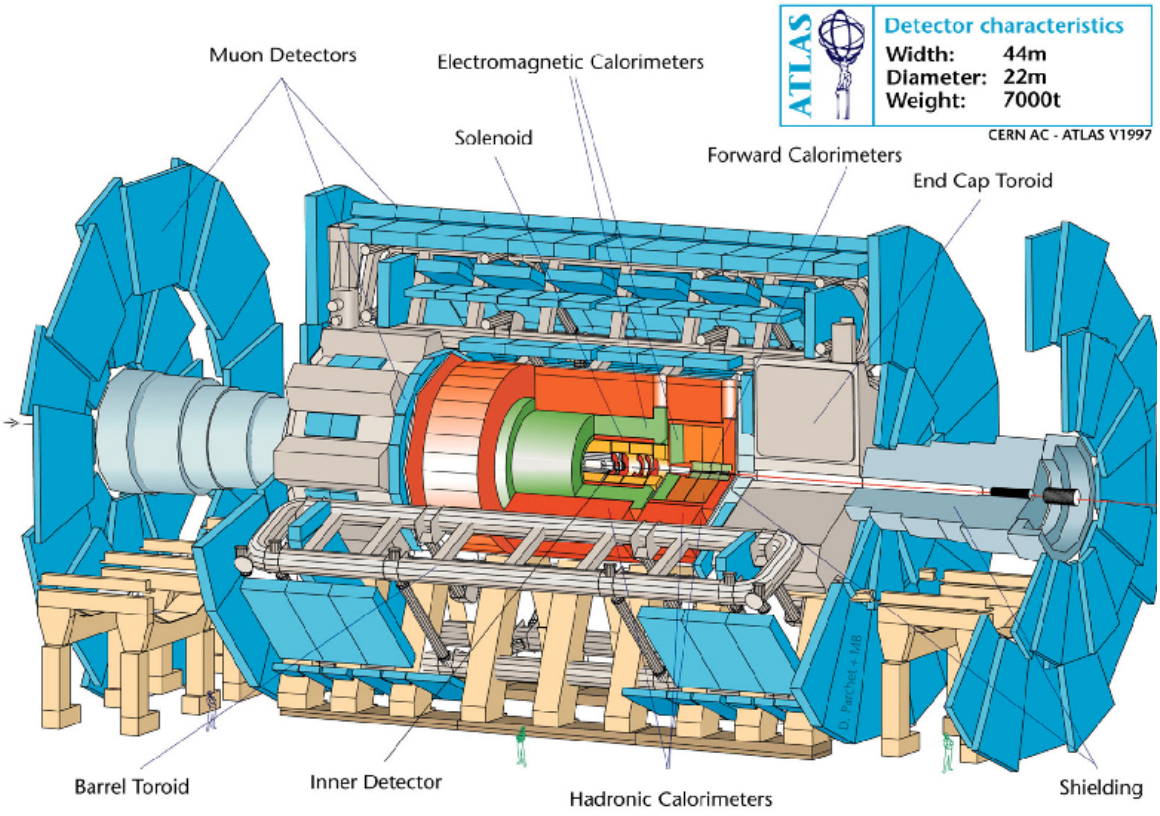

Figure 1.2: Schematic layout of the ATLAS detector.

segment provides better signal to noise ratio.

High luminosity and high interaction energy at the LHC will result in extremely high interaction rates. At maximum luminosity about 30 primary interactions will occur in every beam crossing (every 25 ns) producing several hundred secondary particles. This will result in significant radiation damage of the inner detector, especially for the layers at low radia. Results of the simulation of particle fluxes and estimated consequent damage of the silicon are presented in [6] and [7] . Radiation doses at the SCT radia are calculated to be around $1.5 \cdot 10^{13}$ equivalent 1MeV neutrons per cm^2 per year and 4 kGy/year[2] (fig. 1.4, 1.5). A careful study of radiation damage of silicon detectors is thus necessary to enable proper design and operation scenaria that will provide operation of the semiconductor tracker over 10 years of data-taking. A considerable effort of many groups has been already directed to this field.

[2]Numbers given are the typical values. Maximal values are estimated to $2 \cdot 10^{13}$ cm^2/year of 1 MeV neutrons equivalent and 10 kGy/year [6].

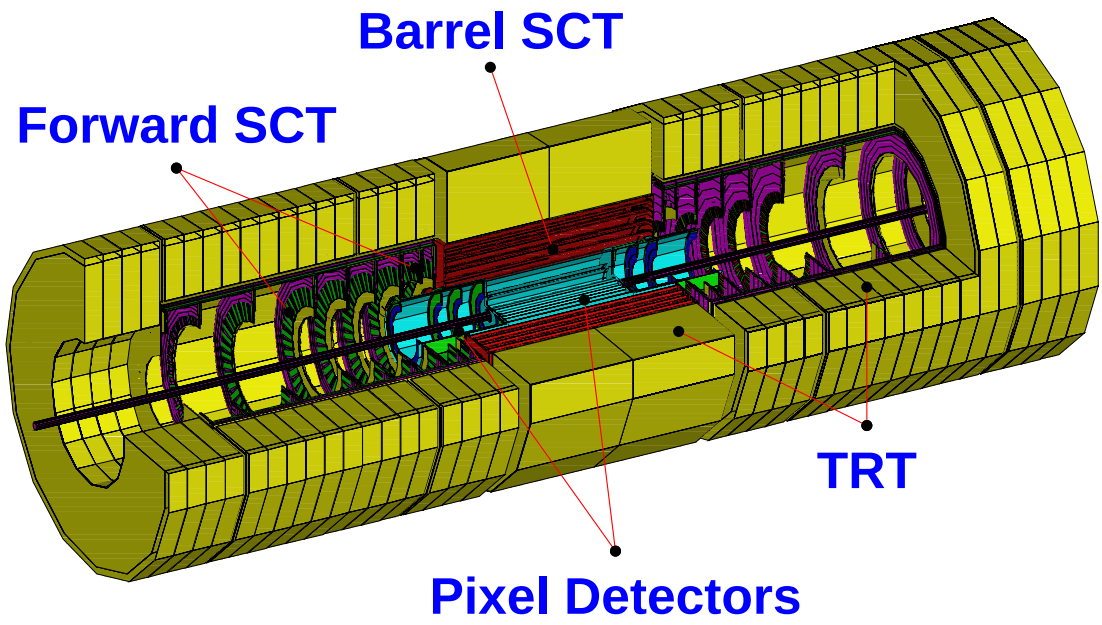

Figure 1.3: Schematic layout of the ATLAS Inner Detector (ID).

This work presents results obtained by the study of radiation induced defects of silicon bulk under controlled conditions. Biasing voltage and temperature were controlled during and after irradiations. Irradiation flux was varied from about 10^8 to few times 10^{15} n/cm^{2}s to search for a flux effect on defect creation. Frequent measurements of reverse current and full depletion voltage were performed during and immediately after the irradiation to provide better insight into fast defect annealing. Finally, a bias dependent defect annealing was discovered, resulting in about two times higher full depletion voltage of the biased samples after the end of beneficial annealing.

Radiation damage caused in silicon detectors can be separated to damage to silicon bulk and surface damage. The latter is mainly due to ionic charges, collected at the border between the semiconductor and the oxide. It increases the conductivity of the surface, giving rise to surface currents. Surface damage can also distort the field below the surface structures, thus changing the operation properties of a detector. It depends considerably on detector design and manufacturing, which have been well studied and understood. Thus the surface damage seems to be manageable. Bulk damage, on the other hand, is much less understood. It causes an increase of the leakage current and of the effective dopant concentration. This results in increased operation voltage, increased noise due to leakage current and increased power consumption and therefore heat. All those effects significantly influence the operational capability of a silicon detector.

Due to the interaction of radiation (n, p, π, e, γ etc.) with silicon atoms the

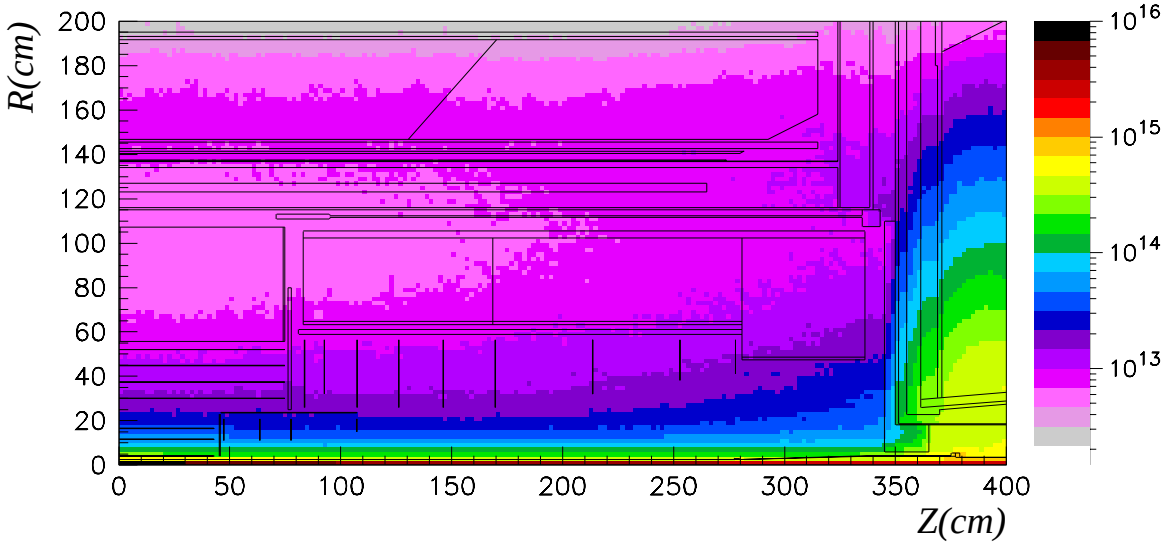

Figure 1.4: Flux in the inner detector cavity in units of 1 MeV equivalent neutrons per cm^2 per year [6].

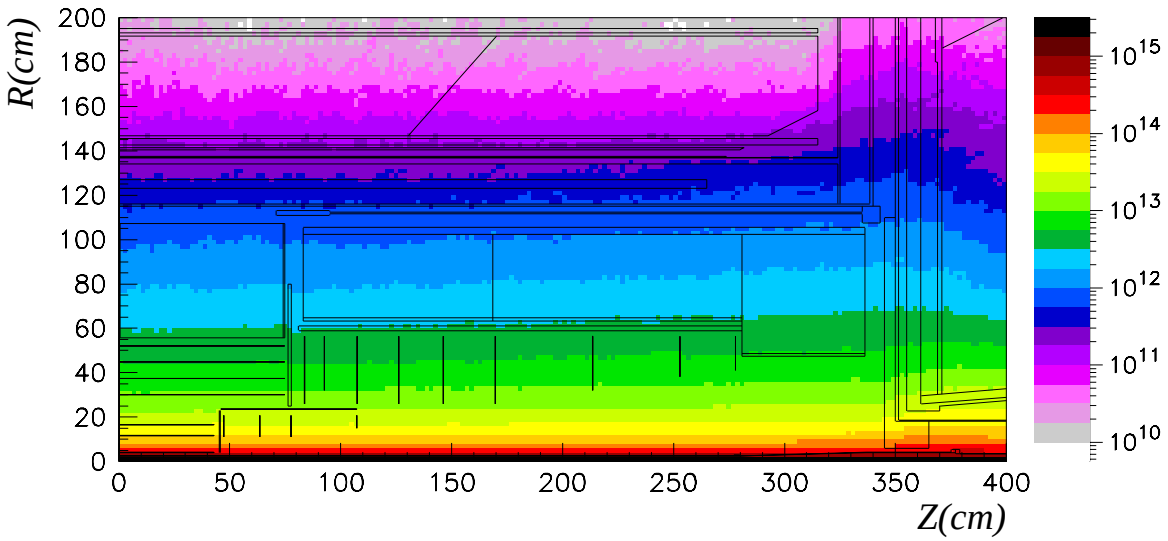

Figure 1.5: Flux of charged hadrons in the inner detector cavity per cm^2 per year [6].

periodic structure of the lattice is destroyed locally, i.e. silicon atoms are dislocated. A dislocated atom is called an interstitial atom, whereas the lattice site, being empty, is called a vacancy. The interstitials and vacancies form defect complexes which establish energy levels in the band gap. Most of the defect complexes contain impurity atoms e.g. carbon and oxygen. Since the detector operation is foreseen to last 10 years, the long term behaviour of bulk properties (effective doping concentration, reverse current) is of major concern. Understanding which type of defect causes the deterioration of performance is

very important in the attempt to build a radiation hard detector.

In the next chapter the basics of detector operation and a simple microscopic view of the defects as understood so far is presented. In the third part irradiation facilities at the TRIGA nuclear reactor that were developed as a part of this work are described. The fourth chapter is dedicated to time development of defects, where results on short term and reverse annealing are discussed. The fifth chapter presents results of the study of dose rate effect and in the last one results at the influence of detector bias on defect development are presented. The slovene summary is given after the conclusions and a list of symbols and abbreviations used in this work can be found in the appendix.

2

Operation and Radiation Damage of Silicon Detectors

2.1 Basics of Operation of Silicon Detectors

A silicon position-sensitive detector is an array of diodes on a silicon wafer. When reverse biased, it is operating like an ionisation chamber. Ionising particles passing a silicon detector generate electron-hole pairs along their paths. The number of pairs is proportional to the particles' energy loss. The creation of an electron-hole pair requires a mean energy of 3.6 eV with average energy loss in silicon of about 390 eV/μm for a minimum-ionising particle. For a typical detector thickness of about 300 μm, one obtains on average $3 \cdot 10^4$ electron-hole pairs, a signal detectable with low-noise electronics.

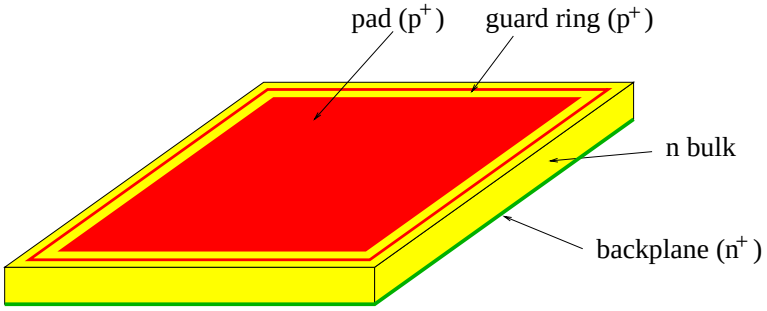

Figure 2.1: A schematic view of a pad detector. The highly doped p^+ pad and guard ring are shown on the p side of the diode.

As the emphasis of this study was in the radiation damage of the silicon bulk, silicon pad detectors (diodes) proved to be the ideal device. Simple processing provides good reproducibility and low cost. Simple structure of pad detectors (figure 2.1) strongly reduces the effects of surface radiation damage. Detectors consist of high resistivity bulk, highly n doped (n^+) on one side (backplane). The other (p) side consists of a large highly doped p^+ pad, often surrounded by one or more p^+ rings (guard rings). Due to simple

structure, surface damage of the top and bottom plane has a negligible effect[3] and the increase of the reverse current due to surface damage at the edge of detectors can be eliminated by guard rings.

The general equation

$$np = n_i^2 = N_C\, N_V e^{-\frac{E_g}{k_B T}} \tag{2.1}$$

is in the intrinsic case ($n = p = n_i$) giving the density of free carriers in non-depleted pure silicon. Here n and p are concentrations of free electrons and holes, respectively, N_C and N_V are effective densities of states at the conduction and valence band edges respectively

$$N_{C,V} = 2\left(\frac{2\pi m^*_{e,h} k_B T}{h^2}\right)^{\frac{2}{3}} \quad , \tag{2.2}$$

E_g=1.12 eV is the band gap, k_B the Boltzmann constant, h Planck constant, T temperature and $m^*_{e,h}$ effective masses of electrons and holes. At room temperature $N_{C,V}$ is of the order $10^{19}/\mathrm{cm}^3$ and n_i around $10^{10}/\mathrm{cm}^3$. In a 300 μm thick diode with an area of 1 cm^2 this gives a few times 10^8 of free carriers with fluctuations comparable to the signal from a minimum ionising particle ($3 \cdot 10^4$ pairs). In a reversely biased diode, on the other hand, free carriers are swept out by the electric field leaving a space charge region (SCR) depleted of free carriers.[4] Thus to obtain a good signal/noise ratio the active volume has to be depleted.

2.1.1 $p-n$ Junction

The number of free electrons and holes in silicon can be changed significantly by doping it with donors or acceptors. Donors usually are atoms that have in addition to the four electrons, needed for the covalent bond, one electron they donate to the conduction band. Acceptors have one electron missing to form bondings to all neighbours. So to complete the missing bond they accept an electron from the valence band, leaving a hole there. Energies needed for those transitions are comparable to $k_B T$ at room temperature and almost all dopants are ionised. Thus at high enough excess concentration of dopants of certain type, the number of electrons in the conduction band equals the number of donors or the number of holes in the valence band equals the number of acceptors. The relation $n_i^2 = n\,p$ still holds as in pure silicon, while $n = p = n_i$ is no longer valid. If the concentration of donors N_D exceeds the concentration of acceptors N_A (i.e. $n > p$)

[3] Single large pad reduces the surface of the oxide-bulk contact. Absence of integrated decoupling capacitors and bias resistors removes effects caused by radiation induced changes in their performances.

[4] In fact a small but permanent carrier generation due to emission and capture processes still remain in the SCR region as will be described later.

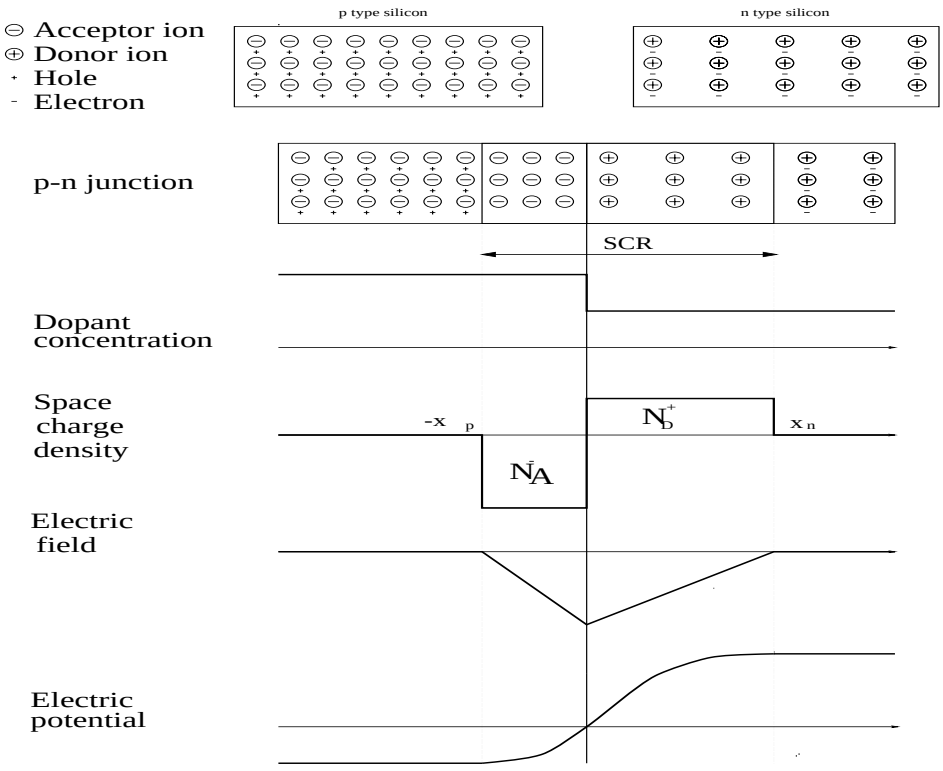

Figure 2.2: The p-n junction: dopant concentration, space charge density, electric field strength and electric potential.

the material is called n-type with electrons as majority carriers. If vice versa $N_A > N_D$ ($p > n$) the material is called p-type and majority carriers are holes. Standard doping elements are phosphorus and boron as a donor and an acceptor, respectively, with energy levels $\Delta E_C(P)$=0.044 eV [5] and $\Delta E_V(B)$=0.046 eV. [6]

When the dopant concentration changes from a surplus of acceptors N_A on the p-side to a surplus of donors N_D on the n-side the p-n junction is obtained (figure 2.2). The gradient of electron and hole densities results in a diffusive migration of majority carriers across the junction. This migration leaves the p region with a net negative charge and the n region with a net positive charge due to unneutralised, immobile acceptor and donor ions. This forms the space charge or depletion region. The immobile ions in the space charge region generate an electric field opposing the migration and thus an equilibrium is obtained in the system.

[5] Energy gap from the phosphorus energy level to the bottom of the conduction band.
[6] Energy gap from the top of the valence band to the boron level.

The electric properties of the junction can be calculated from the Poisson equation

$$-\frac{d^2V}{dx^2} = \frac{\rho_e(x)}{\epsilon_{Si}\epsilon_0} . \tag{2.3}$$

Assuming an abrupt junction

$$N_D(x) = \begin{cases} N_D, & x > 0 \\ 0, & x < 0 \end{cases} \qquad N_A(x) = \begin{cases} 0, & x > 0 \\ N_A, & x < 0 \end{cases} \tag{2.4}$$

one obtains solutions for the electric field and electric potential as shown in figure 2.2. The potential difference over the SCR with no external bias applied is called the built-in potential V_{bi}

$$V_{bi} = \frac{e_0}{2\epsilon_{Si}\epsilon_0}(N_D x_n^2 + N_A x_p^2) . \tag{2.5}$$

From the condition of electrical neutrality of the system it follows that the total positive and negative charge in the SCR have to be equal. It gives

$$N_A\, x_p \;=\; N_D\, x_n\,, \tag{2.6}$$

showing that the depth of depleted region on each side of the junction is inversely proportional to dopation.

For tracking detectors doping of one side (usually p side) is much higher than the other ($N_A \gg N_D$). Such p-n junction is also called a one-sided junction. In that case the depth of depleted region on p side is small compared to the depth on the weakly doped n side and the full depth of the depleted region w can be approximated with the depth on the weakly doped side ($w \approx x_n$). In that case one obtains

$$w = \sqrt{\frac{2\epsilon_{Si}\epsilon_0 V_{bi}}{e_0\, N_D}}. \tag{2.7}$$

Using [8]

$$V_{bi} = \frac{1}{e_0}\left[E_g + k_B T \ln(\frac{N_D N_A}{N_C N_V})\right] \tag{2.8}$$

one obtains V_{bi} of about 0.5-1 V. Together with $N_D \approx 10^{12}$ cm^{-3} for high resistivity silicon, the width of the depleted region for unbiased one-side junction can be estimated to few 10 μm.

2.1.2 Influence of External Voltage

For charged particle detection, the $e-h$ pairs created in the depletion region by a traversing particle are separated by the electric field, collected and read out. The charge created in the neutral, non-depleted region recombines with free carriers and is lost. Increasing the depth of the space charge region thus increases the collected signal.

To obtain maximal signal one would like to have the whole thickness of the detector depleted of free carriers. This can be achieved by applying an external voltage V with the same polarity as the built in potential. In that case V_{bi} in equation 2.7 is replaced by $V_{bi}+V$. Since usually $V \gg V_{bi}$, V_{bi} can be omitted and we obtain

$$w(V) = \sqrt{\frac{2\epsilon_{Si}\epsilon_0}{e_0 N_D} V} \ . \tag{2.9}$$

The voltage necessary to deplete the full depth of the detector (W), called the full depletion voltage (FDV or V_{FD}), is thus given by

$$V_{FD} = \frac{e_0 N_D W^2}{2\epsilon_{Si}\epsilon_0}. \tag{2.10}$$

It can be seen that the relation between V_{FD} and N_D depends quadratically on sample depth. For 300 μm thick samples, the conversion constant is $V_{FD} = 6.95 \cdot 10^{-11}\,\mathrm{Vcm}^3 \cdot N_D$.

For a semiconductor with both electrons and holes as carriers, bulk resistivity is given by [8]

$$\rho = \frac{1}{e_0(\mu_e n + \mu_h p)} \tag{2.11}$$

where μ_e and μ_h are electron and hole mobilities (1350 and 480 $\mathrm{cm}^2/\mathrm{Vs}$ at room temperature, respectively). For a fully ionised shallow-dopant n-type silicon, $n \approx N_D$ and $p \ll n$. Equation 2.11 can thus be simplified to

$$\rho = \frac{1}{e_0 \mu_e N_D} \ , \tag{2.12}$$

relating resistivity and initial donor concentration. For a typical value of $\rho = 5$ kΩcm one obtains $N_D \approx 9 \cdot 10^{11}\ \mathrm{cm}^{-3}$.

High resistivity n-type material ($\rho > 2$ kΩcm), that is usually used for the low doped n side of silicon tracking detectors, is obtained by donor compensation[7]. This means that donor and acceptor concentrations are of the same order of magnitude, and N_D has to be replaced by the difference of the donor and acceptor concentrations

$$N_D \rightarrow N_{eff} = |N_D - N_A| \ . \tag{2.13}$$

[7] Neutron doping is usually used to obtain high resistivity n-type material [8, 9].

2.1.3 The Fermi Level

The occupation probability for electrons is given by the Fermi-Dirac distribution function

$$f(E) = \left(1 + e^{\frac{E-E_F}{k_B T}}\right)^{-1} \tag{2.14}$$

For $E_C - E_F \gg k_B T$ (nondegenerate semiconductors) it converts to Boltzmann statistics, giving

$$n = N_C e^{-\frac{E_C - E_F}{k_B T}} \tag{2.15}$$

for the concentration of electrons in the conductive band [8]. Similary, for the concentration of holes in the valence band holds

$$p = N_V e^{-\frac{E_F - E_V}{k_B T}} \quad . \tag{2.16}$$

The Fermi level for the intrinsic case ($n = p = n_i$) can be determined from the charge neutrality condition

$$E_F(intrinsic) = E_i = \frac{E_C + E_V}{2} + \frac{k_B T}{2} \ln\left(\frac{N_V}{N_C}\right) \tag{2.17}$$

and the intrinsic carrier density is as given in eq. 2.1. It can be seen that in an intrinsic semiconductor the Fermi level lies very close to the middle of the bandgap.

In case of a **doped semiconductor** donor or acceptor impurities introduce new energy levels in the bandgap. To preserve charge neutrality in thermal equilibrium the Fermi level must adjust. Charge neutrality demands

$$n + N_A^- = p + N_D^+ \tag{2.18}$$

where N_D^+ and N_A^- are numbers of ionised donors and acceptors respectively. In a case of standard shallow level dopants (P,B) most dopants are ionised at room temperature, thus $N_D^+ \approx N_D$, $N_A^- \approx N_A$. The concentration of electrons and holes in an n type sample ($N_D > N_A$) follows from eq. 2.18 and 2.1 and for $N_D \gg N_A$ and $N_D - N_A \gg n_i$ the Fermi level equals

$$E_F = E_C - k_B T \ln\left(\frac{N_C}{N_D}\right) \tag{2.19}$$

with the equivalent equation

$$E_F = E_V + k_B T \ln\left(\frac{N_V}{N_A}\right) \tag{2.20}$$

for a p type semiconductor. For a 300 μm thick detector with full depletion voltage of 50 V ($\rho \approx 6\,k\Omega$cm) the donor concentration ($N_D \approx N_{eff}$) is about $7{\cdot}10^{11}/\mathrm{cm}^3$. Using $N_C{=}10^{19}/\mathrm{cm}^3$ (eq. 2.2) one gets E_F about 15 $k_BT{\approx}0.4$ eV below the conduction band, that is at about two thirds of the band gap ($E_g = E_C - E_V = 1.12eV$).

Trap occupancy in the **space charge region** is, as will be shown later, given by eq. 2.34. If we write it in a form of Fermi ocupancy probability

$$f_T = (1 + e^{\frac{2(E_T - E_F^T)}{k_B T}})^{-1} \tag{2.21}$$

we obtain the following value for a quasi Fermi level for a trap with energy E_T in the space charge region

$$E_F^T = E_i + \frac{k_B T}{2} \ln\left(\frac{\sigma_h^T}{\sigma_e^T}\right) \tag{2.22}$$

The ratio of the hole and electron trapping cross-section σ_h^T/σ_e^T is in most cases of the order 1, thus $E_F^T \approx E_i$. That means that traps below mid-gap are mainly occupied while traps above mid-gap are mainly unoccupied with the transition width of a few k_BT. Therefore donors contribute to the space charge if in the upper half of the energy gap and acceptors if in the lower half.

2.1.4 Diffusion Current from the Neutral Bulk

Bulk current running through the depleted region comes from two main contributions: diffusion of charge carriers from the non-depleted region (diffusion current) and generation of carriers in the depleted region (generation current). Besides these two sources a significant contribution can also come from the current running on the surface of a sample (surface current). It is mainly due to ionic charges at the semiconductor surface inducing surface channels, giving rise to the leakage current. It is strongly influenced by mechanical damage, humidity or other contamination of detector surface, and is thus hard to control. However, in an operating device the surface current is most often collected by a guard ring structure[8], making this contribution less critical. The derivation of both bulk-current contributions as compiled from [10], [8] and [11] is presented below. In this section the diffusion current will be discussed and the generation current is discussed in the next one.

The diffusion current describes the current through the p-n junction that is a consequence of diffusion of the carriers from the neutral region on one side to the neutral region on the other side. When no external voltage is applied the net current of the charge carriers (electrons and holes) through the junction sums to zero. This is not a consequence

[8]Guard ring structure is one or more p^+ rings (in a case of p on n device) surrounding the active region with a purpose of shielding it from the surface currents.

of the absence of carrier flow across the junction but only means that as many carriers of each type flow in one direction as in the other. In the presence of an external voltage V this however is not the case.

The diffusion current of a given carrier (e.g. holes) can be divided into two components: diffusion generation current and recombination current. The diffusion generation current of holes (J_h^{gen}) flows from n to p side. It arises from pairs generated just on the n side of the depleted region by thermal excitation of electrons out of the valence band. When such a hole diffuses into the depletion layer it is swept to the p side of the junction by the strong field in the junction. Diffusion generation current does thus not depend on bias voltage. The recombination current of holes (J_h^{rec}), on the other hand, flows from the p to the n side of the junction where it recombines with a free electron. This current flows in the direction opposite to the electric field and thus only holes with a thermal energy sufficient to surmount the potential barrier contribute to the recombination current. The number of such holes is proportional to $e^{-e_0 \Delta V/k_B T}$, thus

$$J_h^{rec} \propto e^{e_0(-V_{bi}+V)/k_B T} \ , \tag{2.23}$$

where $V < 0$ for reverse bias. The total diffusion current of holes is a difference of both components $J_h = J_h^{rec} - J_h^{gen}$. From the condition that there is no net current when no external voltage is applied follows $J_h^{rec}(V = 0) = J_h^{gen}$ and taken together with 2.23 it gives

$$J_h^{rec} \ = \ J_h^{gen} e^{eV/k_B T} \ . \tag{2.24}$$

Thus the total current of the holes equals to

$$J_h \ = \ J_h^{rec} - J_h^{gen} \ = \ J_h^{gen}(e^{eV/k_B T} - 1) \tag{2.25}$$

The size of the diffusion generation current J_h^{gen} can be estimated in terms of diffusion lengths and carrier lifetimes. Holes are generated by thermal generation at a rate $\frac{p_{n0}}{\tau_h}$ per unit volume, where p_{n0} is the equilibrium hole density on the n side and τ_h the hole lifetime. They stand a considerable chance to enter the depleted region and to be swept to the n side if generated within a diffusion length L_h from the boundary of the depleted region. Thus the flow of the thermally generated holes per unit area into the depleted region will be of order $J_h^{gen} \approx \frac{L_h p_{n0}}{\tau_h}$.

The situation is analogous for the electrons except for inverted directions. But since also the charge sign is opposite the total electric current is the sum of the electron and hole component.

$$j_{dif} \ = \ e_0(J_h + J_e) \ = \ j_{sat}(e^{eV/k_B T} - 1) \tag{2.26}$$

where V is external voltage and j_{sat} is the saturation[9] current density.

The result of the derivation described here agrees well with a strict derivation as given in e.g. [8], with the saturation current equal to

$$j_{sat} = \frac{e_0 n_{p0} L_e}{\tau_e} + \frac{e_0 p_{n0} L_h}{\tau_h} \ . \tag{2.27}$$

Using tipical values $L \approx 1$ μm, $\tau \approx 10^{-5}$ s and $N_D \approx 10^{12}$ cm^{-3} one obtains $j_{sat} \approx 0.1$ nA/cm^2.

2.1.5 Generation Current in Depleted Region

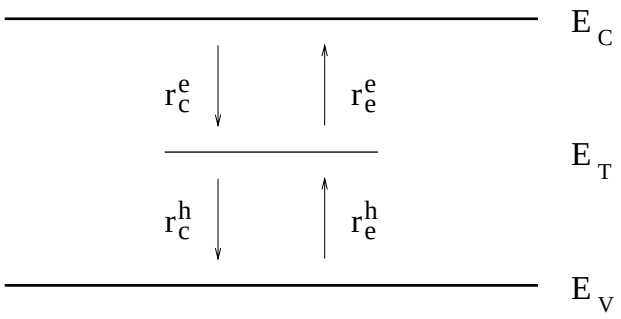

Figure 2.3: Emission and capture processes from an energy level E_T. Arrows present electron transitions.

Generation current in the depleted region is the most important source of the bulk leakage current in highly irradiated high resistivity diodes.

In case of the diffusion current, generated minority charge carriers have to diffuse to the space charge region to be swept to the other side or, in the case or majority carriers, to diffuse to the other side of the SCR surmounting the potential barrier to contribute to the leakage current. Electron-hole pairs generated in the depleted region are however immediately swept to the neutral region. The generation current contribution thus depends mostly on the pair generation rate and generation volume. To determine its contribution it is thus necessary to determine the pair generation rate in the space charge region.

The generation current occurs via trapping centers in the depleted region. There are four processes that can change the occupancy of an energy level E_T in the band gap (figure 2.3):

[9] It is called saturation current because this is the asymptotic value of the diffusion current for a reverse biased diode when $V \to -\infty$.

- electron capture from the conduction band
- electron emission to the conduction band
- hole capture from the valence band
- hole emission to the valence band

The capture rates for electrons and holes are given by

$$r_c^e = \sigma_e^T n v_e (1 - f_T) N_T \qquad r_c^h = \sigma_h^T p v_h f_T N_T \tag{2.28}$$

and the emission rates

$$r_e^e = e_e f_T N_T N_C \qquad r_e^h = e_h (1 - f_T) N_T N_V \ . \tag{2.29}$$

Here N_T is trap concentration and $f_T = (1 + e^{\frac{E_T - E_F^T}{k_B T}})^{-1}$ is the probability that the trap energy level E_T is occupied by an electron. $\sigma_{e,h}^T$ are capture cross sections for electrons and holes by a trap T, $e_{e,h}$ are emission probabilities for electrons and holes, and $v_{e,h}$ their thermal velocities

$$v_{e,h} = \sqrt{3 k_B T / m_{e,h}^*} \ . \tag{2.30}$$

From the condition that in thermal equilibrium emission and capture rates have to be equal follows

$$e_e = \sigma_e^T v_e e^{-(E_C - E_T)/k_B T} \qquad e_h = \sigma_h^T v_h e^{-(E_T - E_V)/k_B T} \ . \tag{2.31}$$

The change in concentration of occupied traps per time is the sum of the processes described

$$\frac{dn_T}{dt} = r_c^e - r_e^e - r_c^h + r_e^h \tag{2.32}$$

where $n_T = f_T N_T$ is the concentration of occupied traps. But since in the SCR almost no free charge carriers exist ($n \approx p \approx 0$) no capture will occur and only emission processes take place

$$\frac{dn_T}{dt} = r_e^h - r_e^e \ . \tag{2.33}$$

In a steady state, trap occupancy is constant in time ($\frac{dn_T}{dt} = 0$) therefore emissions of electrons and holes have to be balanced $r_e^h = r_e^e$. From that and equations (2.29) the trap occupancy f_T can be determined

$$f_T = \frac{e_h N_V}{e_e N_C + e_h N_V} \tag{2.34}$$

and by inserting this value back into emission rates (2.29) the creation rate of electron-hole pairs can be determined

$$r_e^e = r_e^h = r^{pair} = \frac{e_h N_V e_e N_C}{e_e N_C + e_h N_V} N_T \ . \tag{2.35}$$

Inserting (2.31) into (2.35) and assuming $N_C \approx N_V$, $\sigma_e^T \approx \sigma_h^T$ and $v_e \approx v_h$ one obtains

$$r^{pair} = N_T \sigma_{e,h}^T v_{e,h} N_{C,V} e^{-E_g/2k_BT} \cosh^{-1}\left[\frac{1}{k_BT}\left(E_T - \frac{1}{2}(E_V + E_C)\right)\right] \ . \tag{2.36}$$

Equation 2.36 shows that the creation rate of electron-hole pairs is maximal when $E_T = \frac{1}{2}(E_C + E_V)$. This means that the most efficient electron-hole pair generation centres are those located close to the middle of the bandgap. The situation is similar even if $N_C \approx N_V$, $\sigma_e^T \approx \sigma_h^T$ and $v_e \approx v_h$ are not assumed. In that case the trap energy for maximal r^{pair} is shifted to

$$E_T(max) = \frac{1}{2}\left[E_C + E_V + k_BT \ln\left(\frac{\sigma_e^T v_e N_C}{\sigma_h^T v_h N_V}\right)\right] \tag{2.37}$$

and the function deviates somewhat from the symmetrical form[10].

The total current density due to generation in the depleted region is given by an integral of the generation rate over the space charge region

$$j_{SCR} = e_0 r^{pair} w \ . \tag{2.38}$$

Since $w(V) \propto \sqrt{V}$ also the bulk generation current is proportional to $\sqrt{V}$ as long as the diode is not fully depleted. To determine the temperature dependence, we use $E_T \approx E_i$ [11] eq. 2.36 and take into account $v_{e,h} \propto \sqrt{T}$ (eq. 2.30). Thus we obtain

$$j_{SCR} \propto T^2 e^{-\frac{E_g}{2k_BT}} \ . \tag{2.39}$$

The bulk generated reverse current in an unirradiated diode is of the order of nA/cm^2, while for a diode irradiated to 10^{14} n/cm^2 it is of the order of μA/cm^2. The difference is due to the increase of generation current, caused by additional traps close to mid-gap, introduced by irradiation. Generation current is thus the main source of the reverse current in irradiated samples, so one should expect that temperature dependence of the reverse current is following equation 2.39.

[10] One of the exponential terms included in cosh is multiplied by a factor $\frac{\sigma_e^T v_e N_C}{\sigma_h^T v_h N_V}$.

[11] Only traps close to mid-gap are considered, since they give the largest contribution to the leakage current.

The situation is however different if the major contribution to the leakage current is from traps with high concentration but somewhat away from the mid-gap [12]. In that case, one of the exponential terms in cosh in eq. 2.36 prevails and one obtains

$$r^{pair} = \sigma^T_{e,h} v_{e,h} N_{C,V} e^{-\frac{E_g}{2k_B T}} e^{-\frac{1}{k_B T}(E_T - \frac{1}{2}(E_V + E_C))} \ . \tag{2.40}$$

This could account for a higher energy (1.2 eV [13, 14, 15] compared to E_g=1.1 eV) observed in the scaling of reverse current with temperature.

2.1.6 N_{eff} from C/V Measurements

One can define the depletion layer capacitance as the ratio of differential change of charge per differential change of applied voltage

$$C(V_0) \ = \ \frac{dQ}{dV}|_{V=V_0} \ . \tag{2.41}$$

In case of a one-sided abrupt junction the capacitance is given by

$$C(V) = \frac{\epsilon_{Si}\epsilon_0 S}{w} = \sqrt{\frac{\epsilon_{Si}\epsilon_0 e_0 N_{eff}}{2V}} S \tag{2.42}$$

where $Q = e_0 N_{eff} S w$ (S is the sample area) was used together with eq. 2.9. It shows that for N_{eff} constant over the detector depth, the graph of $1/C^2(V)$ versus V is a straight line for reverse voltages bellow full depleted voltage

$$\frac{d(1/C^2(V))}{dV} = \frac{2}{e_0 \epsilon_{Si}\epsilon_0 N_{eff} S^2} \ , \tag{2.43}$$

and a constant value for higher voltages. The position of the kink determines FDV and the slope determines N_{eff}.

A similar set of equations can be used to determine the N_{eff} distribution over the sample depth from a capacitance versus voltage (C/V) measurement in a case of a non-uniform distribution. Equation 2.43 can be rewritten [8] as

$$\frac{d(1/C^2(V))}{dV} = \frac{2}{e_0 \epsilon_{Si}\epsilon_0 N_{eff}(V) S^2} \tag{2.44}$$

giving the N_{eff} value in terms of applied voltage. To determine it in terms of depth one can use the relation [8]

$$w(V) = \frac{\epsilon_{Si}\epsilon_0 S}{C(V)} \ . \tag{2.45}$$

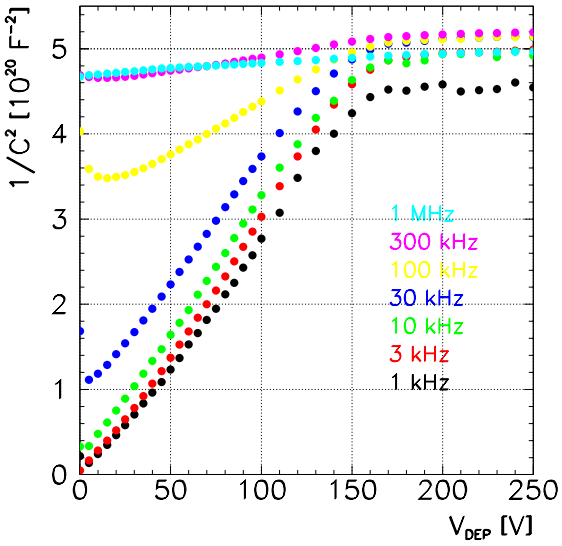

Figure 2.4: C/V measurement of a diode, irradiated to $5 \cdot 10^{13}$ n/cm^2 and annealed for five months at 20°C. The difference in signals obtained by different measurement frequencies is shown. The measurement was performed at 5°C.

The situation is more complicated in case of deep energy levels. For those the emission time, defined as the inverse of emission probability $\tau_T = \frac{1}{e_T N_{C,V}}$ (eq. 2.31), can be large compared to the oscillation time of the measuring signal. In such a case deep traps do not contribute to the measured signal. As can be seen from eq. 2.31 the emission time depends exponentially on the temperature. Therefore a linear decrease in temperature corresponds to a logarithmic decrease in frequency. A change in the measuring frequency or temperature thus affects the signal from deep energy levels and consequently the shape of the C/V curve (figure 2.4). It also results in somewhat higher full depletion voltage as determined from the kink in C/V plot at lower frequencies. This effect was systematically studied by [16, 17] who report about 10% increase of FDV as frequency changes from 10 kHz to 1 kHz. It is suggested the reason may be the presence of a transition region between the space charge region and the neutral bulk in heavily irradiated silicon. Measurement signals of different frequencies might thus probe different parts of this transition region.

To avoid the influence of this effect when comparing different samples, all measurements in the laboratory were taken at 5°C and FDV as obtained from 10 kHz measurement were used for comparison. Measurements at the reactor (i.e. during and early after irradiation) were however taken at the irradiation temperature and were affected by this phenomenon. A more detailed decription of measuring methods used in this work can be found in section 3.5.

2.2 Radiation Induced Defects

Damage caused by radiation can be divided into two groups, surface damage and bulk damage. Due to the interest of electronic industry, the surface damage is better understood and can be controlled to a certain extent by proper design and manufacturing process. Surface damage mainly manifests as charge accumulation in the oxide and subsequent breakdown. Charge accumulation at the silicon-oxide interface significantly decreases the inter-strip resistance of microstrip detectors. Therefore the signal has to be collected very quickly to minimise the loss due to leakage to neighbouring strips. An addition of silicon nitride reduces breakdown problems through silicon oxide [12].

The bulk damage in high resistivity silicon is however much less understood. An extensive study of the bulk damage for the purpose of experiments at high luminosity colliders is therefore ongoing.

In tracking detectors full depletion depths are required. According to eq. 2.10, 2.13 the full depletion voltage is proportional to the effective dopant concentration. Since low operation voltages are sought to avoid breakdown and extensive heating, high resistivity silicon is used in tracking devices. There the concentration of irradiation induced defects can be comparable or even much larger than the initial dopant concentration. Thus construction of trackers for new large experiments, where they will operate in high irradiation environments, demands an intensive study of the irradiation induced bulk defects and to those the further discussion is focused on.

2.2.1 Defect Generation

The energy loss by interaction of an incoming particle with matter can be divided into two parts: ionisation and non-ionising energy loss (NIEL). Due to fast recombination of charge carriers the ionising energy loss does not lead to long term bulk damage. NIEL contains displacements of lattice atoms and nuclear reactions. They both can result in long term bulk damage and will be described in the following sections.

Nuclear Reactions The most important nuclear reaction resulting from neutron irradiation is transmutation to phosphorus

$$^{30}Si + n \rightarrow ^{31}Si + \gamma \ , \quad ^{31}Si \rightarrow ^{30}P + e^- + \bar{\nu}. \tag{2.46}$$

Transmutations to Al and Mg are also possible, but have a few orders of magnitude lower cross-sections, so we shall first estimate the rate of phosphorus production.

The integral radiative capture cross-section σ_γ for the reaction 2.46 is 96 mb for a thermal spectrum and 670 μb for a typical fission (Watt) spectrum. At the irradiation

sites used in this work the flux in both parts (thermal and fast) of the spectrum is comparable[12]. Due to the larger cross-section thus only the thermal part needs to be considered. Change of phosphorus concentration N_P after neutron fluence Φ is given as a product $N_P = R_P \cdot \Phi$ where R_P is the phosphorus introduction rate. The introduction rate can be estimated by

$$R_P = \sigma_\gamma A(^{30}Si) N_{Si} \ . \tag{2.47}$$

With atomic percent abundance of ^{30}Si isotope $A(^{30}Si)$=3.1% and $N_{Si} = \frac{N_{Av}\rho_{Si}}{A} = 5 \cdot 10^{22}$ cm^{-3} we obtain ^{30}P introduction rate of $R_P = 1.5 \cdot 10^{-4}$cm^{-1}. As will be shown later it is more than two orders of magnitude lower compared to introduction rates of active lattice defects and thus negligible. Since cross-sections for transmutation to Al and Mg are even smaller they can also be neglected.

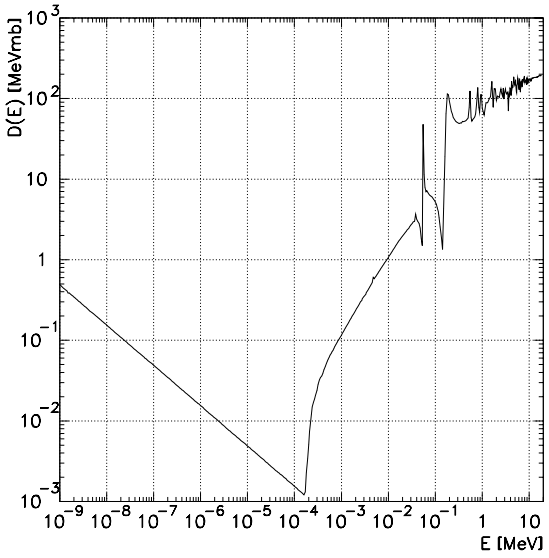

Figure 2.5: The neutron damage function for silicon according to Ougouag [27].

Lattice Atoms Displacements The most important process for radiation damage in silicon is the displacement of lattice atoms. An incoming particle can transfer a significant part[13] of its energy to a Si atom. Bulk damage occurs when the transfer of kinetic energy is sufficient to displace a silicon atom from its lattice site[14]. Displaced atoms may come

[12] Measurements of the spectra are presented in chapter 3.

[13] As much as 13% of the incoming neutron energy can be transferred to the Si atom as can be seen from the equation $E_{max}/E_n = 4m_n\, m_{Si}/(m_n + m_{Si})^2$, describing the collision kinematics.

[14] Around 15 eV of recoil energy is required [24].

to rest in interstitial positions (I), leaving vacancies (V) at their original locations. If the kinetic energy of the recoiling atom is sufficient it can displace further Si atoms, creating a cluster of displacements. Most of the resulting vacancies and interstitials recombine while others diffuse away and eventually create stable defects.

2.2.2 Comparing Radiation Damage Measurements

As already mentioned, the part of energy loss of the incoming particle used for ionization (electron-hole pair creation) does not contribute to the long-term bulk damage. Thus only non-ionising energy loss (NIEL) is to be taken into account when damages caused by different particles or particles of different energies are compared. According to this "NIEL hypothesis" the radiation damage of the bulk depends on the non-ionising energy loss only. This has been experimentally demonstrated for protons, neutrons and pions [13, 18, 19, 20, 21, 22].

Displacement damage scales linearly with NIEL. It is given by the damage function $D(E)$ [25]. The damage caused by different particles is usually compared with the damage caused by neutrons. Since D depends on neutron energy (figure 2.5), the damage done by 1 MeV neutrons is taken as a reference point. The standard value for the neutron damage at 1 MeV is 95 MeVmb [26]. For an irradiation with particles A with spectral distribution $\frac{d\phi}{dE}$ and cut-offs E_{min} and E_{max} a hardness factor κ can be defined as

$$\kappa_A = \frac{\langle D_A \rangle}{D(1MeVn)} = \frac{1}{D_n(1MeV)} \cdot \frac{\int_{E_{min}}^{E_{max}} D_A(E) \frac{d\phi_A}{dE}(E)\, dE}{\int_{E_{min}}^{E_{max}} \frac{d\phi_A}{dE}(E)\, dE}. \tag{2.48}$$

In order to allow a universal comparison of results it is common practice to refer to the equivalent fluence Φ_{eq} of 1 MeV neutrons which would have caused the same damage as the fluence Φ of particles actually applied. Φ is converted into Φ_{eq} by multiplying it with the hardness factor κ

$$\Phi_{eq} = \kappa_A \, \Phi_A \ . \tag{2.49}$$

2.2.3 Types of Defects

At the interaction of the traversing particle with the lattice an interstitial-vacancy pair (Frenkel pair) or a cluster can be produced, depending on energy, transferred to the primary atom. Though physical properties of clusters are not determined yet, theoretical models have been proposed [23]. In the first phase the disordered region consists of many interstitials and vacancies. Most of the vacancies and interstitials recombine, some vacancies may interact to form stable divacancies or higher vacancy complexes while the

Primary Vacancies	Primary Interstitials	Replaced impurities
Group A		
$V + P \rightarrow VP$	$I + VP \rightarrow P$	$C_i + C_s \rightarrow C_i$-$C_s$
$V + O \rightarrow V\,O$	$I + VO \rightarrow O$	$C_i + O_i \rightarrow C_i$-$O_i$
$V + VO \rightarrow V_2O$	$I + V_2 \rightarrow V$	$C_i + P_s \rightarrow C_i$-$P_s$
$V + C_i \rightarrow C_s$	$I + C_s \rightarrow C_i$	
$V + V_2O \rightarrow V_3O$	$I + V_3O \rightarrow V_2O$	
$V_2 + V \rightarrow V_3$		
Group B		
$V + V \rightarrow V_2$	$I + V \rightarrow Si$	
$V_2 + V \rightarrow V_3$		

Table 2.1: Survey of possible defect reactions. Group A reactions are caused by diffusion of interstitials and vacancies throughout the crystal. To group B belong the reactions, which have a significant chance of occurring during a primary cascade. Indexes $_i$ and $_s$ stand for interstitial and substitutional.

rest diffuse away. Those can react with other radiation induced defects, forming defect complexes, or react with impurity atoms such as carbon, oxygen and phosphorus, those being among the most common impurities in silicon. When only a Frenkel pair is created only reactions with existing defects are possible. Thus reactions of the defects can be divided into two groups. In the group A are reactions of vacancies and interstitials diffusing throughout the crystal. Group B reactions only have a significant chance of occurring within the cluster, where the defect density is high. Possible reactions of both groups are listed in table 2.1 and the most relevant defect configurations are shown schematically in figure 2.6.

2.3 Effects on Bulk Properties

Defects generated during the irradiation have the following effects on the bulk properties:

- They introduce new energy levels in the band gap, contributing to emission and capture processes and thus affecting the leakage current.
- They can act as donors or acceptors, changing the effective dopant concentration N_{eff} thus affecting the full depletion voltage.
- Increased capture probability decreases charge carrier lifetime thus decreasing the charge collection efficiency.

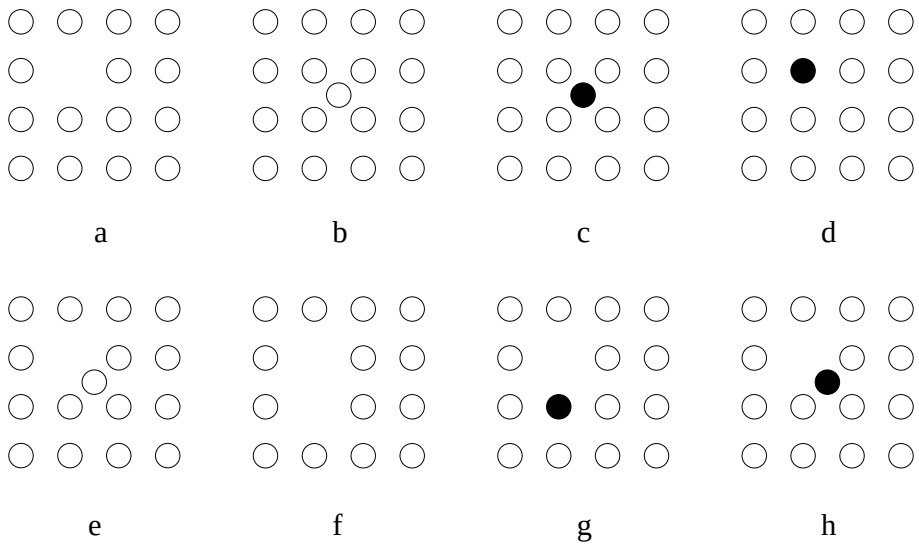

Figure 2.6: Various possible defect configurations. Simple defects are: a) vacancy V, b) interstitial silicon atom I, c) interstitial impurity atom, d) substitutional impurity atom (e.g. phosphorus as donor). Examples of defect complexes are: e) close pair I-V, f) divacancy V-V, g) substitutional impurity atom and vacancy (e.g. VP complex), h) interstitial impurity atom and vacancy (e.g, VO complex)

2.3.1 Leakage Current

Defects generated due to irradiation may introduce energy levels in the band gap. Most defects have one energy level with two charge states as was also assumed in the derivation of the generation rate in the depleted region (section 2.1.5). Acceptors are negatively charged when occupied by an electron and neutral when empty, while donors are positively charged when unoccupied but neutral otherwise. Some of the defects however have more than one energy level and more charge states. Such an example is divacancy (V_2) with three energy levels in the band gap, giving four charge states [28].

As shown in section 2.1.5 the largest contribution to the leakage current comes from defects with energy levels close to the middle of the bandgap. While standard doping materials (P, B) have energy levels close to the conduction (donors) or valence band (acceptors) this is not the case with the irradiation induced defects (figure 2.7). This means that radiation induced defects can contribute a major part of the leakage current generated in the depleted region.

Since the defect density is proportional to the total fluence Φ ($N_{def} = g_{def} \cdot \Phi$ with g_{def} the defect generation rate) and the generation current proportional to mid-gap defect

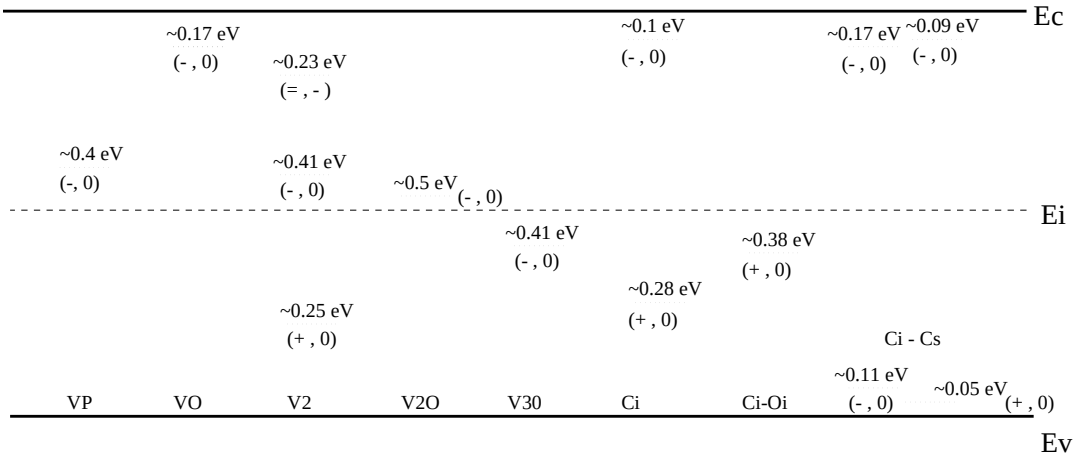

Figure 2.7: Energy levels of some vacancy and carbon related defects. The defect charge states are shown in brackets, e.g. minus and neutral (-,0). Above the dotted line the energy of the trap is written; in the lower half ΔE_V and in the upper half ΔE_C. Sign = means the double charged state. In the figure, data from [14] were used.

concentration (eq. 2.35, 2.38), also the irradiation induced leakage current is proportional to the equivalent fluence Φ_{eq}

$$\frac{\Delta I}{V} = \alpha \cdot \Phi_{eq} \ , \tag{2.50}$$

where α is the leakage current damage constant and V the volume.

2.3.2 Effective Dopant Concentration

The effective dopant concentration N_{eff} is composed of ionised shallow levels (donors and acceptors) and deep levels. Before irradiation, the concentration of deep levels is negligible and the effective dopant concentration is determined by the difference of donor and acceptor concentrations $N^0_{eff} = N^0_D - N^0_A$. During the irradiation two types of processes take place. One is the introduction of new defects that may act either as donors or acceptors and the second is the removal of initial shallow levels by creation of defect complexes. It is well proven by experiments that deep level acceptor-like states are generated during irradiation. According to equations 2.10 and 2.13 the full depletion voltage is proportional to $|N_{eff}|$. It means that, for an initially n type bulk, at low fluences FDV is decreasing with fluence until the inversion point is reached and then it starts to increase with fluence. Thus at high total fluences full depletion voltage may grow too high for a normal operation of the device. This increase of depletion voltage is the main problem for operation of silicon detectors in a high radiation environment.

The fluence dependence of the initially present shallow level dopants is however not well understood yet. Different models have been proposed to explain experimental results.

R. Wunstorf et al. [29] reports on measurements of removal of both initial shallow donors and acceptors, together with deep level acceptor creation. Development of the effective dopant concentration with fluence can thus be parametrised as

$$N_{eff}(\Phi) = N_D^0 e^{-c_D\Phi} - N_A^0 e^{-c_A\Phi} - g\Phi \tag{2.51}$$

Donor removal constant has been determined to be $c_D \approx 2.5 \cdot 10^{-13}$ cm^2 and acceptor removal constant $c_A \approx 1.98 \cdot 10^{-13}$ cm^2.

F. Lemeilleur [30] however reports linear dependence of the inversion fluence on initial dopant concentration with $\Phi_{inv} = (18 \pm 0.6\text{cm}) \cdot N_{eff}(0)$. At the same time fluence dependence of N_{eff} is parametrised by

$$N_{eff}(\Phi) = N_D^0 e^{-c_D\Phi} - N_A^0 - g\Phi \tag{2.52}$$

with $c_D \approx 2.5 \cdot 10^{-14}$ cm^2 and $g \approx 1.1 \cdot 10^{-2}$ cm^2.

H. Feick [20] assumes low level of compensation of his initial material ($N_A^0 \ll N_D^O$) and is thus not sensitive to changes in concentration of initial acceptors. Exponential dependence of the donor concentration on fluence is reported with removal rate equal to $c_D = (2.4 \pm 1.4) \cdot 10^{-13}$ cm^2, but with only about a third of initial donors being subject to the removal. Reduced donor removal was also reported in [50].

Watts [31] used numerical modelling of deep acceptor creation to generate N_{eff} versus neutron fluence for p and n type diodes. No initial dopant removal was used in the calculations and good agreement with the data is reported. It is thus claimed that no initial dopant removal is required to successfully explain the fluence dependence of N_{eff}. Similarly, compensation of initial donors by deep acceptors instead of donor removal is also suggested by [32].

Due to lack of information about initial donor and acceptor concentration, low compensation[15] has been assumed throughout this work. Initial donor concentration is thus given by full depletion voltage before irradiation according to eq. 2.10. Donor removal with c_D=2.4·10^{-13} cm^2 from [29] has been assumed, giving almost complete removal of initial donors for fluences above 10^{13} n/cm^2. Thus only the acceptor creation part $g\Phi$ remains in eq. 2.51 or 2.52 while the contribution of initial doping is neglected. However, even if the initial donors are not completly removed during the irradiation, their concentration in most samples used in this work is small compared to the concentration of radiation induced deffects.

[15] Assuming low compensation $N_A^0 \ll N_D^0$, and with initial donor concentration $N_D^0 < 4 \cdot 10^{11}$ cm^{-3}, initial acceptor concentration can be neglected.

2.3.3 Charge Collection Efficiency

Deep energy levels introduced by irradiation reduce the lifetime of charge carriers. This trapping effect can be described by introducing a characteristic trapping time constant τ^{tr} used to modify the number of charge carriers $N_{e,h}$

$$N_{e,h} = N^0_{e,h} e^{-\frac{t}{\tau^{tr}_{e,h}}} , \tag{2.53}$$

where the inverse overall trapping time constant $(\tau^{tr}_{e,h})^{-1}$ is given by a sum of all capture rates (eq. 2.28)

$$(\tau^{tr}_e)^{-1} = \sum_{traps} \sigma^T_e v_e (1 - f_T) N_T \qquad (\tau^{tr}_h)^{-1} = \sum_{traps} \sigma^T_h v_h f_T N_T \tag{2.54}$$

where trap occupation for the SCR is determined by (2.34). From 2.54 we see that the trapping time constant is inversely proportional to the trap concentration N_T. And since N_T is proportional to fluence one gets a linear dependence of $1/\tau^{tr}$ with fluence $1/\tau^{tr} = 1/\tau^{tr}_0 + \Phi/K$ with the proportionality factor $1/K$. This relation has been experimentally confirmed up to $2.5{\cdot}10^{15}$ n/cm^2 [33]

However, in determining the effect of different traps on the charge collection efficiency it has to be taken into account that only traps with detrapping time large compared to the charge collection time reduce the charge collection. For those with large detrapping rates, most of the captured carriers are released within the shaping time of readout electronic, thus not affecting the collected signal.

The drop in the charge collection efficiency at a fluence around 10^{14} n/cm^2 is around 10% with fast shaping (few 10 ns) [13, 34]. At the moment no means of avoiding this effect seem to be suggested.

2.4 Time Evolution of Defects

Regarding their time development, irradiation induced defects can be divided into three groups (fig. 2.8)

- Defects stable in time
- Electrically active defects that change to non-active ones (annealing)
- Electrically non-active defects that change to active ones (reverse annealing)

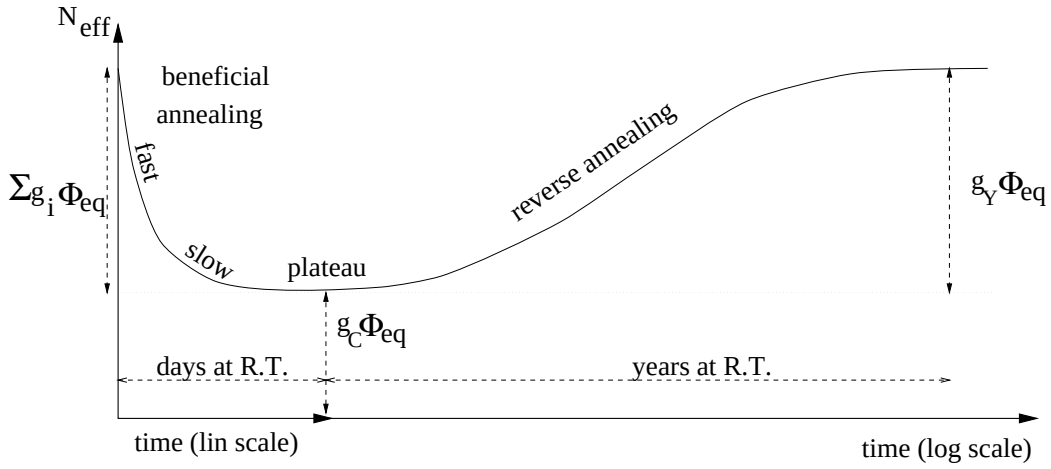

Figure 2.8: Schematic plot of time development of N_{eff}. All three phases are shown with introduction rates for responsible defects. Note that reverse annealing is shown in the logarithmic time scale.

The change of a defect can be either due to dissociation or combination of a defect complex. In case of the dissociation $X \rightarrow Y$ the reaction can be described as a first order process

$$-\frac{dN_Y}{dt} = \frac{dN_X}{dt} = -k_1^Y N_X \ , \tag{2.55}$$

with the general solution

$$N_X(t) = N_X^0 e^{-k_1^Y t} \tag{2.56}$$

$$N_Y(t) = N_X^0 (1 - e^{-k_1^Y t}) \ . \tag{2.57}$$

When the new complex is due to a reaction of two defects $X_A + X_B \rightarrow Y$ it can be described by

$$-\frac{dN_Y}{dt} = \frac{dN_{X_A}}{dt} = \frac{dN_{X_B}}{dt} = -k_2^Y N_{X_A} N_{X_B} \ , \tag{2.58}$$

with the solution ($N_{X_A}^0 > N_{X_B}^0$)

$$N_Y(t) = N_{X_B}^0 \frac{1 - e^{-k_2^Y t (N_{X_A}^0 - N_{X_B}^0)}}{1 - (N_{X_B}^0 / N_{X_A}^0) e^{-k_2^Y t (N_{X_A}^0 - N_{X_B}^0)}} \ . \tag{2.59}$$

In the case of two defects with similar initial concentrations $N_{X_A}^0 = N_{X_B}^0$ or a reaction between defects of the same type one obtains

$$N_X(t) = \frac{N_X^0}{1 + N_X^0 k_2^Y t} \tag{2.60}$$

$$N_Y(t) = N_X^0 - N_X(t) = N_X^0(1 - \frac{1}{1 + N_X^0 k_2^Y t}) \tag{2.61}$$

describing a second order process. If, however, concentration of one type of interacting defects is much larger than the concentration of the other ($N_{X_A}^0 \gg N_{X_B}^0$) the dynamics of the process can again be described by the first order equation with $k_1^Y = k_2^Y N_{X_A}^0$.

In the equations, N_X^0 is the initial concentrations of defect X and k_1^Y and k_2^Y are the reaction constants for the first and second order processes. From equations 2.55 and 2.58 it can be seen that in the first order reaction, the reaction rate depends linearly on defect concentration while in the second order case it depends quadratically.

2.4.1 Time Evolution of Leakage Current

Traditionally, measurements of the time development of the leakage current have been fitted with an ansatz [46, 19, 14, 20]

$$I(t) = I(0)[A_C + \sum_i A_i e^{-t/\tau_i^\alpha}] \tag{2.62}$$

where A_0 represents the contribution of defects constant in time, A_i contributions of decaying defects, τ_i their decay times and t time after irradiation. To remove the effect of sample size and irradiation fluence, a more fundamental constant $\alpha = \frac{I}{V \cdot \Phi_{eq}}$ (eq. 2.50), where V is the sample volume, is usually used. Thus eq. 2.62 can be rewritten in terms of the α parameter as

$$\alpha(t) = \alpha_C + \sum_i \alpha_i e^{-t/\tau_i^\alpha} \ . \tag{2.63}$$

Only the contribution of defects constant in time and annealing defects has been determined in the leakage current, while no reverse annealing was observed. However recent results [35] as well as results presented in this work are showing also a long term annealing component, that could be described by an effective logarithmic time dependence, described by an ansatz

$$\alpha(t) = \alpha_E e^{-t/\tau_E^\alpha} - \alpha_L \ln(t/\tau_L^\alpha) \ . \tag{2.64}$$

2.4.2 Time Evolution of N_{eff}

Results on the N_{eff} time development show that all three types of defects are taking part in the time development of defects contributing to the space charge in the depleted region (fig. 2.8). While the annealing part can be described with a sum of exponentials like

the leakage current and thus indicates decays of active defects, the nature of the reverse annealing part is not fully understood yet. The time development of the N_{eff} can thus be parametrised as

$$N_{eff}(t) = N_C + \sum_i N_i e^{-t/\tau_i} + N_Y(t) \tag{2.65}$$

where N_C represents defects constant in time, N_i defects that anneal with time constants τ_i and N_Y defects responsible for the reverse annealing.[16] Depending on the reactions responsible for reverse annealing, $N_Y(t)$ is described by equations 2.57, 2.59 or 2.61, depending on the type of reaction(s) responsible for the reverse annealing. Agreement of the measured results with different options will be presented later in this work.

*

[16]Defects contributing to the charge in the SCR are not necessarily the same as those contributing to the leakage current, thus also time constants may differ.

3

Irradiation Facility

3.1 The Reactor

The reactor research centre of the Jožef Stefan Institute is located in Podgorica near Ljubljana. It is the site of an experimental nuclear reactor of type TRIGA, constructed to provide neutrons for experimental purposes. It can be run with large span in operating power (few W to 250 kW), enabling irradiations with various neutron fluxes at the same irradiation site.

The main part of the reactor is its core, consisting of fuel and control rods. It is surrounded by a graphite reflector and placed into a reactor vessel filled with water, all within a thick concrete shield (fig. 3.1). Irradiation sites can roughly be divided into two groups. Vertical channels are giving access to irradiation sites at the edge of the core or even in its centre, occupying a fuel rod position. In those, space available for a sample is highly limited (less than 2.5 cm diameter and 15 cm length). Horizontal irradiation channels are leading to irradiation sites some distance from the core. They can contain different materials to modify the neutron spectrum in the particular channel. In the scope of the present work, one horizontal and one vertical channel were exploited to achieve the desired irradiation conditions.

3.2 Selection of Irradiation Site

The properties of irradiation channels to be used were determined by the requested irradiation conditions. Those were:

- Neutron spectrum with a significant portion of fast neutrons (above 0.1 MeV).
- Flux of fast neutrons of the order 10^9 n/cm^{2}s or higher.

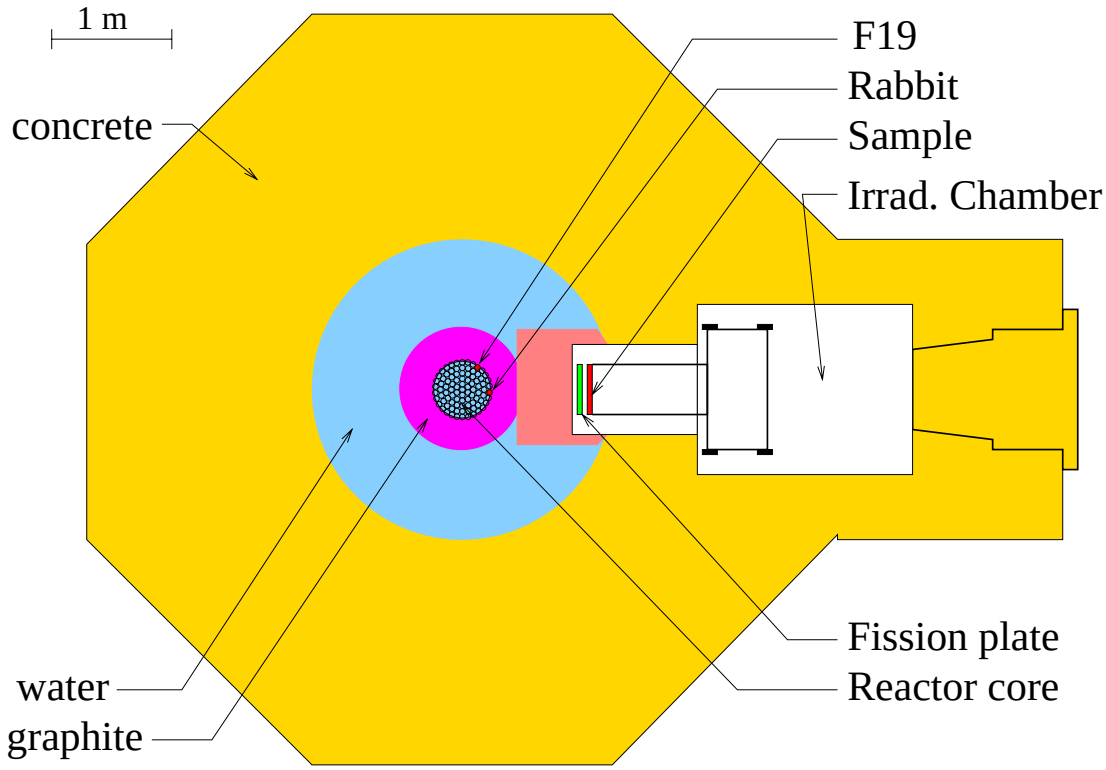

Figure 3.1: Schematic view of the reactor cross-section. The reactor core consists of fuel rods and control rods, surrounded by a graphite reflector. It is placed into a reactor vessel filled with water. Among many irradiation spots only those connected to this work are marked.

- Possibility to irradiate samples with dimensions up to 10×10 cm^2.
- Possibility to bias the samples and perform C/V (capacitance versus voltage) and I/V (current versus voltage) measurements during and after the irradiation.
- Possibility to keep the samples at a fixed temperature during and after irradiation.

The last two conditions can be reduced to free access for bias/measuring cables and cooling pipes while the second and the third condition were unfortunately not compatible. For that reason two irradiation channels had to be equipped. They were the irradiation chamber and the vertical irradiation channel F19. The vertical irradiation channel equipped with a rabbit system (F24) was also used at the beginning for fast irradiations where cooling and biasing of the samples were not required (fig. 3.1).

3.3 Irradiation Chamber

3.3.1 Channel Description

The irradiation chamber is one of the horizontal irradiation channels, widening at the end to a small chamber (approx. 2×2×2 m^3) (fig. 3.2). To increase the fast neutron flux, a fission plate[17] is placed in front of the sample during irradiations. During the irradiation, samples were kept in an irradiation box with controlled temperature. The box was mounted on a remote-driven trolley to move the sample into the channel and out of it.

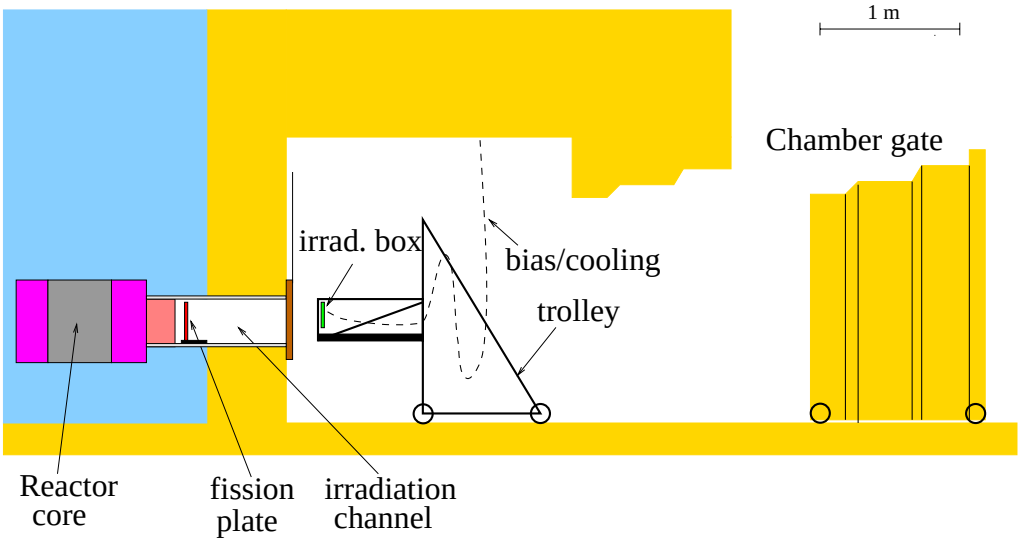

Figure 3.2: Schematic view of the irradiation chamber. The trolley with mounted irradiation box is in the outside position.

The irradiation box contained two independent cooling slots, connected to Peltier elements. Each was powered by a 12V DC power supply controlled by a Yokogawa UT15 temperature controller. The warm side of the Peltier elements was water cooled to 5-10°C. The sample temperature was measured by a Pt100 sensor, placed within a few mm from the sample and connected to the Yokogawa controller. Temperatures down to about -20°C could be obtained, stable within 0.2°C.

3.3.2 Measurement Setup

The reactor measurement setup enabled biasing of the samples and C/V and I/V measurements during and after the irradiation. It consisted of a Wentzel high voltage power

[17] The fission plate is made of 1468 g of ^{238}U, enriched to 20% ^{235}U, forming an active disc with a diameter of about 30 cm.

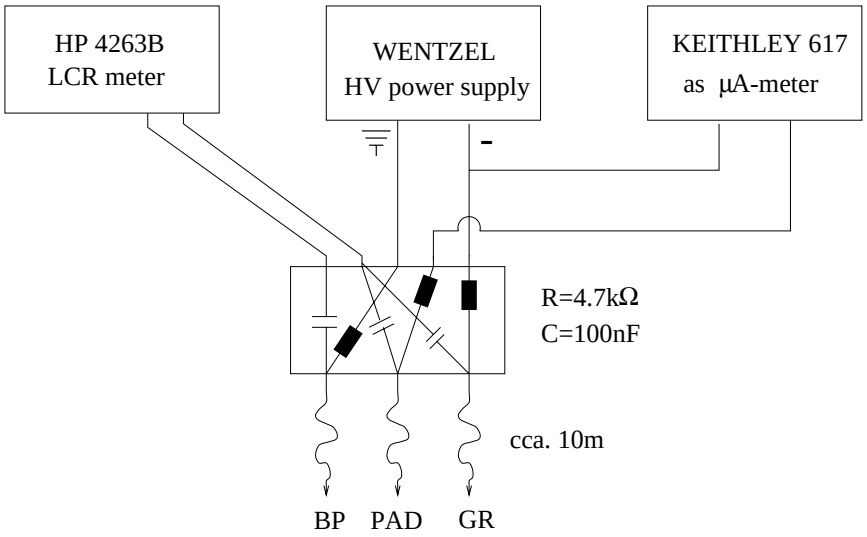

Figure 3.3: Schematic view of the measurement setup at the irradiation site. BP, TOP and GR are connections to sample back plane, pad and guard ring, respectively.

supply, computer controlled via a DAC converter, a KEITHLEY 617 source-measure unit used as a precise ampermeter and a HP4263B LCR-meter (figure 3.3). Decoupling capacitors were used to shield LCR meter from the high bias voltage. Four different frequencies of measuring voltage (100 Hz, 1 kHz, 10 kHz and 100 kHz) were used in C/V measurements. The sample temperature during and after the irradiation was measured by a PT100 sensor. The measurement method used in this work is discussed in more detail in section 3.5.

A careful study of the activation had to be performed on all materials used in the highly radiative environment close to the reactor core. The selection was mostly reduced to pure aluminium and a certain type of plastic (Novilon Oilon, produced by Akripol, Slovenia). After irradiations, few days had to pass before activity of the sample and cooling system decreased sufficiently to safely remove the sample and transfer it to the laboratory. The conditions were even harsher in channel F19 due to much higher neutron fluxes, leading to higher saturation activities.

3.3.3 Neutron Spectrum and Dosimetry

The low flux of fast neutrons (up to few times 10^8 n/cm^{2}s) at this irradiation site and desired total fluences around 10^{14} n/cm^2 demanded for irradiation times of over 100 hours. The long irradiation time prohibited direct use of In foil activation ($^{115}In + n \rightarrow ^{115} In^* + n'$, $^{115}In^* \rightarrow ^{115} In + \gamma$, $\tau = 4.4$ h) to monitor the fast neutron flux because of the short lifetime of the excited state. Thus an indirect way was established consisting

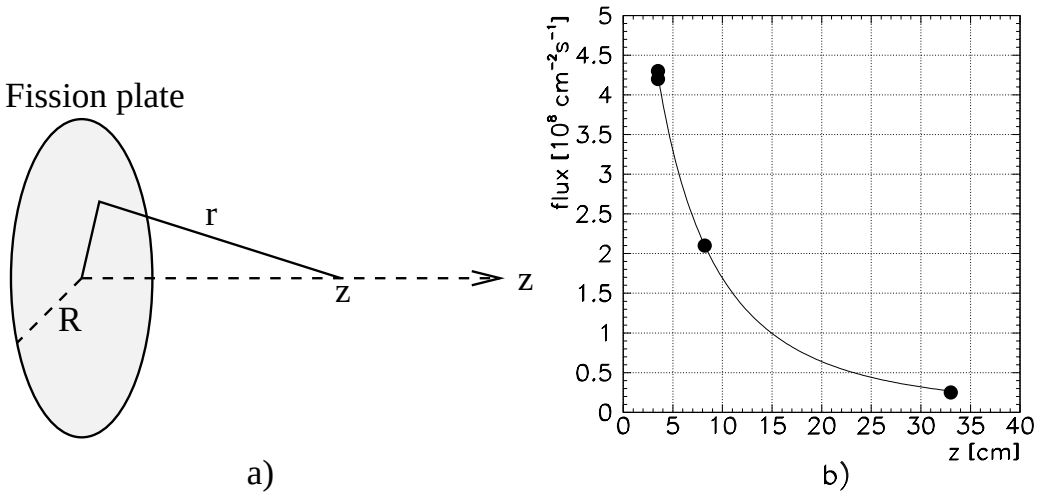

Figure 3.4: Dependence of the fast neutron flux on the distance from the fission plate. a) Schematical presentation of the setup. b) Comparison of measurements [36] and calculations.

of a calibration and an irradiation measurement. During short calibration measurements an In foil in a Cd shield[18] was placed at the sample position and a Zn foil was put in the middle of the box. After the irradiation, the activation of Zn (thermal neutron capture, decay time 244 days) was measured and compared to the fluence of fast neutrons as determined from the activation of In with a well known activation cross-section. In the irradiation run only the Zn foil was placed at the same position as in the calibration run. By comparison of Zn activations in both runs, the irradiation fluence was determined. The error of this method was estimated to be about 15%.

Due to the limited size of the fission plate, the fast neutron flux depends on the distance from the plate. Dependance on the distance can be determined by geometrical considerations (fig. 3.4)[19]. The following relation is obtained

$$\frac{\phi(z_1)}{\phi(z_2)} = \frac{\ln(1+\frac{R^2}{z_1^2})}{\ln(1+\frac{R^2}{z_2^2})} \tag{3.1}$$

where R is the radius of the fission plate and z the on-axis distance from it (fig. 3.4a). Measurements were performed at three different distances from the fission plate: 3.5 cm (2

[18] Cd shield was used to reduce In activation due to thermal neutrons.

[19] From the collision probability $P_1 = \frac{\sigma}{4\pi r^2}$ where σ is a reaction cross-section and r distance from the neutron source one obtains reaction probability as its integral over the surface of the fission plate $P = \int_{f.pl.} \frac{dN}{dS} P_1 dS$. From this flux dependence can be determined by $\phi(z) = \frac{P}{\sigma} = \int_{f.pl.} \frac{dN}{dS} \frac{1}{4\pi r^2} dS = \frac{dN}{dS} \frac{1}{4} \ln\left(\frac{z^2+R^2}{z^2}\right)$.

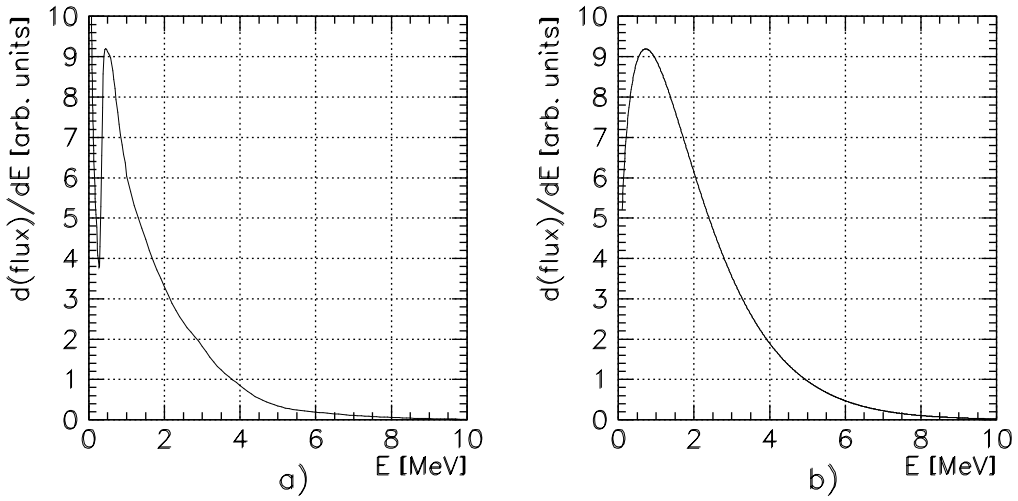

Figure 3.5: a) Fast neutron spectrum as measured 11 cm in front of the fission plate [36]. b) Watt spectrum [37].

meas.), 8.2 cm and 33 cm. The measured fluxes were $4.3{\cdot}10^8$ n/cm^{2}s and $4.2{\cdot}10^8$ n/cm^{2}s, $2.1{\cdot}10^8$ n/cm^{2}s and $2.5{\cdot}10^7$ n/cm^{2}s, respectively. As can be seen in fig. 3.4b the measured values can be fitted well with the calculated curve.

To determine the relative damage factor κ (eq. 2.48), it is necessary to know the shape of the neutron spectrum. For the calculation of the κ value in the irradiation chamber behind the fission plate, the result from an existing measurement [36] (fig. 3.5a) was used. The measurement was performed in front of the fission plate at the distance of 11 cm, while samples were irradiated behind the fission plate. Due to large absorption of slow neutrons in the fission plate, only the fast part of the measured spectrum is valid for the irradiations behind the plate. Using the Ougouag damage function values [27] (fig. 2.5) a κ value

$$\kappa_{IC} = 0.99 \tag{3.2}$$

was determined, for the energy interval (0.1 - 15 MeV). Contribution of the spectrum below 0.1 MeV was estimated to contribute less than 1% to NIEL damage.

To estimate the possible error, the κ_{IC} value (3.2) was compared with the κ value for a pure fission (Watt [37], fig. 3.5b). The value obtained was $\kappa_{Watt} = 1.05$. Watt spectrum gives the energy distribution of neutrons produced in the fission plate and the discrepancy is caused by the protons, comming directly from the core. The difference between both κ values was used to estimate the error on the value from the measured spectrum to less than 6%.

3.4 Irradiation Channel F19

3.4.1 Channel Description

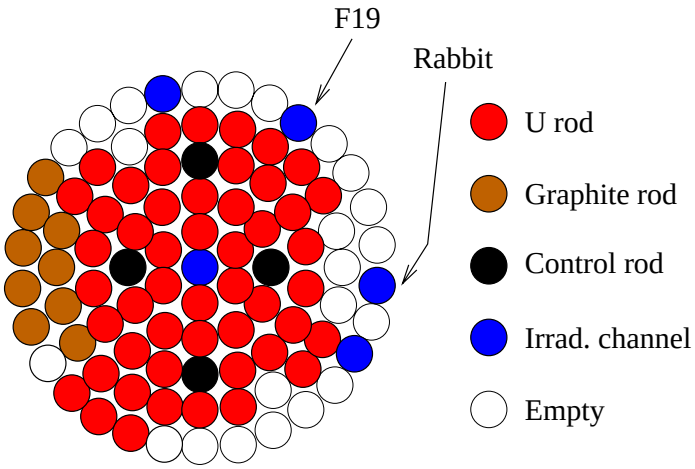

Figure 3.6: Schematic view of the reactor core as of 11.9.1996.

Irradiation channel F19 is one of the vertical channels leading to the edge of the reactor core where it is replacing a rod (fig. 3.6). The proximity of the core provides high neutron fluxes with a relatively high portion of fast neutrons (about 1/3 of the flux is above 0.1 MeV).

Low diameter of the channel and a bend[20] constrain sample dimensions to those fitting into a cylinder with 35 mm diameter and 12 cm length. A cooling scheme that fulfils these space limitations was designed. A cooling cylinder as shown in figure 3.7 was constructed and used as a part of a closed circuit liquid cooling[21]. The lowest stable temperature was limited by heating from the pump and surrounding air and was about 0°C. Samples were mounted on Al_2O_3 ceramic plates, supporting metalised kapton strips used for contacting. The sample temperature was monitored and stabilised by a Yokogawa UT15 temperature controller. After irradiation, samples were moved to a thermostat chamber with controlled temperature and held there until the activity of the sample and cooling cylinder was safe for handling and transport.

The measurement setup used for C/V and I/V measurements was the same as used for irradiations in the irradiation chamber (section 3.3.2). It provides measurements both at the irradiation site and in the thermostat chamber.

Flux of the fast neutrons (above 0.1MeV) is about $2 \cdot 10^{12}$ n/cm^{2}s at maximal reactor power of 250 kW and scales with power down to few 10 W. Much higher neutron flux can

[20] A bend about a meter above the core provides shielding of the reactor plateau from the core.
[21] Mixture of water and etylen glycol was used to provide cooling below 0°C.

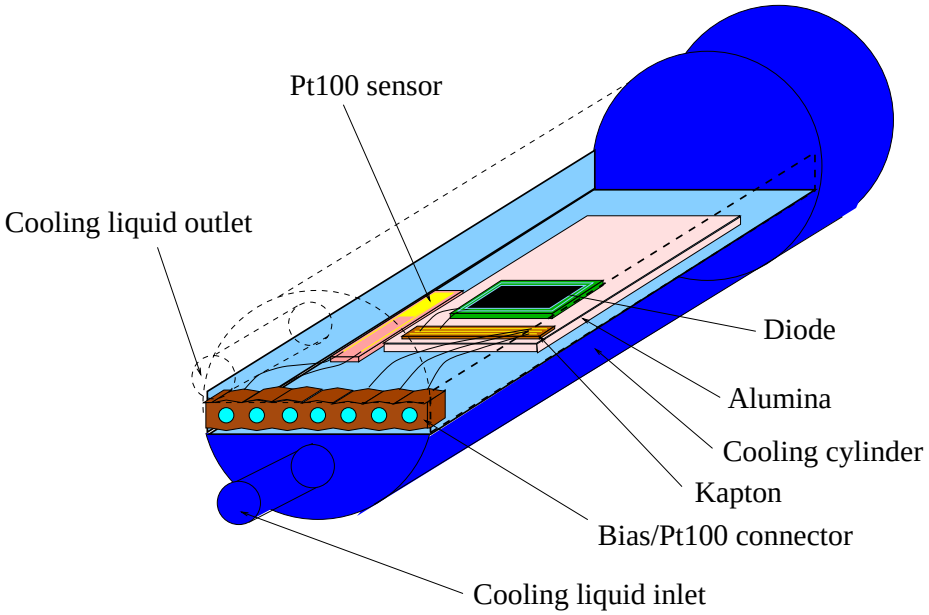

Figure 3.7: Schematic view of the cooling cylinder for sample cooling in the F19 irradiation channel. A sample mounted on Al_2O_3 ceramics and a Pt100 temperature sensor is displayed together with the connector for bias/measurement lines.

be obtained in pulsed mode. To pulse the reactor one of the control rods is pneumatically fired to a preset upper position, driving the reactor highly over-critical. This results in a fast increase of the neutron flux and heating of the reactor core. Temperature raise however causes an increase of neutron absorption in ^{238}U and hardens the thermal part of the spectrum thus decreasing the reaction rate in ^{235}U. Thus the pulse is stopped and the reactor is shut down. In the pulsed mode a total fluence of about 10^{14} n/cm^2 can be obtained in around 20 ms (approximate pulse width).

3.4.2 Neutron Spectrum and Dosimetry

The neutron spectrum in the irradiation channel F19 (fig. 3.8) was determined by simulation [38] and measurement [36].

The simulated spectrum was obtained using the MCNP4B Monte Carlo simulation code [39]. Since the reliability of the results depend crucially on the source description, a detailed description of the real TRIGA geometry [40] was used in the simulation. It included the exact configuration of all 91 locations in the core and a detailed description of fuel elements as well as control rods. It was tested with experimental results of a critical experiment [41]. Very good agreement with experimental results confirms the reliability of the model developed.

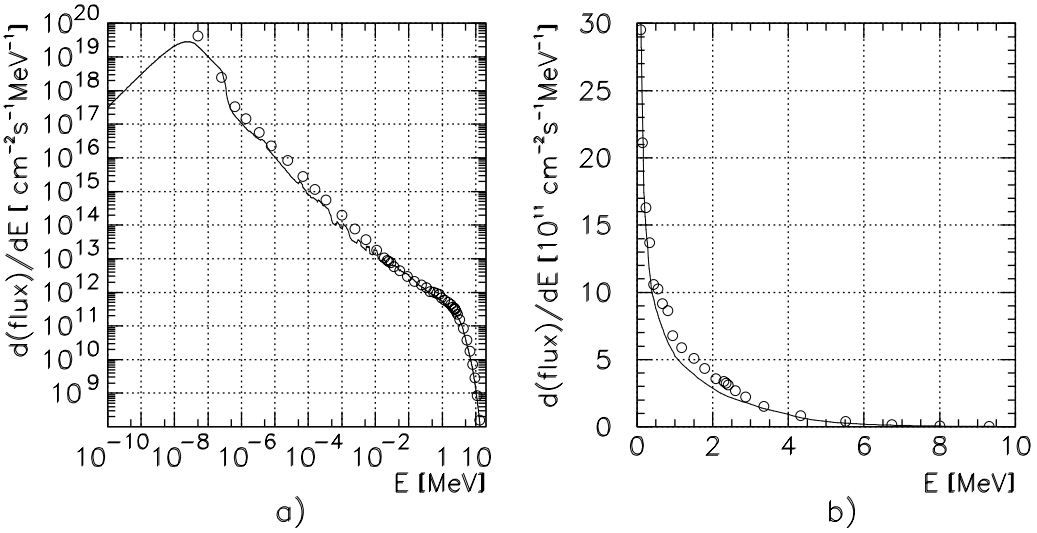

Figure 3.8: Measured [36] (full line) and simulated [38] (open circles) neutron spectrum in the irradiation channel F19. In figure a) logarithmic scale is used to present the full energy range while on the linear scale in figure b) only the fast neutron spectrum can be seen.

The simulation uses an iterative method to determine the neutron field in the reactor core [39]. The initial step assumes a point neutron source with Watt spectrum [37] in each rod and the effect of the neutrons from those sources on the generation of new sources in the core elements is determined. The calculation is repeated with recalculated element properties and source distribution until an equilibrium condition is reached. The neutron flux in the selected irradiation spot (in our case channel F19) is then determined from the neutron field in the equilibrium. A more detailed description of the procedure can be found in [41, 42].

Experimentally, measurement of the neutron spectrum was performed using the activation method [43]. It exploits the activation of different materials in the neutron field. Foil activation rate due to reaction i is determined by

$$r_i = \int_0^{E_{max}} \sigma_i(E)\phi(E)dE \ . \tag{3.3}$$

Foils with well known reaction cross-section for reaction i ($\sigma_i(E)$) are used for the measurement. Several foils of different materials are irradiated and activation rates are determined. The neutron spectrum is obtained from the solution of the system of integral equations 3.3. The error on the resulting spectrum depends on the number of different activated foils and on the sensitivity of the reaction cross-sections on neutron energy. Errors on the activation measurement, cross-section data, influence of other reactions and similar effects also contribute to the precision of the spectrum determination. Ten dif-

ferent reactions were used in the neutron spectrum measurement at channel F19. They were ^{197}Au(n,γ), ^{197}Au(n,γ)+Cd, ^{115}In(n,n'), ^{115}In(n,γ)+Cd, ^{27}Al(n,α), ^{58}Fe(n,γ)+Cd, ^{63}Cu(n,γ)+Cd, ^{63}Cu(n,γ), ^{59}Co(n,α) and ^{59}Co(n,p) [43]. The resulting spectrum is shown in figure 3.8.

Both simulation and measurement data were used to determine the κ value for this irradiation site. The same energy cuts were used as in the case of irradiation chamber, i.e. 0.1 - 15 MeV. The damage functions of Ougouag [27] and Griffin [44] were used to determine the κ value on measured data:

$$\kappa_{F19}^{Ougouag} = 0.90 \tag{3.4}$$

$$\kappa_{F19}^{Griffin} = 0.90 \ . \tag{3.5}$$

Due to good agreement of both calculations only the Ougouag damage function was used with the simulated spectrum

$$\kappa_{F19}^{sim} = 0.93 \ . \tag{3.6}$$

From these results, the κ value for irradiation site F19 was determined to be

$$\kappa_{F19} = 0.90 \pm 0.03 \ , \tag{3.7}$$

with error conservatively estimated from the diference between values 3.4 and 3.6.

To determine the contribution of neutrons with energy below 0.1 MeV, calculations within wider energy ranges were also performed. They showed that neutrons with energy below 0.1 MeV contribute an additional 1.5% to NIEL damage. Thus to determine neutron fluence, equivalent to 1MeV neutrons (eq. 2.49) the following equation was used throughout this work

$$\Phi_{eq}^{F19} = \kappa_{F19} \cdot (1 + 0.015) \cdot \Phi(E > 0.1MeV) \ . \tag{3.8}$$

The dosimetry in the irradiation channel was performed using Au activation (thermal neutron capture, decay time 2.7 days). Since this was also one of the foils used to determine the neutron spectrum it was possible to make a calibration of Au foil activation to flux above 0.1 MeV. The saturated activity for the reaction ^{197}Au(n,γ) of $4.8 \cdot 10^{-10}$ Bq per ^{197}Au atom was determined to correspond to fast neutron flux of $1.8 \cdot 10^{12}$ n/cm^{2}s. The systematic error of the method was estimated to about 15%.

This method is highly sensitive to changes of the spectrum since Au activation is sensitive to slow neutrons. Therefore fluence measurements for irradiations performed

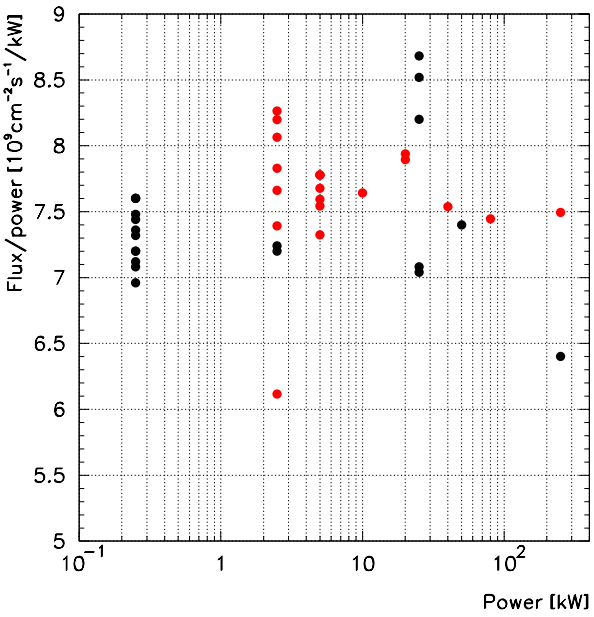

Figure 3.9: Flux of fast neutrons (E > 0.1 MeV) divided by reactor power versus the reactor power. The constant value of this ratio confirms the validity of the assumption that the neutron flux scales linearly with the reactor power. The scattering of measurements (RMS=3%) is within the error of the flux measurements.

after April 1998 are less reliable since the reactor core was going through a set of changes that may have affected the spectrum. For that reason a new measurement of the spectrum is planned after the new core configuration is set.

The homogeneity of the neutron field was determined by a separate measurement [43]. At the irradiation spot F19, the radial gradient was measured to be about 4%/cm and the vertical gradient about 1%/cm. Since the dosimetry foil was attached to the wall of the cylinder with rotational freedom, it induced an additional error of about 5% to the fluence measurement[22].

As already mentioned irradiations at the F19 channel were performed at different reactor powers, thus varying the neutron flux. It is expected that the neutron flux scales linearly with power. As can be seen in figure 3.9, measurements agree well with this expectation with $7.5 \cdot 10^9$ n/kWcm^{2}s of fast neutrons ($6.8 \cdot 10^9$ n/kWcm^{2}s of 1 MeV neutron equivalent).

[22] The radius of the irradiation cylinder was 1.3 cm.

3.5 Measurement Setup, Methods and Analysis

In the scope of this work, full depletion voltage (FDV) and bulk reverse current were measured on samples under study. The measurement setup as used in the laboratory is described while the one used at the reactor was described in section 3.3.2. Since both setups are only slightly different, the same measurement method and analysis were used.

3.5.1 Laboratory Setup

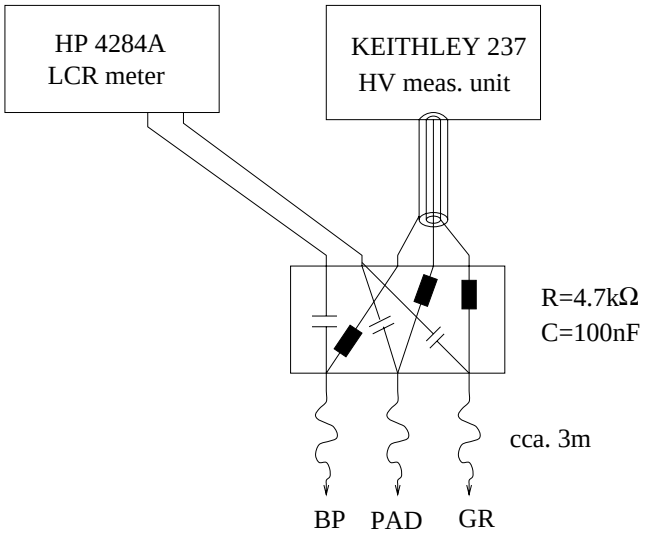

Figure 3.10: Measurement setup as used in the laboratory. BP, TOP and GR are connections to sample back plane, pad and guard ring, respectively.

The main components of the measurement setup were a LCR meter, a precise ampermeter and a high voltage source (up to cca. 1000 V). All units were computer controlled. In the laboratory, a HP4284A LCR measure unit and a KEITHLEY 237 high voltage source-measure unit were used. A Yokogawa UT15 temperature controller connected to a Pt100 sensor placed close to the sample was used to measure the sample temperature. All units were controlled and read out by a personal computer, where some on-line data analysis was also performed.

To measure the capacitance at different depletion depths, i.e. at different voltages, an external DC voltage has to be applied to the sample. In the laboratory, a KEITHLEY 237 high voltage source-measure unit was used as an external power source. It can provide DC voltage up to 1100 V with a current limit of 1 mA. To shield the LCR meter from high DC biasing voltages, decoupling capacitors were used as shown in figure 3.10. To reduce

the influence of changes in the small impedance of the voltage source on the measurements, decoupling resistors have been used (figure 3.10).

Most of the measurements were performed in a thermostat chamber at 5°C. When stored, samples were kept at stable temperature in one of the temperature stabilised chambers. For biasing during storage Wentzel high voltage power supplies were used. Annealing and reverse annealing have been accelerated by heating in an oven stabilised to 60°C, stable to about ±2°C. Temperature history during heating was measured by a Pt100 sensor, placed close to the sample and connected to a Yokogawa controller. The temperature read from the controller by computer and stored to a file. Measured temperature history was used to correct the equivalent heating time for temperature variations (eq. 4.5).

3.5.2 C/V Measurements

Full depletion voltage was determined from the kink in C/V plot (see section 2.1.6). It was used to determine the average effective dopant concentration according to equations 2.10 and 2.13.

Capacitance versus voltage curves were measured by Hewlet-Packard LCR meter. Capacitance is determined from the complex impedance. It is calculated from the measured amplitude and phase shift of the current signal in response to an AC measuring voltage with user selected frequency. The AC voltage amplitude can be set from 5 mV to 2 V. High measurement voltages give the advantage of better signal to noise ratio. They are however a significant disturbance at bias voltages of few volts. Thus at the reactor the amplitude of the measurement voltage was kept at 1 V due to harsh measurement conditions (long partially unshielded cables). At the laboratory, it was usually also kept at 1 V.

Both HP4284A and HP4263B[23] LCR meters provide means to transform measured complex impedance to different physical parameters according to a selected model. Since a partially depleted diode can be roughly described by an equivalent circuit as presented in figure 3.11, an adequate RC model should be selected. HP LCR-meters offer a serial and a parallel RC model, neither of them corresponding to the equivalent circuit. Thus an approximate influence of each component in the model from fig. 3.11 was estimated.

Let us consider the situation in a partially depleted diode of 1 cm^2 area and 300 μm thickness, irradiated to about 10^{14} n/cm^2, that being the most common situation in our studies. Measurement temperature of 5°C and measuring frequency of 10 kHz are assumed.

[23] A HP4263B LCR measure unit was used at the reactor, see section 3.3.2.

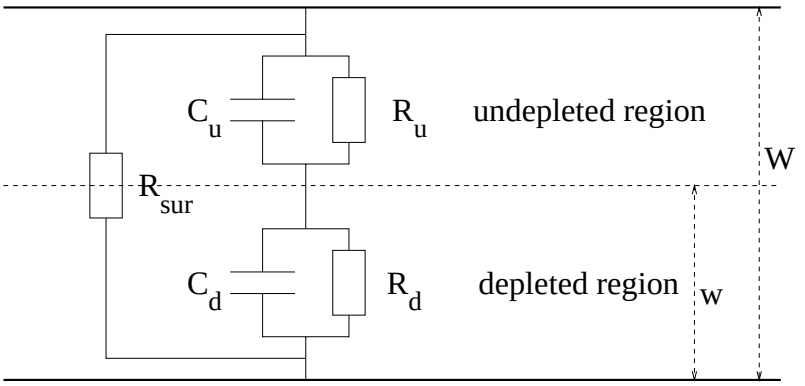

Figure 3.11: A simple model of a partially biased diode. Both depleted region and undepleted region are modelled by a capacitor C and a resistor R connected in parallel. Depleted and undepleted regions are connected in series with a parallel resistor to account for the surface current.

Capacitance of the depleted region can be determined by equation

$$C_d = \frac{\epsilon_{Si}\epsilon_0 S}{w} = \frac{C_0}{\sqrt{V'}} \ , \tag{3.9}$$

where w is the depletion depth, $C_0 = 35$ pF is capacitance of fully depleted diode and the dimensionless parameter $V' = V/V_{FD}$ is the fraction of full depletion voltage, applied across the depleted region. Similarly, capacitance of the undepleted region is given by

$$C_u = \frac{\epsilon_{Si}\epsilon_0 S}{W - w} = \frac{C_0}{1 - \sqrt{V'}} \ , \tag{3.10}$$

where W is the detector thickness. Corresponding impedances $Z = (2\pi\nu C)^{-1}$ for a 10 kHz measuring signal are

$$Z_d \approx 0.5\,M\Omega \cdot \sqrt{V'} \qquad Z_u \approx 0.5\,M\Omega \cdot (1 - \sqrt{V'}) \ , \tag{3.11}$$

decreasing inversly with measuring frequency.

Resistance of the undepleted bulk R_u for an inverted diode can be determined from the specific resistance for intrinsic bulk $\rho_{intr}(5°\mathrm{C}) \approx 1$ MΩcm. From it, one can obtain the resistance of the undepleted region in dependence of the depletion voltage

$$R_u = \rho\frac{W - w}{S} = \frac{\rho W}{S}(1 - \sqrt{V'}) = 30\,k\Omega \cdot (1 - \sqrt{V'}) \ . \tag{3.12}$$

The resistance of the depleted region can be determined from the DC current, flowing trough the diode[24]. According to eq. 2.38, the reverse current is proportional to the

[24]Since the reverse current is limited by the resistance of depleted region, this is a viable estimate.

width of depleted region w and consequently to $\sqrt{V}$, i.e. $I = A\sqrt{V}$. The magnitude of the parameter A can be estimated from the conditions at full depletion $A = \frac{I_{FD}}{\sqrt{V_{FD}}}$. Then the resistance of the depleted bulk at given depletion voltage is given by

$$R_d = \frac{V}{I} = \frac{V}{A\sqrt{V}} = \frac{\sqrt{V}}{A} = \frac{V_{FD}}{I_{FD}}\sqrt{V'} \tag{3.13}$$

Using reverse current of $I_{FD} \approx 25\ \mu$A at full depletion voltage[25] of $V_{FD} \approx 250$ V one obtains

$$R_d = 10\ M\Omega \cdot \sqrt{V'}\ . \tag{3.14}$$

One can see that in the described case $R_d/Z_d \approx 20$ and $Z_u/R_u \approx 15$. Thus the depleted region can be approximated by a capacitor and the undepleted by a resistor. The significance of the resistance of the undepleted region is however decreasing with increasing depletion depth. Thus at half of full depletion depth ($V = V_{FD}/4$), one already obtains $Z_d/R_u > 15$. Thus for large depletion depths the bulk can be described well by a single capacitor and both serial and parallel model should give the same result. The parallel model however has the advantage that it can take into account changes in the surface current, presented by the surface resistor. They are hard to predict but can get very important close to the breakdown where the differential resistance is small. Since for determination of full depletion voltage from the C/V characteristic, we are interested in its shape close to full depletion, the parallel model suits better and was used throughout this work.

The situation however changes dramatically when the measuring frequency is increased. This reflects in a decrease of impedance of both capacitors and at 1 MHz, Z_u has the leading role also in the undepleted region. Then the equivalent circuit can be approximated by two serial capacitors with a constant sum of capacitances. Thus at 1 MHz the measured capacitance is almost independent on applied voltage, as seen in figure 3.12. Similar effect is obtained by increasing the temperature. Since resistance of both depleted and undepleted region is approximately proportional[26] to $e^{-E_g/2k_BT}$, increasing the temperature for a few 10°C has the same relative effect as the above mentioned increase in frequency.

Static resistivities, used in the above estimation, do not describe the system very accurately. And although dynamic resistivities are somewhat different[27], the qualitative conclusions remain the same.

[25] Values of reverse current and full depletion voltage at the minimum after beneficial annealing were used.

[26] For depleted region see eq. 2.38 and for undepleted regions equations 2.11 and 2.1.

[27] A difference of up to about factor of two was estimated.

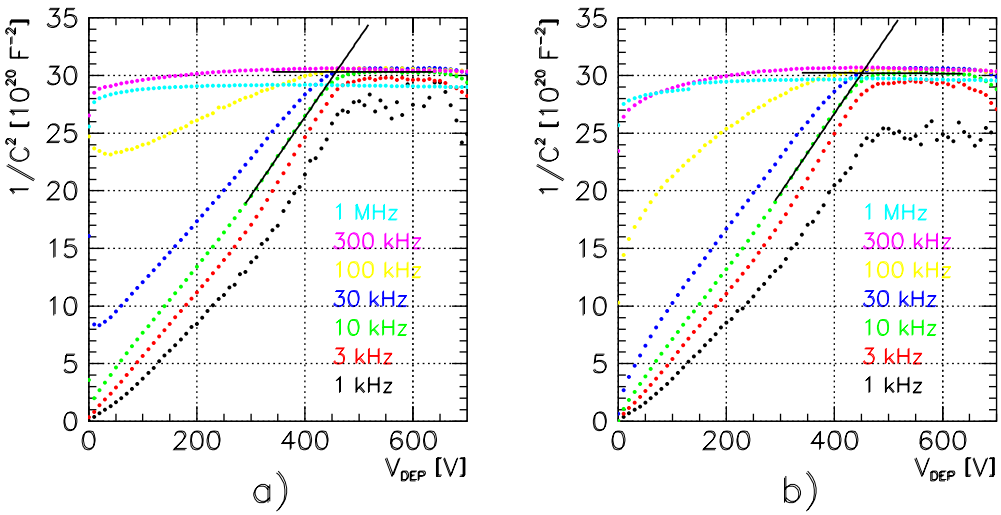

Figure 3.12: A comparison of a $1/C^2$ vs. voltage characteristics as obtained by a a) parallel and b) serial RC model. Straight line fits to the slope at large depletion depths and to the plateau at full depletion are also shown. The intersection of the lines was used to determine the full depletion voltage.

A comparison of results obtained by both models is shown in figure 3.12. As expected, at low depletion voltages better results are obtained from the serial model while results at high depletion depths are similar. It can however be noticed that the serial model gives a larger error of the value at the plateau for the lowest frequency (1 kHz). In that case parallel resistance is no longer negligible compared to capacitor impedance $\frac{1}{\omega C}$, leading to a larger error for the serial model. Full depletion voltages as obtained by both models agree within the errors.

The effect of the decoupling capacitors and resistors was taken into account by calibration. HP4284A enables frequency dependent calibration in a large frequency range while HP4263B can only be calibrated at one frequency, 10 kHz in our case. Calibration is done at open and closed circuit and with known load[28].

The measurement of the C/V characteristic was run by a custom written LabView program, running on a PC. Bias voltage (DC) was raised in predefined steps and sample capacitance was measured at each step with different frequencies of measuring (AC) voltage. Leakage current and sample temperature were also measured at each step. Measured capacitance was converted to $1/C^2$ and plotted in dependence of the bias voltage.

[28] A capacitor of 44 pF was used since this is an approximate capacitance of fully depleted 300 μm thick diodes with an area of 1 cm^2, used in this study.

The full depletion voltage was determined as the position of the kink in $1/C^2$ vs. voltage curve. The exact position of the kink was determined by the intersection of two lines, one fitted to the slope at large depletion depths and the second to the plateau at full depletion (see fig. 3.12). Fitted range was determined manually after a visual examination of the plot.

To determine the effective dopant concentration N_{eff}, a homogeneous distribution over the sample was assumed. In such case N_{eff} can be determined from the full depletion voltage by the equation

$$N_{eff} = \frac{2\epsilon_{Si}\epsilon_0}{e_0 W^2} V_{FD} \ . \tag{3.15}$$

The conversion factor depends on sample thickness and for 300 μm thick samples equation 3.15 can be written with a fixed numerical factor $N_{eff} = 1.44 \cdot 10^{10} V^{-1} cm^{-3} \cdot V_{FD}$.

The main sources of systematic error on determination of the full depletion voltage are in the selection of the measuring frequency and temperature. While measurements were performed at different frequencies (1 kHz, 3 kHz, 10 kHz, 30 kHz, 100 kHz, 300 kHz and 1 MHz in the laboratory and 100 Hz, 1 kHz, 10 kHz and 100 kHz at the reactor), a frequency of 10 kHz was most usually used to determine FDV. 10 kHz is a compromise between a good signal to noise ratio[29], sensitivity to traps with long trapping times and applicability of the simple RC model used.. Since it is also the most commonly used frequency of other groups, it also enables better comparison.

In the laboratory, all measurements were performed at 5°C to avoid the temperature effect. This was however not possible at the reactor, where measurements were performed at storage temperature.

The systematic error due to the sources listed above is estimated to be below 10%. The variations of FDV due to different selections of the fitted range for fits of the linear part at high depletion depths is on a percent level. That means that the largest contribution to the error on introduction rates of different defects comes from the 15% systematic error of the dosimetry.

3.5.3 Bulk Current

The time development of reverse bulk current has been studied together with N_{eff}. To separate bulk-generated current from the surface generated one, only diodes with guard rings were used in the analysis. While both guard ring and the pad were connected to the same potential, only current flowing through the pad was measured to reduce the contribution of the surface current.

[29] Impedance of capacitor is depending inversly on the frequency of the measurement voltage.

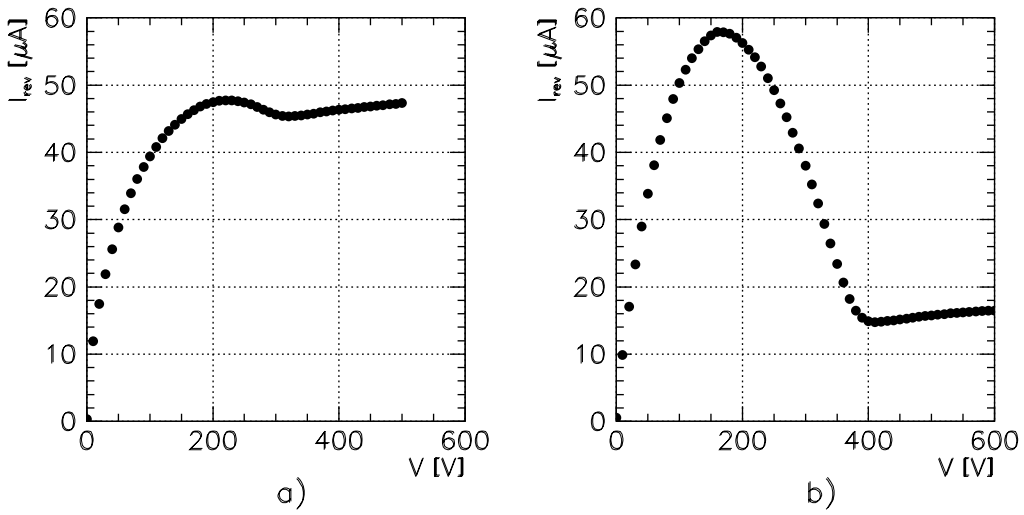

Figure 3.13: I/V measurement of the diode K3. Guard rings were kept at the same potential as the pad but their current is not included in the measurement. Measurement a) was taken 5 days after irradiation (stored at 5°C) and was performed at 5°C. The full depletion voltage from the C/V measurement at 10 kHz is 306±10 V, agreeing well with the position of the minimum in the I/V curve. Value in the minimum after the bump (45 μA) is taken as the value of the bulk generation current at full depletion. b) Measurement of the same diode taken after total of 5 days at 60°C.

From equations 2.38 and 2.9 it follows that the bulk generation current is increasing as the square root of the depletion voltage until the sample is fully depleted and the values at the plateau could be used to determine α (eq. 2.50). The I/V curve of an inverted p^+-n-n^+ diode (fig. 3.13) however deviates from the expected $I \propto \sqrt{V}$ shape. A characteristic bump can be observed on all samples after inversion. The explanation has been proposed in [51]. After inversion, the depleted region starts to grow from the n side while guard rings are on the p side. For low depletion voltages, the surface current is thus not fully collected by guard rings, contributing to the current measured on the central pad. When the sample is fully depleted guard rings are fully operational again (fig. 3.13). Thus throughout this work, the leakage current at the minimum after the bump has been used as the best estimate of the bulk generation current.

The main contribution to the error comes from the surface current that remains present at the minimum after the bump. As can be seen from data presented later (e.g. fig. 4.16), this contribution is rather small for diodes with working guard rings. The variations of the alpha parameter determined by this method are at the level of few

percent. Thus the main contribution to the error on α comes again from 15% of systematic error on dosimetry.

3.6 Summary

Two irradiation sites at the TRIGA reactor at the reactor research center in Ljubljana were equipped to enable irradiations of silicon samples with fast neutrons. Irradiation set-ups provide mounting, cooling and biasing of samples and on-line C/V and I/V measurements.

Irradiation chamber enables irradiation of samples with dimensions up to about 10×15 cm^2. Samples can be cooled down to about -20°C via Peltier cooling. A fission plate is used to increase the fast neutron flux. Thus, the maximal flux of fast neutrons (above 0.1 MeV) is about $4 \cdot 10^8$ n/cm^{2}s and is determined with an error of about 15%. An existing measurement of the neutron spectrum was used to determine the relative damage factor κ to $\kappa_{IC} = 0.99 \pm 0.06$. The neutron dose equivalent to 1 MeV neutrons is thus determined with an error of about 17%.

Irradiation channel F19 provides fast neutron fluxes in the range from about 10^9 n/cm^{2}s to $2 \cdot 10^{12}$ n/cm^{2}s and about $5 \cdot 10^{15}$ n/cm^{2}s in the pulsed mode. Sample dimensions are limited to about 15×50 mm^2 and liquid cooling down to 0°C is provided. The neutron spectrum has been determined by measurements and simulation, and damage factor relative to 1 MeV neutrons was determined to $\kappa_{F19} = 0.90 \pm 0.03$. Fluence of the fast neutrons is determined with a systematic error of about 15% and an additional error of about 5% on the dosimetry of individual sample. Thus irradiation fluence equivalent to 1 MeV neutrons can be determined with an error of approximately 15%(syst.) + 5%(ind.).

At the time of concluding this work, another channel similar to F19 is being finished. It will enable irradiation of larger samples (up to approximately 5×5 cm^2) and cooling to about -10°C.

Full depletion voltage was determined from C/V measurements. It has been qualitatively shown, that a simple parallel RC model is an adequate description of an irradiated diode for a measuring AC signal with a frequency of about 10 kHz. The errors on the measured full depletion voltage are estimated to be below 10%, while the error on reverse current is at the level of few percent.

4

Time Development of Defects

In this chapter results of the study of time development of radiation-induced defects are presented. The study consists of measurements of two detector properties they influence, full depletion voltage and generation current (bulk reverse current).

Time development of full depletion voltage (or N_{eff}) is described by equation 2.65. Since time constants for the annealing and reverse-annealing part differ by about two orders of magnitude (around room temperature order of days for annealing compared to about a year for reverse annealing) both phenomena have been studied separately. Due to large amounts of data available for the slow part of annealing (time scale of days at room temperature) [14, 18, 19, 21, 45, 46] this work is only dealing with the fast part (time scale of hours) where data are rather scarce. Results of this study are presented in the first section. In the second section reverse annealing of N_{eff} is discussed with the purpose to determine the dynamics of responsible processes (first or second order). Finally, in the third section, results on time development of reverse current are presented.

4.1 Fast Annealing of N_{eff}

According to equation 2.65 and neglecting reverse annealing on the time scale of measurements[30] the initial stage of N_{eff} time development can be described by

$$N_{eff}(t) = g_C \cdot \Phi_{eq} + \sum_i g_i \Phi_{eq} e^{-t/\tau_i} \ . \tag{4.1}$$

Here g_i are introduction rates and τ_i decay time constants of unstable defects and g_C introduction rate of defects stable in time.

[30] Reverse annealing contributes a few percent of constant level during one week at 15°C and less at lower temperatures.

Sample	process	No. of GR	V^0_{FD} [V]	T	ϕ_{eq} [n/cm^{2}s]	Φ_{eq} [n/cm^2]
K3	planar	3	6	5°C	$1.9 \cdot 10^9$	$1.03 \cdot 10^{14}$
I3	planar	3	24	5°C	$1.9 \cdot 10^9$	$4.4 \cdot 10^{13}$
D3	planar	3	16	15°C	$1.8 \cdot 10^9$	$4.7 \cdot 10^{13}$
D1	planar	3	26	15°C	$1.9 \cdot 10^{10}$	$4.2 \cdot 10^{13}$
B3	planar	3	20	0°C	$1.9 \cdot 10^9$	$4.4 \cdot 10^{13}$
G3	planar	3	23	0°C	$1.8 \cdot 10^9$	$8.3 \cdot 10^{12}$
G2	planar	3	20	0°C	$1.8 \cdot 10^{10}$	$8.7 \cdot 10^{12}$

Table 4.1: List of diodes used in study of fast annealing of N_{eff}. Processing type, no. of guard rings, full depletion voltage before irradiation, irradiation/storage temperature, irradiation flux and fluence normalised to 1 MeV neutrons are given for each sample. Thickness of samples was 300±5 μm.

In case of irradiation times t_{irr} comparable with decay time constants τ_i, annealing during the irradiation should be taken into account. In that case equation 4.1 is generalised to

$$N_{eff}(t) = \begin{cases} [g_C t + \sum_i g_i \tau_i (1 - e^{-t/\tau_i})] \cdot \phi_{eq} & ; \ t < t_{irr} \\ [g_C t_{irr} + \sum_i g_i \tau_i (e^{t_{irr}/\tau_i} - 1) e^{-t/\tau_i}] \cdot \phi_{eq} & ; \ t_{irr} < t \end{cases} \tag{4.2}$$

A set of 7 samples was used to study fast annealing of N_{eff}. They are listed in table 4.1 together with their irradiation conditions. Samples were processed by Micron on Wacker high-resistivity ($\rho \approx$>10kΩcm) wafers using a planar process.

Time development of N_{eff} during irradiation for samples D3, I3 and B3 is shown in figure 4.1a and their annealing after irradiation in figure 4.1b. Those three samples were irradiated and kept at identical conditions except for the temperature (15°C, 5°C and 0°C respectively).

Evolution of defects during the irradiation is affected by both defect creation and their annealing, while only the defect annealing is taking place after the irradiation. Thus fit according to equation 4.2 was first attempted on the data measured after the irradiation (fig. 4.1b). Results of the fitting show that the early stage of defect development can be perfectly fitted with a constant and two exponentials

$$N_{eff}(t) = [g_0 t_{irr} + \sum_{i=1,2} g_i \tau_i (e^{t_{irr}/\tau_i} - 1) e^{-t/\tau_i}] \cdot \phi_{eq} \quad ; \ t_{irr} < t \tag{4.3}$$

indicating fast annealing of two defects.

Figure 4.1 indicates systematically higher values of N_{eff} for lower temperatures, attributed to defect freezing [46]. This effect is however not obvious in the fit results

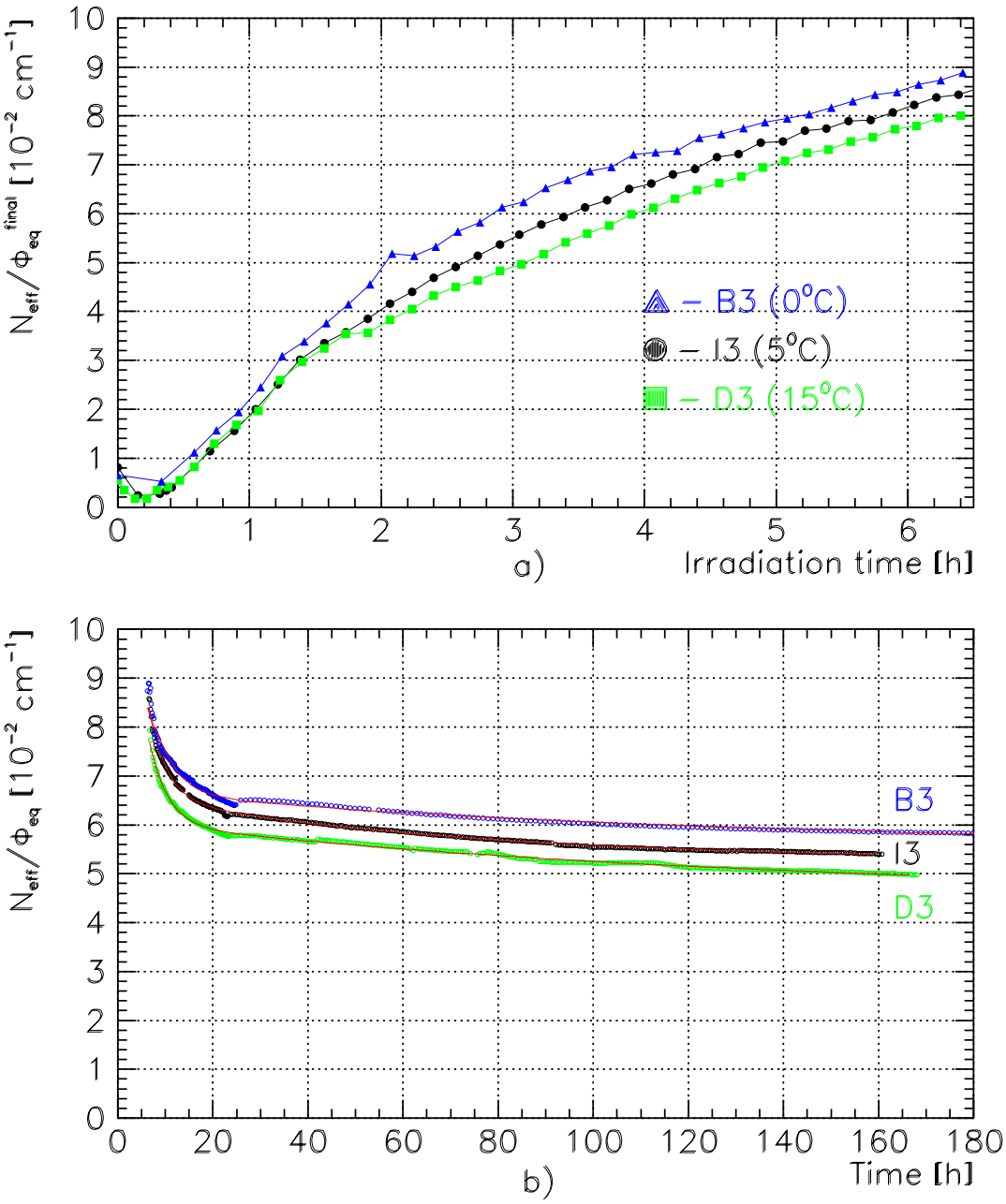

Figure 4.1: Development of N_{eff} a) during and b) after irradiation for samples D3, I3 and B3. The samples were treated identically except for the temperature that was 15°C, 5°C and 0°C, respectively. In figure a) type inversion point can be seen at 0.2 h. In figure b) the fit according to eq. 4.3 (red lines) fits the measured data perfectly.

Sample	T [°C]	g_0 [10^{-2}/cm]	g_1 [10^{-2}/cm]	τ_1 [h]	g_2 [10^{-2}/cm]	τ_2 [h]
D3	15°C	4.3	3.6	4.0	1.7	170
D1	15°C	4.5	2.5	3.9	1.3	37
K3	5°C	4.3	1.7	9.3	1.1	79
I3	5°C	5.1	3.9	3.7	1.3	68
B3	0°C	5.5	4.1	4.4	1.1	110
G3	0°C	6.4	7.3	3.5	4.3	16
G2	0°C	4.3	8.0	3.8	4.9	47

Table 4.2: List of samples and irradiation temperatures with values of the fit parameters according to eq. 4.3.

as given in table 4.2. They indicate a fast component with a time constant of about 4 hours with almost no temperature dependence. Its introduction rate however shows no systematic behaviour. As discussed in chapter 6, a qualitative explanation could be found in the effect of reverse bias on the defect development. The situation is similar with the slow and constant component. There the reason probably lies also in the relatively short time-range of the fit. Therefore the temperature dependence of the slow component as reported by Ziock et al. [45] could not be determined. After heating to 60°C N_{eff} at the minimum is equal for all planar detectors with an introduction constant for stable defects g_C=0.04 cm^{-1}. Temperature independent values at minimum were also reported by other authors [14, 21, 46].

Development of N_{eff} has also been monitored during the irradiation (fig. 4.1a). As the irradiation time is comparable with the lifetime of the fast component, the time development[31] of N_{eff} is expected to deviate from a straight line. Results of the measurements during the irradiation (figure 4.1a) agree with those expectations. They can however not be reproduced well using the introduction rates and decay constants as obtained from the fit after the end of irradiation. This may be the consequence of initial dopant removal and the bias effect (see chapter 6).

Since frequent measurements of the C/V characteristic caused samples to be only partially biased (not totally depleted) for a significant portion of time, the annealing constants presented in this chapter can not be claimed valid for fully biased samples. Also, the bias voltage of 200V, that was adopted as a standard, was not sufficient to fully bias all samples during and immediately after the irradiation. For that reason it is important to notice that the present results, especially during irradiation and in the very early stage of annealing, are affected by the annealing of bias-dependent defects. This

[31] Since samples were irradiated with a constant neutron flux, the accumulated fluence is proportional to the irradiation time.

effect and its influence on the measurements are discussed further in chapter 6.

4.2 Reverse Annealing of N_{eff}

Reverse annealing of N_{eff} was studied to determine the type of the process responsible. This knowledge is important for a prediction of radiation damage at the LHC. In case of a first order process (eq. 2.57) the reverse annealing time constant k_1^Y does not depend on the fluence while in case of a second order process (eq. 2.61) $k_2^Y N_X$ depends on fluence linearly ($N_X \propto \Phi$).

Two different methods were used in this work to determine the type of the reaction responsible. In the first one, samples were fully reverse annealed and reaction equations for first and second order processes were fitted to the data. In the second only the slope at the beginning of the reverse annealing was studied, with its dependence on irradiation fluence.

4.2.1 Reaction Kinematics Fit

A set of 10 samples was used to study reverse annealing by fitting reaction kinematics. All samples were 1×1 cm^2 p^+-n-n^+ diodes with 3 guard rings, produced by planar process at Micron on Wacker wafers. The irradiation conditions are given in table 4.3. About a week after irradiation the heating procedure was started, in order to accelerate defect development. Samples were heated to 60°C for increasing time intervals interrupted by C/V and I/V measurements at 5°C. The sample temperature was monitored and the heating time was corrected (eq. 4.5) for small deviations from 60°C.[32] Total heating times from one month to few months at 60°C were accumulated, depending on the sample. All samples were reverse biased to 200 V during and after the irradiation[33], including the heating periods[34]. Though not all samples were irradiated at the same temperature these effects could be neglected after a few hours at 60°C. Nevertheless, this was accounted for, using equation

$$k(T) = k_0 e^{-\frac{E_a}{k_B T}} \ , \tag{4.4}$$

giving

$$k(T_2) = k(T_1) e^{\frac{E_a}{k_B}(\frac{1}{T_1} - \frac{1}{T_2})} \ . \tag{4.5}$$

[32]Sample temperature during the heating periods was stable to about ±2°C.

[33]Except for the P0 samples (P0A and P0B, irradiated in the pulse mode) that were not biased all the time during the first few days at -10°C.

[34]Due to voltage-source current limit of 3 mA for some highly irradiated samples the bias voltage during heating was somewhat lower, but never below 140 V.

Sample	V_{FD}^0 [V]	T	ϕ_{eq} [n/cm^{2}s]	Φ_{eq} [n/cm^2]
K3	6	5°C	$1.9 \cdot 10^9$	$1.03 \cdot 10^{14}$
K1	32	5°C	$3.7 \cdot 10^{11}$	$1.02 \cdot 10^{14}$
K0	32	5°C	$1.6 \cdot 10^{12}$	$1.04 \cdot 10^{14}$
P0A,B	8	-10°C	$\approx 5 \cdot 10^{15}$	$1.12 \cdot 10^{14}$
I3	24	5°C	$1.9 \cdot 10^9$	$4.4 \cdot 10^{13}$
D3	16	15°C	$1.8 \cdot 10^9$	$4.2 \cdot 10^{13}$
B3	20	0°C	$1.9 \cdot 10^9$	$4.4 \cdot 10^{13}$
G3	23	0°C	$1.8 \cdot 10^9$	$8.3 \cdot 10^{12}$
G2	20	0°C	$1.8 \cdot 10^{10}$	$8.7 \cdot 10^{12}$

Table 4.3: List of diodes used in the study of reverse annealing of N_{eff} with model fits. Full depletion voltage before irradiation, irradiation/storage temperature, irradiation flux and fluence normalised to 1MeV neutrons are given for each sample. The thickness of samples was 300±5 μm.

Value of the activation energy E_a for the reverse annealing of N_{eff} is about 1.3 eV [13, 14, 15] and for annealing of reverse current about 1.1 eV [15]. Thus, the time development of N_{eff} at 60°C is almost 500 times faster than at 20° and for time development of reverse current this factor is about 190.

Since annealing time constants are much shorter than those for the reverse annealing it is possible to study reverse annealing independently by waiting for annealing to complete. The effect of reverse annealing during the time interval of beneficial annealing is negligible as can be seen from figures 4.5. Thus, assuming annealing to be completed and using equations 2.65, 2.57 and 2.61 one can set an ansatz for both processes as

$$N_{eff}(t) = g_C \Phi_{eq} + g_Y \Phi_{eq}(1 - e^{-k_1^Y t}) \tag{4.6}$$

for the first order process and

$$N_{eff}(t) = g_C \Phi_{eq} + g_Y \Phi_{eq}(1 - \frac{1}{1 + g_Y \Phi_{eq} k_2^Y t}) \tag{4.7}$$

for the second order. There g_C is the introduction rate for defects constant in time, g_Y for defects responsible for reverse annealing and Φ_{eq} the irradiation fluence normalised to 1 MeV neutrons. Fits of first and second order ansatz are shown in figure 4.2 and 4.3 and their results given in table 4.4.

Comparison of χ^2/ndf values from table 4.4 shows that though in most cases the second order fit is somewhat better than first order, the difference is not large enough to exclude a first order reaction. Even more so because fits in figures 4.2 and 4.3 show that first order mainly fails at the late stage of reverse annealing.

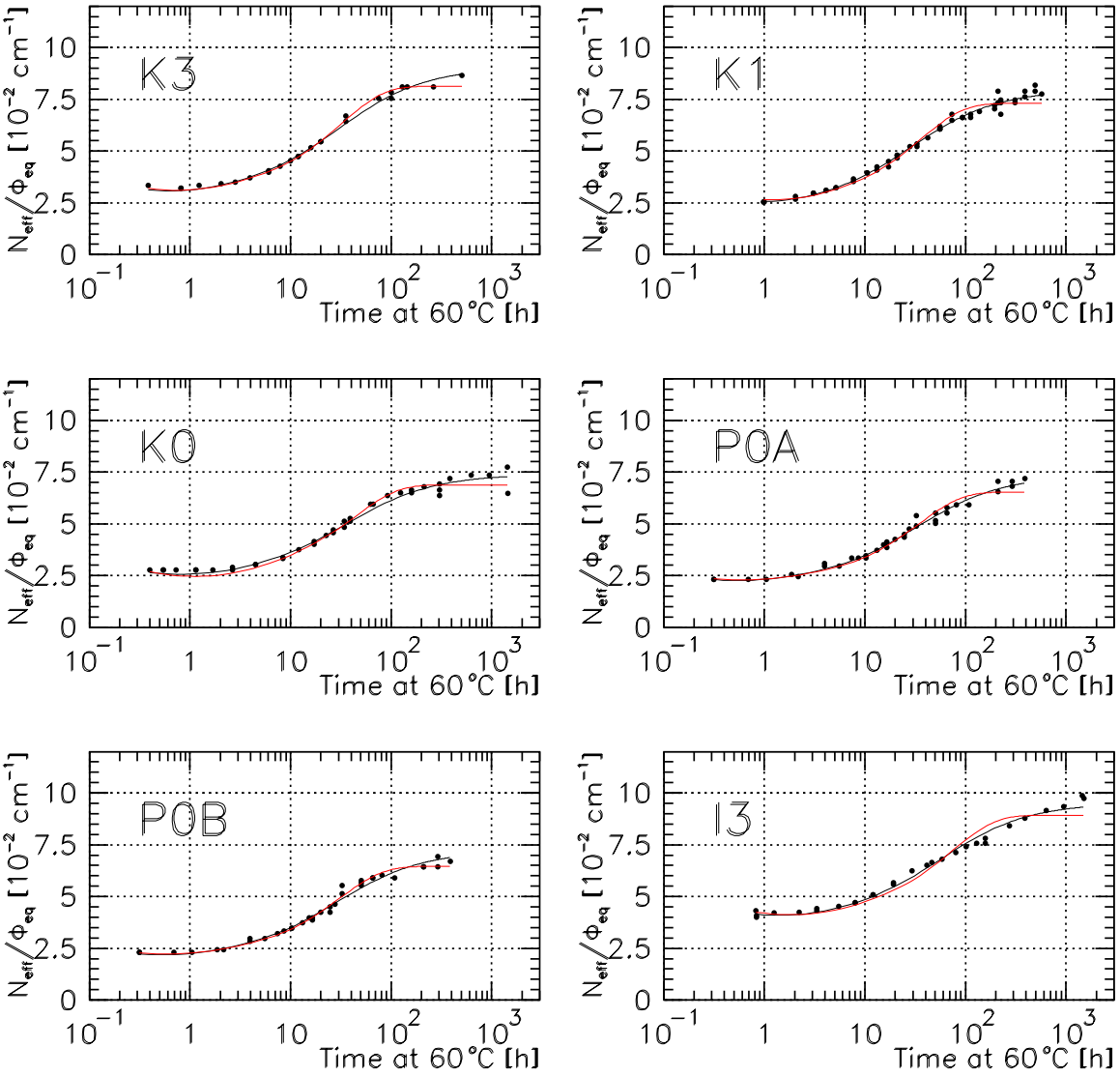

Figure 4.2: First order (red line) and second order (black line) fits for diodes K3, K1, K0, P0A, P0B and I3. N_{eff}/Φ_{eq} versus heating time at 60°C is displayed.

Another test to differentiate between the models is the dependence of reaction constants k_1^Y and k_2^Y on irradiation fluence. For the correct model they should be fluence independent while for the wrong one they should depend on fluence. As can be seen from figure 4.4, the first order reverse annealing constant k_1^Y indicates linear dependence on fluence $k_1^Y \propto \Phi_{eq}$ while the second order constant k_2^Y shows somewhat weaker fluence dependence. Though these results favour second order dynamics against first order one,

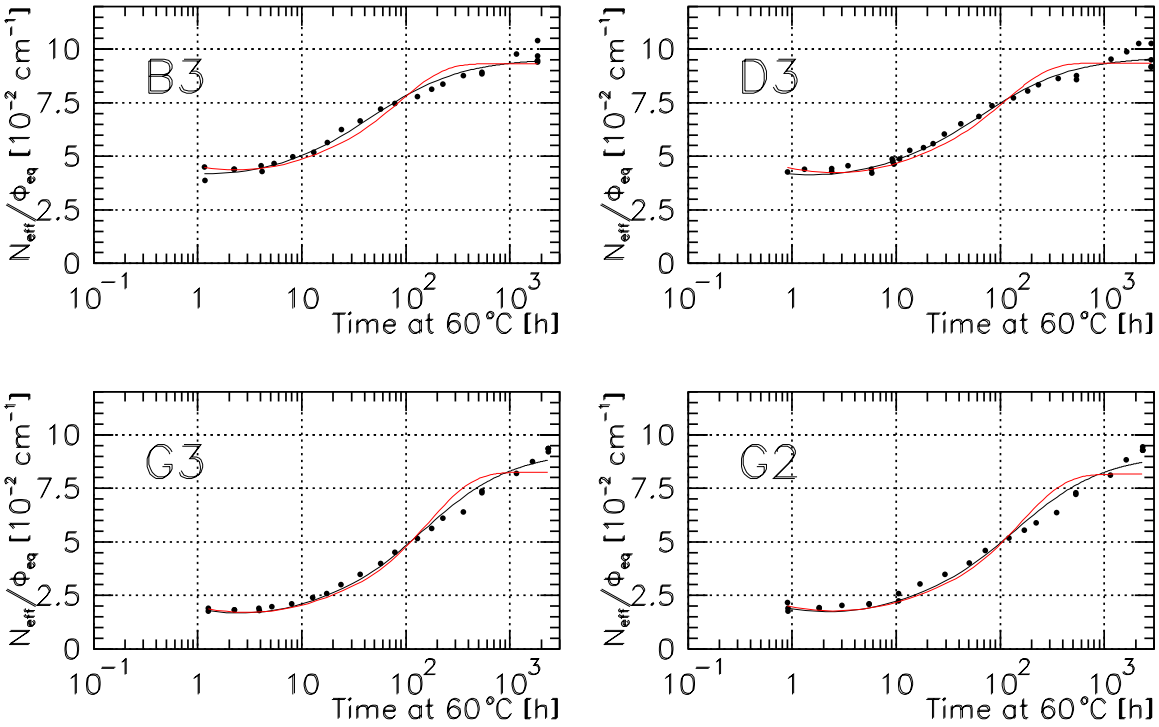

Figure 4.3: First order (red line) and second order (black line) fits for diodes B3, D3, G3 and G2. N_{eff}/Φ_{eq} versus heating time at 60°C is displayed.

we do not yet consider them as conclusive evidence.

Fluence dependence of reverse annealing constants is however affected by partial bias of the samples. Namely, all samples were biased with 200 V. Thus samples irradiated to low fluences were strongly over-biased while those irradiated to high fluence were only partially depleted. Also, for highly irradiated samples, the depleted depth was decreasing with reverse annealing due to the raise of FDV. And since, as shown in chapter 6, biased regions have higher N_{eff} than unbiased ones, this reflects in time development of an average N_{eff}. As this represents the quantity used in the study of reverse annealing, partial bias affects values of the reverse annealing parameters.

Sample	g_C [10^{-2}/cm]		g_Y [10^{-2}/cm]		$k^Y(60°C)$ [10^{-6}/s]	[10^{-18}cm^3/s]	χ^2/ndf	
	1^{st} or.	2^{nd} or.	1^{st} or.	2^{nd} or.	1^{st} or.	2^{nd} or.	1^{st} or.	2^{nd} or.
K3	3.1	3.0	5.0	6.0	8.8	1.51	0.6	0.7
K1	2.5	2.4	4.7	5.6	7.8	1.70	2.1	0.8
K0	2.6	2.6	4.2	4.8	6.4	1.54	1.5	1.8
P0A	2.3	2.3	4.2	5.1	7.6	1.45	3.1	2.0
P0B	2.3	2.3	4.2	4.9	8.4	1.61	2.8	3.5
I3	4.0	3.9	4.5	5.3	3.8	2.12	3.0	1.0
D3	4.2	4.1	4.9	5.5	3.3	1.86	3.0	1.6
B3	4.1	4.0	4.8	5.4	4.5	2.54	3.9	1.8
G3	1.8	1.7	6.5	7.5	1.6	3.12	8.2	2.6
G2	1.9	1.9	6.3	7.2	1.6	3.27	11.5	5.2

Table 4.4: Results of the fits using first order and second order models. Generation rates for defects constant in time (g_C) and ones responsible for reverse annealing (g_Y) are given together with reverse annealing constants k_1^Y and k_2^Y. χ^2/ndf (ndf - number of degrees of freedom) is given for both fits to compare agreement of both models with measured results. Errors on k^Y are about 5%.

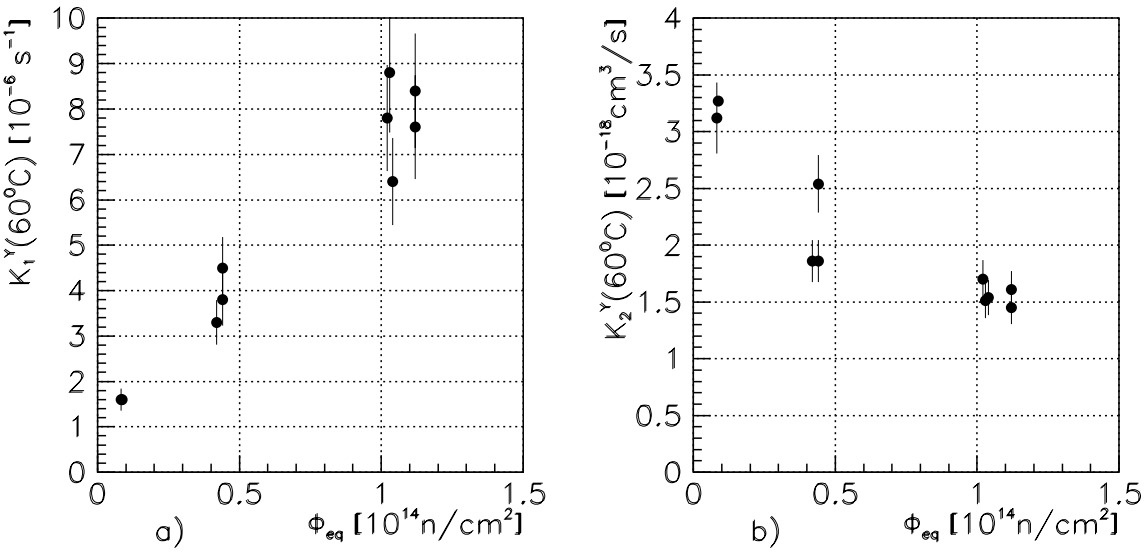

Figure 4.4: a) First order and b) second order reverse annealing constants k_1^Y and k_2^Y in dependence of irradiation fluence. First order assumption shows $k_1^Y \propto \Phi_{eq}$ dependence while k_2^Y shows somewhat weaker fluence dependence.

4.2.2 Initial Slope Fit

During the initial stage of reverse annealing, i.e. for $k_1^Y t \ll 1$ and $g_Y \Phi_{eq} k_2^Y t \ll 1$ for first and second order processes respectively, equations 4.6 and 4.7 can be linearised to

$$\frac{N_{eff}(t)}{\Phi_{eq}} = g_C + g_Y k_1^Y t \tag{4.8}$$

for the first order and

$$\frac{N_{eff}(t)}{\Phi_{eq}} = g_C + g_Y^2 \Phi_{eq} k_2^Y t \tag{4.9}$$

for the second order. Thus, if we write

$$\frac{N_{eff}(t)}{\Phi_{eq}} = g_C + k_Y^{lin} t \tag{4.10}$$

the slope k_Y^{lin} at the initial stage of reverse annealing is not fluence dependent for the first order process and is increasing linearly with fluence for the second order process and is the main difference between first and second order processes. A comparison of slopes $k_Y^{lin}(\Phi_{eq})$ can thus indicate the process responsible for reverse annealing.

Two sets of samples were used for this study. In the first were the diodes K3,K1, K0, P0A, P0B, I3, B3, D3, G3 and G2 that were reverse annealed at 60°C under bias. Their characteristics and irradiation conditions were presented in the previous subsection (table 4.3). In the second (RAN) set are 8 diodes irradiated and annealed with no bias. Those were planar Sintef p^+-n-n^+ diodes with multiple non-connectable guard rings and dimensions 6×6 mm^2 (B diodes) and 5×5 mm^2 (M diodes). They were irradiated in four pairs (one B and one M diode in each pair) to four different fluences (table 4.6). To assure identical conditions during annealing and reverse annealing they were all mounted on the same metalised glass plate and kept at 20°C.

Time development of N_{eff} at the initial stage of the reverse annealing for diodes annealed at 60°C is shown in figure 4.5. Results of the fit according to eq. 4.10 are presented in table 4.5 and figure 4.6.

Contrary to the results from the reaction kinematics fit, results from the fit of the initial slope slightly favours a first order process. However both k_Y^{lin} and k_Y^{lin}/Φ_{eq} are fluence dependent and do not give clear evidence for any of the two proposed models. The samples however are the same as used for reaction kinematics fit in the previous section. Thus the influence of partial bias as given there also applies to the results of the initial slope fit. The influence of the bias effect is however somewhat reduced since the changes in FDV (and thus changes in the portion of the region undepleted by 200 V) are

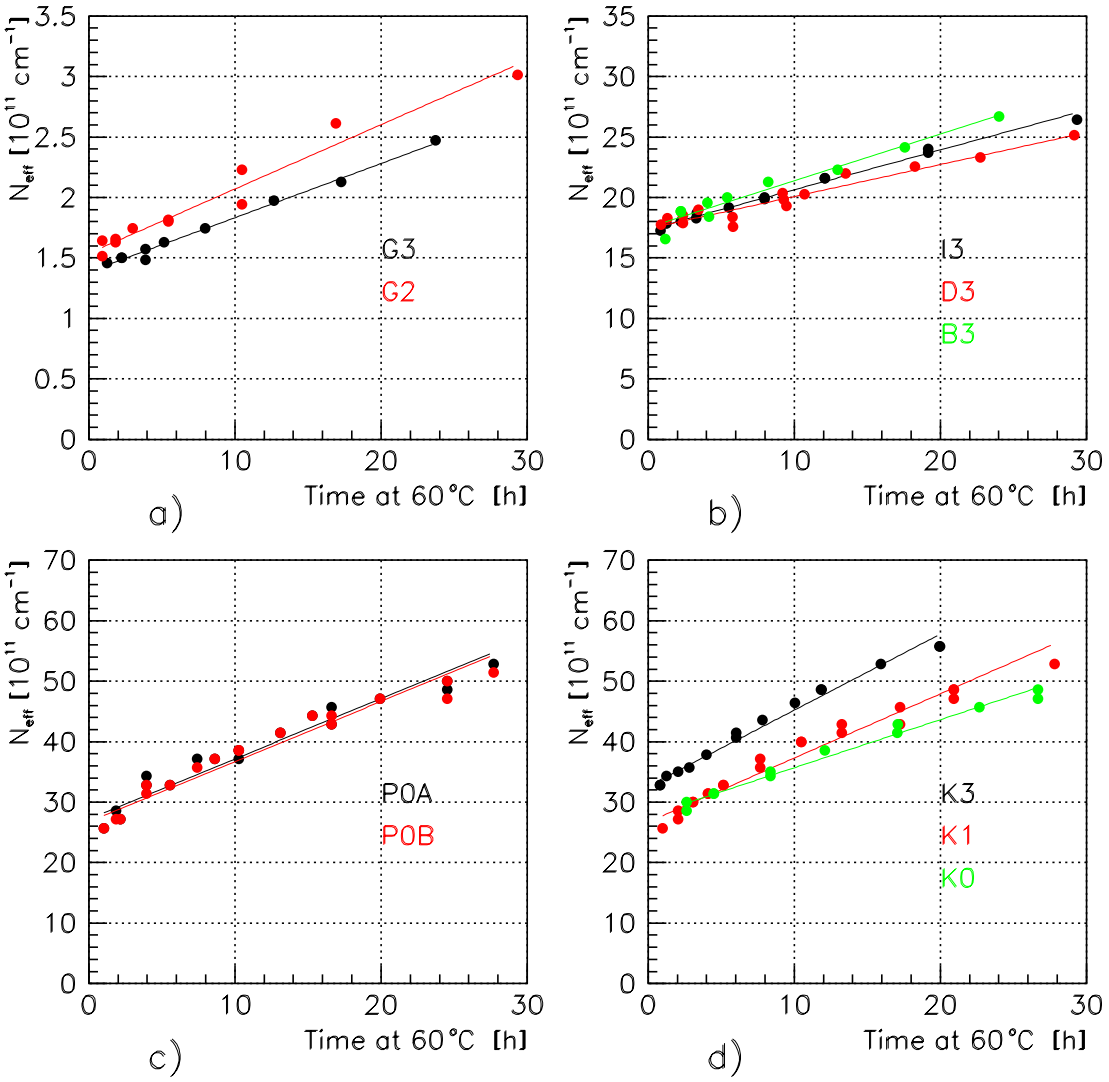

Figure 4.5: Time dependence of N_{eff} at the initial stage of the reverse annealing for a) samples G3 and G2, b) samples I3, D3 and B3, c) samples P0A and P0B and d) samples K3, K1 and K0.

smaller. To obtain conclusive result, a set of diodes fully biased or unbiased during the complete treatment was necessary. Thus a set of diodes was dedicated to this type of analysis (RAN set).

The diodes from the RAN set were unbiased and kept at 20°C during the study. After the annealing stage was completed, time development of N_{eff} was fitted according to equation 4.10. The development of N_{eff} at the initial stage of reverse annealing is

Sample	g_C $[10^{-2}\mathrm{cm}^{-1}]$	k_Y^{lin} $[10^{-7}\mathrm{cm}^{-1}\mathrm{s}^{-1}]$
K3	3.2	3.4
K1	2.6	2.9
K0	2.7	2.1
P0A	2.4	2.5
P0B	2.4	2.5
I3	4.0	2.2
D3	4.2	1.8
B3	4.1	2.6
G3	1.7	1.5
G2	1.8	1.7

Table 4.5: Results of the linear fit for the initial stage of reverse annealing for diodes annealed at 60°C under bias. Errors on k_{lin}^Y are about 5%.

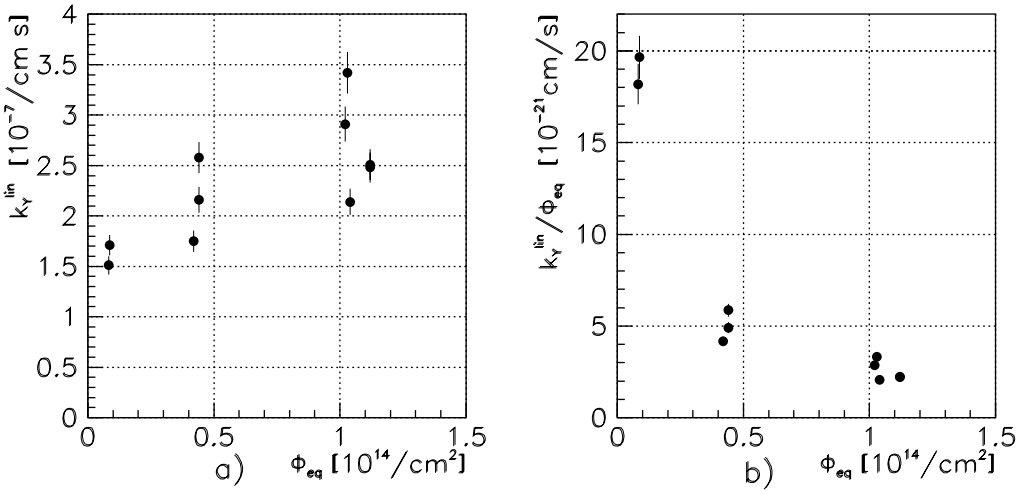

Figure 4.6: a) k_Y^{lin} and b) k_Y^{lin}/Φ_{eq} for the group annealed at 60°C. In case of a first order dynamics, the distribution in figure a) should be flat, while for second order, the distribution b) should be flat.

shown in figure 4.7, together with the fit. Results of the fit are presented in table 4.6 and figure 4.8.

Comparison of N_{eff}/Φ_{eq} for all 8 samples annealed with no bias at 20°C is shown in figure 4.9 where it can be clearly seen that reverse annealing slopes k_{lin} are not fluence dependent. Disagreement in the introduction rates of the stable defects g_C can be explained by donor removal. While it has not been taken into account it may have still

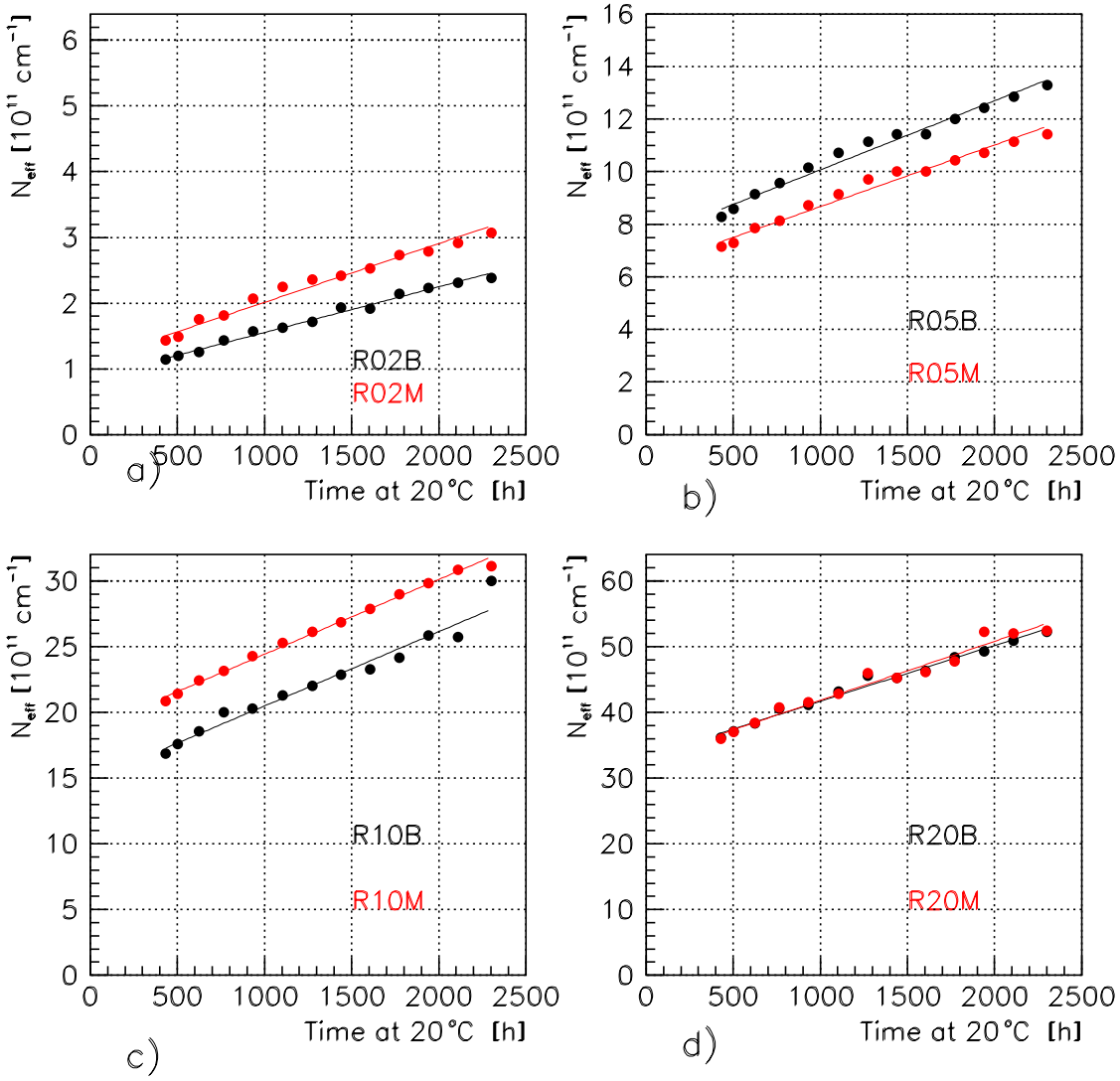

Figure 4.7: Development of N_{eff} at the initial stage of the reverse annealing for a) samples R02B and R02M, b) samples R05B and R05M, c) samples R10B and R10M and d) samples R20B and R20M.

not been completed for the samples irradiated to the low fluences[35]. This explanation is supported by the fluence dependence of effective g_C as shown in figure 4.10.

Measurements of the set annealed at 20°C clearly point to the first order model during the initial stage of reverse annealing. Disagreement of other samples with the the

[35]It has to be considered that the RAN samples had for about a factor of 2 higher initial full depletion voltage (effective dopant concentration) than the rest of the samples used in this work, enhancing the effect of incomplete donor removal.

Sample	V^0_{FD} [V]	ϕ_{eq} [10^{11} n/cm^{2}s]	Φ_{eq} [10^{14} n/cm^2]	g_C [10^{-2}cm^{-1}]	k_Y^{lin} [10^{-10}cm^{-1}s^{-1}]
R02B	45	2.1	0.21	0.42	9.1
R02M	41	2.1	0.21	0.57	11.3
R05B	39	2.1	0.53	1.4	13.5
R05M	40	2.1	0.53	1.2	12.0
R10B	47	2.1	1.06	1.4	15.3
R10M	47	2.1	1.06	1.8	14.9
R20B	41	2.1	2.1	1.6	11.1
R20M	44	2.1	2.1	1.6	11.8

Table 4.6: Full depletion voltage, irradiation conditions and results of the linear fit for the initial stage of the reverse annealing for diodes annealed at 20°C. Errors on k^Y_{lin} are about 5%.

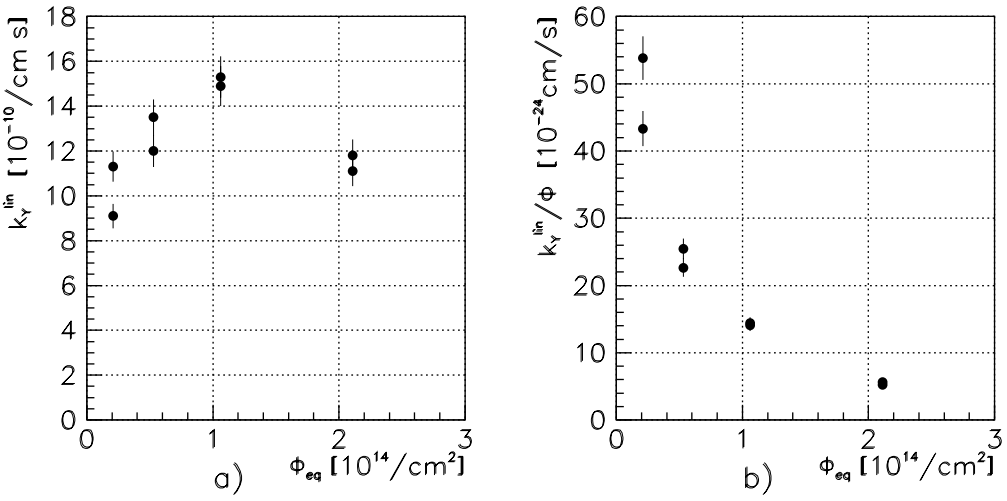

Figure 4.8: a) k_Y^{lin} and b) k_Y^{lin}/Φ_{eq} for the group annealed at 20°C. In case of a first order dynamics, the distribution in figure a) should be flat while for a second order, the distribution b) should be flat.

first order model can be explained by the partial bias of some samples caused by a fixed bias voltage, independent of the irradiation fluence.

4.2.3 Test of Boron Reactivation Model

R. Wunstorf et al. [29] proposed a model for reverse annealing based on reactivation of boron. It is suggested that directly after irradiation boron does not act as an acceptor because it has been removed from the substitutional to an interstitial site. However,

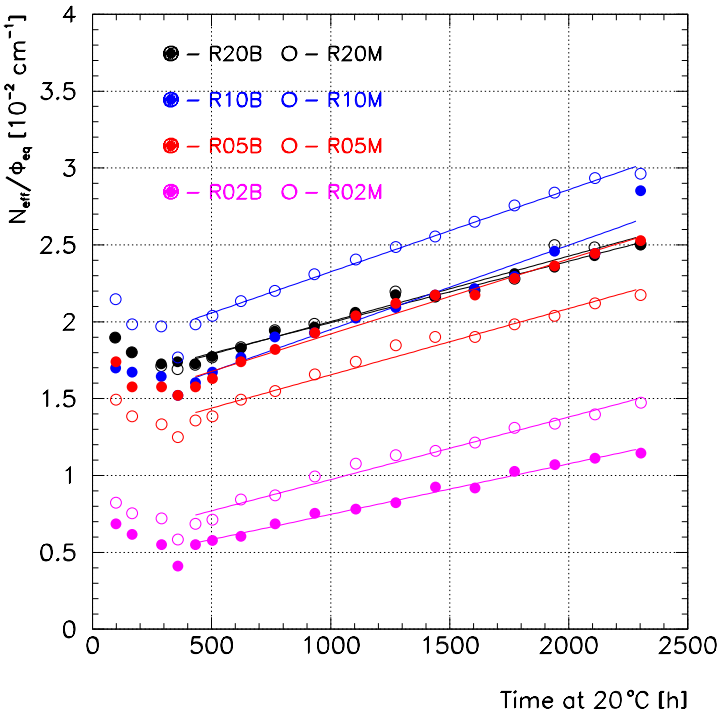

Figure 4.9: Development of N_{eff}/Φ_{eq} at the initial stage of reverse annealing for unbiased samples kept at 20°C.

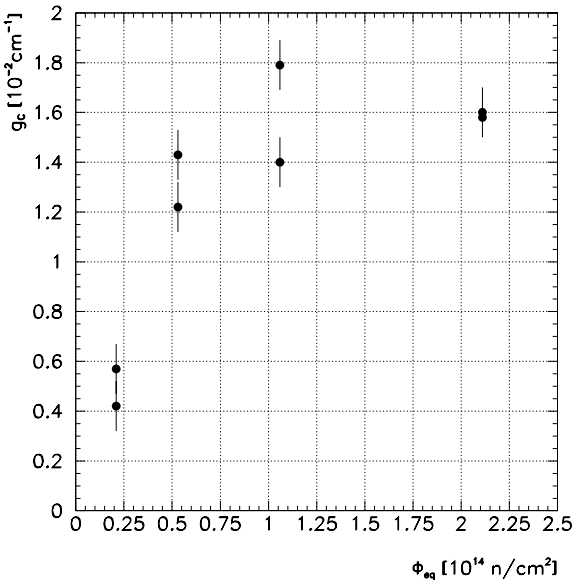

Figure 4.10: Fluence dependence of effective g_C for unbiased samples kept at at 20°C. 15% of systematic error on the dosimetry is not included in the error bars.

during long term annealing (reverse annealing) boron is reactivated through the reaction $B_i + V \rightarrow B_s$ where B_i indicates boron in an interstitial position (not electrically active) and B_s boron in a substitutional position (acceptor). The model thus predicts the acceptor increase during reverse annealing (g_Y) to be proportional to the concentration of boron in the original material, assuming sufficient availability of mobile vacancies. This model would have important implications for engineering of radiation hard materials, since the level of reverse annealing could be controlled by boron concentration in the initial material.

In the scope of this work an experimental test of the model has been performed. From the model follows, that the rise of N_{eff} during the reverse annealing should be removed in a subsequent irradiation. To check for such behaviour, an irradiated sample was reverse annealed to a late stage and irradiateda again. Development of full depletion voltage during the process was monitored and compared to the model prediction.

Sample I3 was irradiated to $4.4{\cdot}10^{13}$ n/cm^2 1 MeV neutron equivalent and completely reverse annealed (two months at 60°C). This was followed by a second irradiation to $4.1{\cdot}10^{13}$ n/cm^2 1 MeV neutron equivalent with repeated annealing at 60°C. Time development of the full depletion voltage for both irradiations is shown in figure 4.11. The first measurement data begin after almost all beneficial annealing has been completed.

If the above model were correct, the substitutional boron responsible for the reverse annealing after the first irradiation, should be removed during the second irradiation. From acceptor (boron) removal rate $c_A = 1.98 \cdot 10^{13}$cm^2 from the same article [29] and the fluence of the second irradiation ($4.1{\cdot}10^{13}$ n/cm^2) one can see that basically all reactivated boron should be removed by the second irradiation, cancelling the effect of reverse annealing after the first irradiation. This should reflect in a drop of full depletion voltage equal to the contribution of the reverse annealing (about 160 V). The total change of FDV during the irradiation should thus be equal to the difference between this drop (approx. 160 V) and the FDV raise induced by other irradiation induced defects (approx. 100 V after beneficial annealing). The value of the FDV at the plateau after second irradiation should equal the sum of defects constant in time introduced during both irradiations (approx. 240 V). Results in figure 4.11 however show this is not the case, so our results do not confirm the boron reactivation model.

It can also be seen from the comparison of the full (first irradiation) and open circles (second irradiation) in the first part of the figure, where the open circles were obtained by subtracting the FDV just before the second irradiation from the FDV after it. The comparison shows good agreement of defect generation and annealing from both irradiation steps.

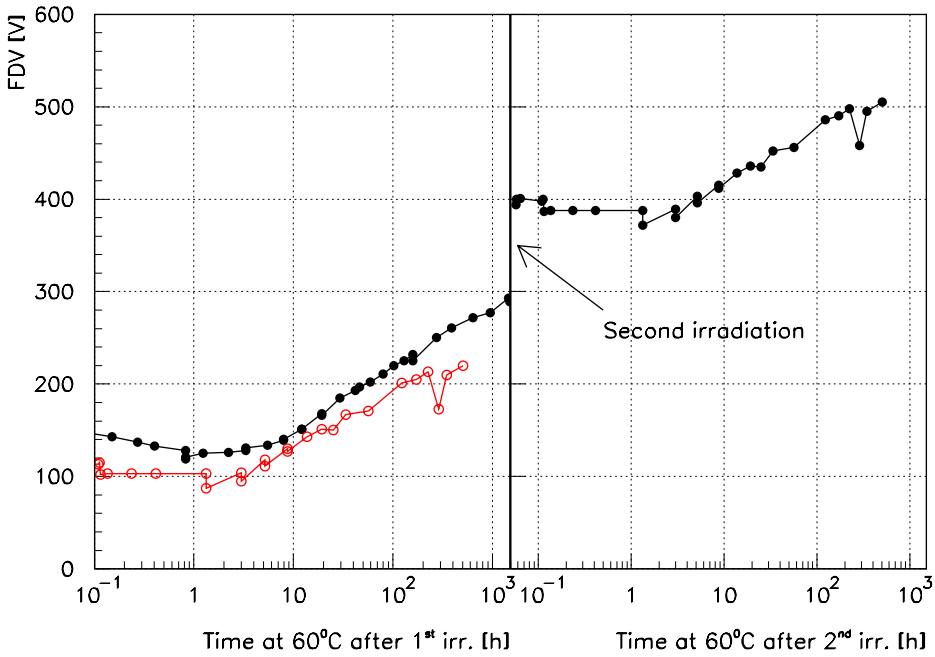

Figure 4.11: Time development of FDV for the diode I3 after the first and the second neutron irradiation ($4.4{\cdot}10^{13}$ n/cm^2 and $4.1{\cdot}10^{13}$ n/cm^2 1 MeV neutron equivalent, respectively). Open circles are used to compare the effect of the first and the second irradiation. They represent the change in full depletion voltage induced by the second irradiation (i.e. FDV after second irradiation reduced for the value of the FDV before the second irradiation).

4.3 Results on Annealing of MESA Samples

An effect of the production process to the radiation hardness was repored by various groups [32, 47, 48, 49, 50]. Thus a comparison of diodes produced by a planar and MESA process was performed in the scope of this work.

Two MESA processed 1×1 cm^2 diodes on Polovodice wafers were irradiated to $5 \cdot 10^{13}$ n/cm^2. The diodes are oxygen enriched due to the process [47]. Their irradiation conditions are listed in table 4.7. Sample R4 was irradiated under the same conditions as sample I3 and sample R3 same as sample D3 (compare with table 4.1).

Short term annealing was fitted with expression 4.3 and results of the fit are given in table 4.8. Comparison of the fast annealing of planar and mesa samples is shown in figure 4.12. Together with figure 4.14 it shows that in the initial stage of the annealing a 20-30% difference in the effective doping concentration develops, that persists also through latter annealing and reverse annealing (figure 4.13). This difference however can not be attributed to the initial difference in N_{eff} that reflected in about 100 V difference in FDV

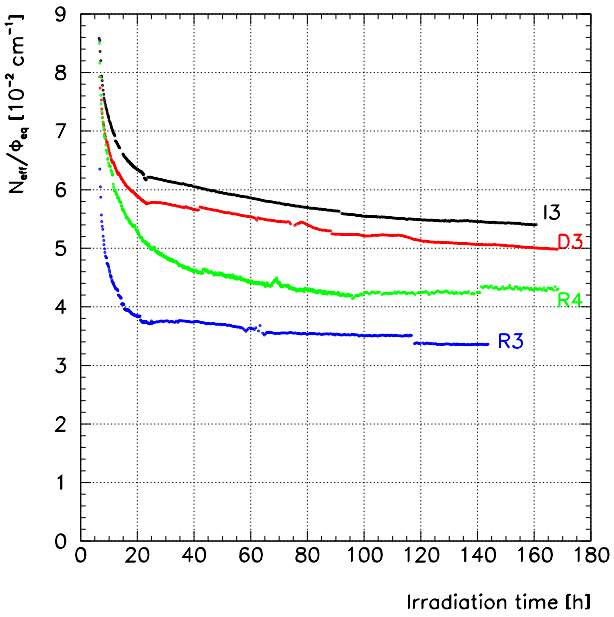

Figure 4.12: Comparison of short-term annealing of planar (I3, D3) and MESA (R4, R3) samples at 5°C (I3, R4) and 15°C (D3, R3).

Sample	process	No. of GR	V^0_{FD} [V]	T	ϕ_{eq} [n/cm^{2}s]	Φ_{eq} [n/cm^2]
R3	mesa	0	100	15°C	$1.8 \cdot 10^9$	$4.4 \cdot 10^{13}$
R4	mesa	0	110	5°C	$1.8 \cdot 10^9$	$4.2 \cdot 10^{13}$

Table 4.7: List of MESA processed diodes used in the study of fast annealing of N_{eff}. Processing type, number of guard rings, full depletion voltage before irradiation, irradiation/storage temperature, irradiation flux and fluence normalised to 1MeV neutrons are given for each sample. Thickness of samples was 300±5 μm.

Sample	T [°C]	g_0 [10^{-2}cm^{-1}]	g_1 [10^{-2}cm^{-1}]	τ_1 [h]	g_2 [10^{-2}cm^{-1}]	τ_2 [h]
R3	15°C	2.2	4.7	3.5	1.6	370
R4	5°C	4.2	5.1	2.8	2.2	21

Table 4.8: List of MESA samples with their irradiation temperatures and values of the fit parameters according to eq. 4.3.

before irradiation. As shown in figure 4.14, the difference in initial FDV disappeared during the irradiation as an effect of shallow donor removal.

Lower full depletion voltages for MESA processed samples as compared to planar ones have also been reported by G. Casse et al. [48]. They observed systematically better

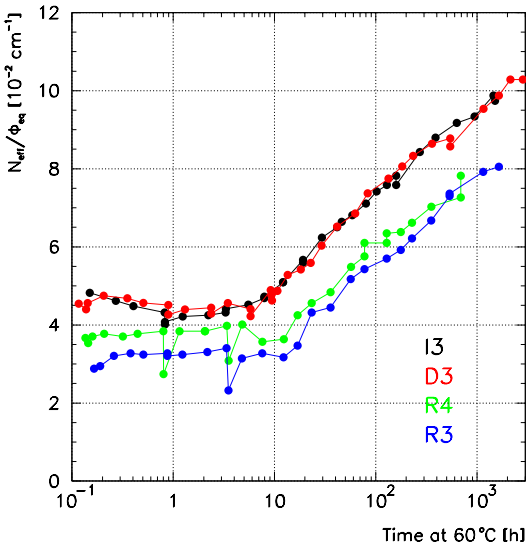

Figure 4.13: Comparison of N_{eff} development of planar (I3,D3) and MESA (R4,R3) samples after heating to 60°C.

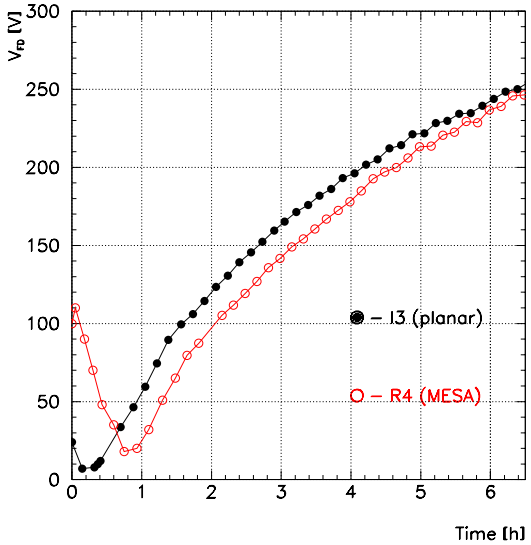

Figure 4.14: FDV comparison of diodes I3 (planar) and R4 (MESA) during the irradiation at 5°C.

radiation hardness of MESA samples as compared to planar ones. The difference shows as an about factor of two lower introduction rate of acceptor-like defects, lower introduction rate of reverse annealing defects and lower α damage constant. Those effects are however not induced by increased oxygen concentration only, since results on oxygenated planar samples (up to several 10^{17} cm^{-3}) show no decrease in FDV or α value as compared to non-oxygenated planar samples [48]. Agreement of FDV after irradiation for standard

and oxygenated materials was also reported by L. Beattie et al. [49], while B. Dezillie et al. [32] reports better radiation resistivity of MESA samples and M. Moll et al. [50] for Czochralski samples, both having an increased oxygen concentration (order of 10^{18} cm^{-3}).

4.4 Annealing of Reverse Current

As with N_{eff}, the time development of bulk generation current was studied in two parts: fast annealing at various temperatures during the first week after irradiation and long term annealing at 60°C to accelerate time development.

4.4.1 Fast Annealing

Sample	T [°C]	α'_0 [10^{-17}A/cm]	α_1 [10^{-17}A/cm]	τ_1^α [h]	α_2 [10^{-17}A/cm]	τ_2^α [h]
D3	15°C	4.6	2.0	4.2	1.9	55
D1	15°C	4.1	1.2	15.	1.4	180
B3	0°C	4.1	1.2	9.7	1.1	220
K0	5°C	5.4	14.	1.4	2.5	20
K3	5°C	5.1	7.4	2.2	1.9	38

Table 4.9: List of samples and irradiation temperatures with values of the fit parameters according to eq. 4.11. For easier comparison between samples and with other authors, values of the α parameter are normalised to 20°C.

Fast annealing of reverse current was studied on samples D3, D1, B3, K0 and K3. Their irradiation conditions are given in tables 4.1 and 4.3. The rest of the diodes had no guard ring structures, guard rings were not connectable or had some other problems that prevented reliable determination of the bulk current.

As with N_{eff}, short term annealing can be fitted with a constant part and two exponentials (eq. 2.63).

$$\alpha(t) = \alpha'_0 + \alpha_1 e^{-t/\tau_1^\alpha} + \alpha_2 e^{-t/\tau_2^\alpha} \tag{4.11}$$

and for irradiation times comparable to defect decay times τ_i, an ansatz equivalent to 4.3 was used. Measurement data together with fits according to eq. 4.11 are shown in figure 4.15 and the results of the fits are given in table 4.9.

Results from the present fits show no systematic behaviour with no clear temperature dependence while measured leakage currents agree within about 20%. Discrepancies

Sample	ϕ_{eq} [n/cm^{2}s]	Φ_{eq} [n/cm^2]	α_E [10^{-17}A/cm]	τ_E^α [h]	α_L [10^{-17}A/cm]	τ_L^α [years]
K3	$1.9 \cdot 10^9$	$1.03 \cdot 10^{14}$	1.4	0.7	0.32	2.
K0	$1.6 \cdot 10^{12}$	$1.04 \cdot 10^{14}$	1.1	1.8	0.26	6.
I3	$1.9 \cdot 10^9$	$4.4 \cdot 10^{13}$	1.3	1.8	0.26	14.
B3	$1.9 \cdot 10^9$	$4.4 \cdot 10^{13}$	1.4	1.3	0.29	8.
G3	$1.8 \cdot 10^9$	$8.3 \cdot 10^{12}$	1.2	1.6	0.28	9.
G2	$1.8 \cdot 10^{10}$	$8.7 \cdot 10^{12}$	1.2	1.9	0.24	12.
U3A	$1.8 \cdot 10^9$	$4.1 \cdot 10^{13}$	1.2	2.1	0.31	2.
U3B	$1.8 \cdot 10^9$	$4.1 \cdot 10^{13}$	1.2	2.1	0.32	3.

Table 4.10: List of diodes used to study long term annealing of bulk current. All samples are planar p^+-n-n^+ 1×1 cm^2 diodes, 300±5 μm thick with three guard rings. In the first part of the table are given irradiation flux and fluence normalised to 1 MeV neutrons. In the second part are values of the fit parameters according to ansatz 4.12. Values of the α parameters are normalised to 20°C to simplify comparison with other results. Time constants τ_E^α and τ_L^α are given for 60°C. Errors on α_E, τ_E^α and α_L are about 20% and on τ_L^α as large as 50%. The systematic error of the dosimetry is not included in the given errors.

between samples may be explained by contribution of surface current, high irradiation environment and long, partially unshielded, measurement cables. Measurements of the leakage current at the laboratory with shorter cables give the same value for all samples after a time equivalent to a few weeks at 20°C (see next section on long term annealing). For LHC experiments short term annealing is irrelevant anyway. It is however important to be aware of its extent when results from different sources are compared.

4.4.2 Long Term Annealing

Long term annealing of the bulk current has been studied on diodes K3, K0, I3, B3, G3, G2, U3A and U3B. Their irradiation conditions are given in table 4.10. To accelerate annealing, the samples were heated to 60°C for increasing time periods, intermited with C/V and I/V measurements at 5°C. As can be seen in figure 4.16, after almost three months at 60°C there was still no evidence of reaching a plateau.

A constant slope in log-lin plot at large heating times (over 10 h at 60°C) indicated that a logarithmic time dependence could parametrise the late stage of annealing. An effective ansatz

$$\alpha(t) = \alpha_E e^{-t/\tau_E^\alpha} - \alpha_L \ln(t/\tau_L^\alpha) \tag{4.12}$$

has thus been attempted. Agreement of measured data and ansatz 4.12 can be seen

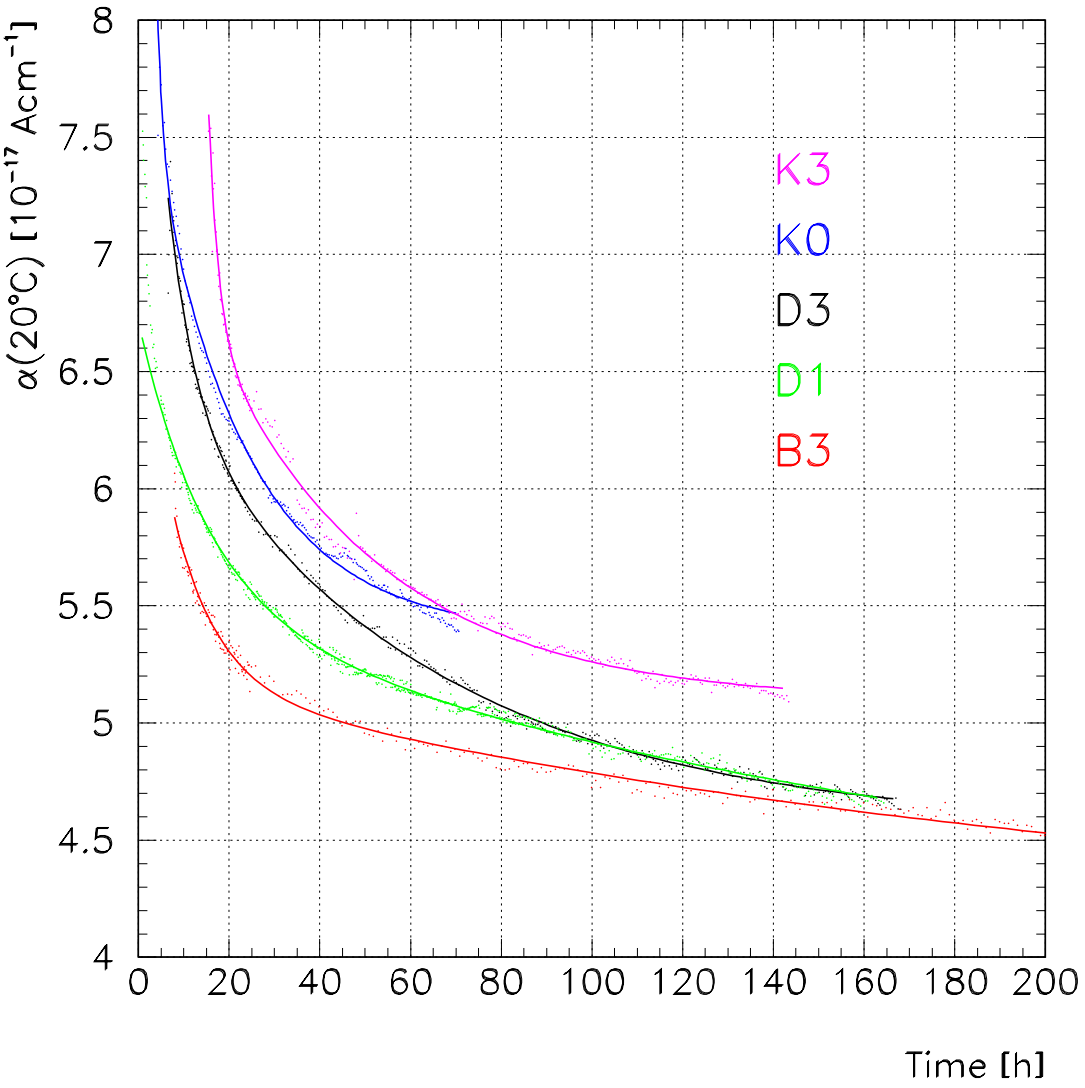

Figure 4.15: Short term development of the bulk current. Values of the α parameter are normalised to 20°C for easier comparison (eq. 2.39), though measurements were performed at various temperatures as given in the table 4.9. Fits according to eq. 4.11 are shown together with measurements. Note the suppressed zero.

in figure 4.16 and resulting fit parameters are given in table 4.10. It can be seen that agreement among the samples is reasonably good except for the time constant of the logarithmic part. Large discrepancies in τ_L should not be a surprise and reflect the fact that the logarithmic parametrisation lacks natural explanation. It is however a working ansatz for late annealing stages that can be used until the true nature of the process is unveiled.

The logarithmic part has a time constant equal to few years at 60°C and an introduction constant about a fourth of the exponential part. Though its temperature dependence is still to be determined, it can be expected to be significantly longer at lower temperatures. It is thus probably irrelevant for the LHC operation. It is however important to realise that the bulk current is decreasing steadily even after extremely long heating times without saturation on this time scale. For comparison of results from different sources it is thus important to state at what point in time the value of the α parameter was measured.

The logarithmic behaviour of the leakage current at late stages of annealing was also reported by [35]. Taking into account their somewhat different parametrisation

$$\alpha(t) = \alpha_1 e^{-t/\tau_1} + \alpha_0 - \beta \ln(t/\tau_0) \ , \tag{4.13}$$

here τ_0 is set to 1 min, one translates $\tau_L = \tau_0 \exp(\alpha_0/\beta)$, while the rest of parameters can be compared directly. Values reported by [35] are: $\alpha_1 = 1.01 \pm 0.38 \cdot 10^{-17}$ A/cm, $\tau_1 = 93 \pm 24$ min, $\alpha_0 = 5.03 \pm 0.09 \cdot 10^{-17}$ A/cm and $\beta = 3.34 \pm 0.26 \cdot 10^{-18}$ A/cm, giving $\tau_L \approx 6.6^{+45}_{-4.6}$ years. Comparison shows that results agree within errors except for α_L (β) where discrepancy is about twice the value of given errors.

Results presented in [35] can also be used to check the fluence measurement. Since only weak material dependence[36] was observed, values of the α parameter at a given annealing stage can be compared to cross check the dosimetry from different irradiation sources. $\alpha(20°\text{C})$ value after 2880 minutes at 60°C as obtained with the TRIGA reactor equals $2.0 \pm 0.3 \cdot 10^{-17}$. Good agreement with the expectation from [35] of about $2.2 \cdot 10^{-17}$ confirms the absolute scale of the dosimetry used in this work.

4.5 Conclusion

A systematic study of the time development of N_{eff} and reverse current has been performed under controlled conditions. Results on short-term annealing show that both N_{eff} and reverse bulk-current are subject to significant fast annealing in the first day after irradiation. Although this annealing has no influence on the operation of detectors in LHC experiments, it has however to be taken into account when comparing results of irradiation damage studies from different sources.

An extensive study of reverse annealing was performed to unveil the nature of the responsible process. While from most of the samples no conclusive evidence could be obtained due to bias-effect interference (see chapter 6), a dedicated set of 8 unbiased

[36] Discrepancy of about 6% (1 σ) in α among different materials has been observed after 80 minutes at 60°C [35].

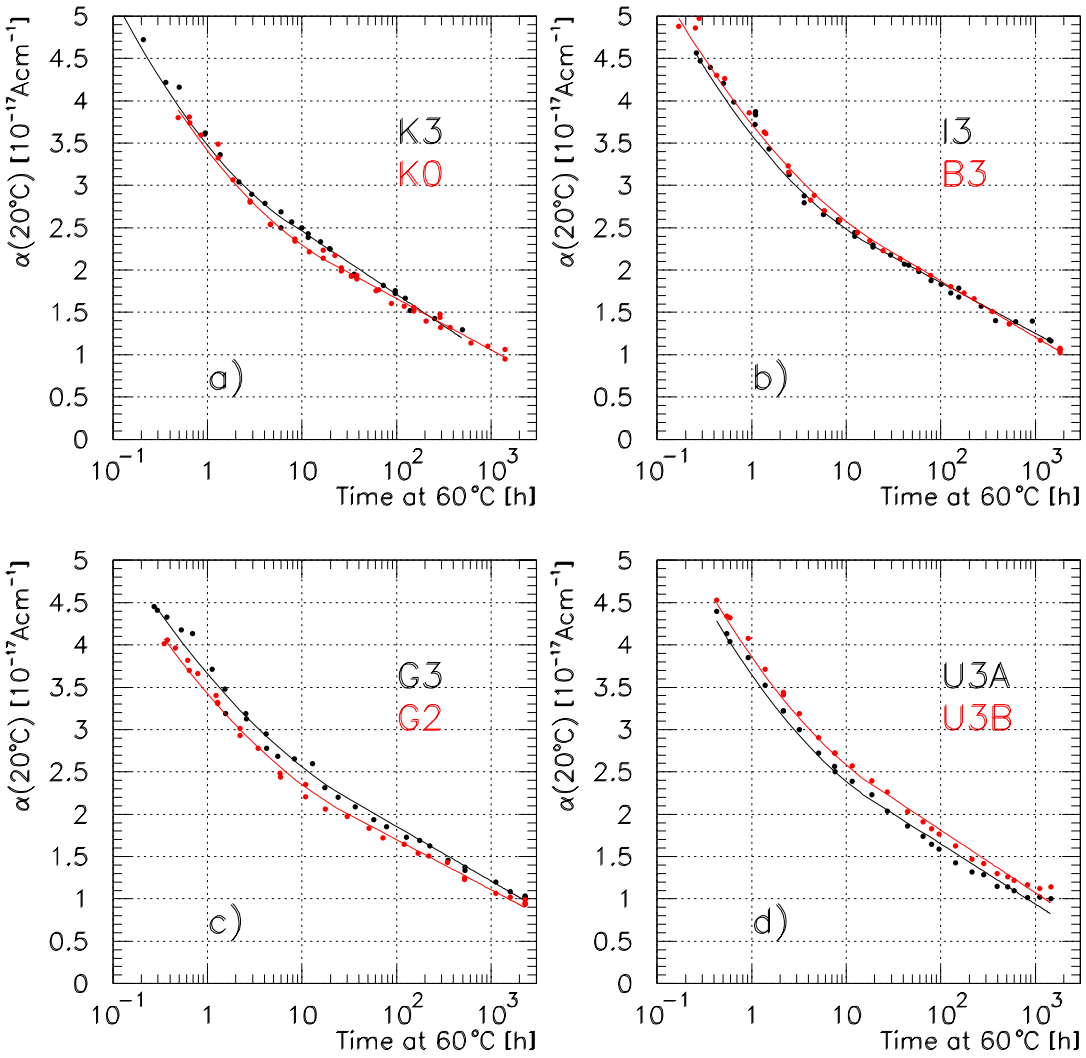

Figure 4.16: Long term development of the bulk current. Values of the α parameter are normalised to 20°C for easier comparison with other sources, though measurements were performed at 5°C. Fits according to eq. 4.12 are shown together with measurements.

samples annealed at 20°C is clearly showing a linear dependence of initial slope of N_{eff} reverse annealing on irradiation fluence. Thus at least during the initial stage of the reverse annealing, relevant for the LHC operation, the reaction dynamics is described by a first order process. Further studies are however necessary to determine the influence of reverse bias on the reverse annealing constants.

Reverse leakage current shows similar short-term annealing behaviour to that of

N_{eff}. In agreement with results from previous sources [46, 21, 19, 14, 18] no reverse annealing was observed. Long term annealing at 60°C however does not lead to the expected saturation of reverse current, but shows continuous annealing with an effective logarithmic time dependence. The true nature of this effect is at the present not completely clear.

5

Dose Rate Dependence

5.1 Motivation

Irradiation of silicon detectors in the environment of future detectors will be a slow process, taking many years to accumulate the predicted fluence of the order of 10^{14} n/cm^2 1 MeV neutrons equivalent. For obvious reasons it is unpractical, if not impossible, to perform studies of irradiation damage effects with fluxes that low. Most often samples are irradiated to those fluences in a few hours or days. It is thus important to check for a possible flux effect. Even more so because results on ion implantation with Br, Si and C are showing considerable decrease in trap generation rates for fluxes above a treshold of about 10^7 cm^{-2}s^{-1}, 10^8 cm^{-2}s^{-1} and few times 10^8 cm^{-2}s^{-1}, respectively [52]. This can be explained by clusters overlapping at high fluxes, enhancing prompt vacancy-interstitial silicon recombination, thus reducing radiation induced damage.

The reactor where the present irradiations were performed can cover a wide range of fluxes. The maximal flux is determined by a fluence of about 10^{14} n/cm^2 that can be obtained in an about 20 ms long pulse, giving a flux of about $5{\cdot}10^{15}$ n/cm^{2}s. The lower flux was limited by practical reasons (about 150 h for 10^{14} n/cm^2) to about $2{\cdot}10^8$ n/cm^{2}s. Thus, a range of more than seven orders of magnitude in flux can be investigated.

A set of 7 samples was used to study the flux influence. They were all irradiated to about 10^{14} n/cm^2 with neutron fluxes covering the above mentioned range. All samples were 1×1 cm^2 p^+-n-n^+ planar Micron diodes. Except for samples SA1 and SA2 that had 1 and 2 guard rings respectively, all diodes had 3 guard rings. Details about irradiation and storage are listed in table 5.1. For samples K0, K1 and K3, about a week after irradiation, the time development was accelerated by heating to 60°C. In case of SA and P0 diodes, heating started 8 and 4 months after the irradiation. In the meanwhile they

Sample	V^0_{FD} [V]	T	ϕ_{eq} [n/cm^{2}s]	Φ_{eq} [n/cm^2]	bias [V]
SA1	12	-10°C$^+$	$2.2 \cdot 10^8$	$1.3 \cdot 10^{14}$	0
SA2	12	-10°C$^+$	$2.2 \cdot 10^8$	$1.3 \cdot 10^{14}$	150*
K3	6	5°C	$1.9 \cdot 10^9$	$1. \cdot 10^{14}$	200
K1	32	5°C	$3.7 \cdot 10^{11}$	$1. \cdot 10^{14}$	200
K0	32	5°C	$1.6 \cdot 10^{12}$	$1. \cdot 10^{14}$	200
P0A	8	-5°C$^+$	$\approx 5 \cdot 10^{15}$	$1.1 \cdot 10^{14}$	0**
P0B	8	-5°C$^+$	$\approx 5 \cdot 10^{15}$	$1.1 \cdot 10^{14}$	200***

Table 5.1: List of diodes used in the study of dose rate influence. Full depletion voltage before irradiation, irradiation/storage temperature, irradiation flux and fluence normalised to 1 MeV neutrons and bias voltage are given for each sample. Thickness of samples was 300±5 μm.
$^+$ Sample was heated to 20°C several times for a few hour periods to repair broken bias/measurement lines.
* Biasing of SA2 was lost several times during the first 6 months due to lost contact. When heating to 60°C started, 200 V bias was used.
** Sample P0A was biased to 350 V for about first 30 min, then the contact was lost.
*** Sample P0B was not biased for the first few days.

were kept at -10°C and -5°C, respectively, as indicated in table 5.1[37].

Development of N_{eff} and reverse current of samples was compared to observe possible differences due to a dose rate effect. Results of the study are presented in the following sections.

5.2 Results on N_{eff}

Time development of N_{eff} for samples listed in table 5.1 after start of heating to 60°C is shown in figure 5.1. The second order ansatz 4.7 was used in the fit. The second order parametrisation was chosen because it describes the late stage of reverse annealing better than the first order one. The fluence dependence of the time constant, that is the main difference between the two models, was not important in this case, because all samples, used fo the study of the flux effect, were irradiated to simmilar fluences (table 5.1). Results of the fits are given in table 5.2 and compared in figures 5.2 to 5.4.

Neither plots of N_{eff} time development during reverse annealing nor fit results show any systematic variations that could be correlated with flux. Discrepancies between different samples can be attributed to different biasing conditions (see chapter 6) and

[37] In this time samples were not yet fully annealed and thus storage had negligible influence on study of reverse annealing.

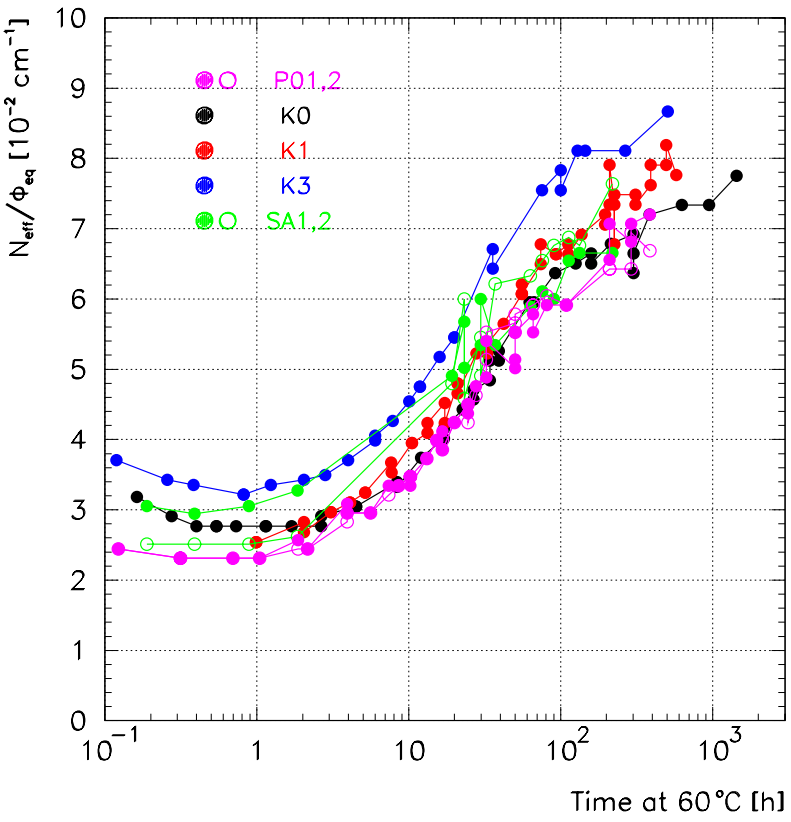

Figure 5.1: Time development of N_{eff} at 60°C for detectors, irradiated with different neutron fluxes.

Sample	g_C [10^{-2}cm^{-1}]	g_Y [10^{-2}cm^{-1}]	k_2^Y(60°C) [10^{-18}cm^{3}s^{-1}]
SA1	2.9	4.0	3.1
SA2	2.4	5.5	1.5
K3	3.0	6.0	1.5
K1	2.4	5.6	1.7
K0	2.6	4.8	1.5
P0A	2.3	5.1	1.5
P0B	2.3	4.9	1.6

Table 5.2: Results of the second order fit. Generation rates for defects constant in time (g_C) and those responsible for reverse annealing (g_Y) are given together with the reverse annealing constant k_2^Y. Errors on k_2^Y are about 5%. Errors on k_2^Y and g_Y are larger for SA1 and SA2 samples due to the low number of measurement points on the slope and breakdown below FDV at late stage of reverse annealing.

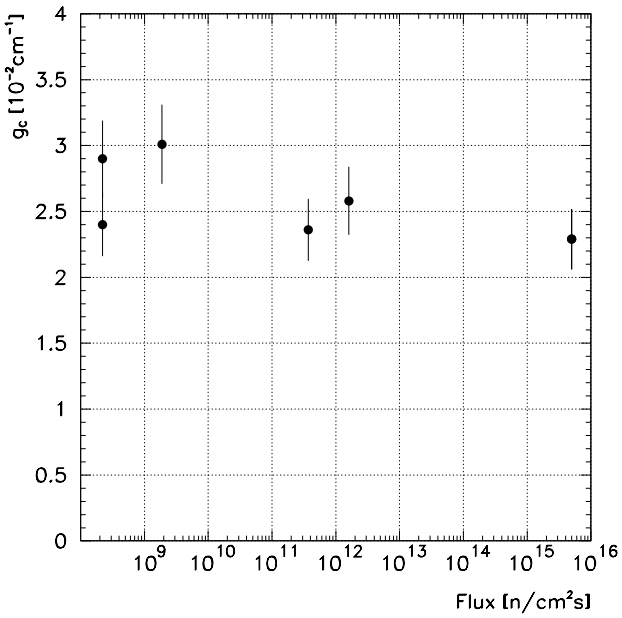

Figure 5.2: Introduction rate of stable defects g_C versus irradiation flux.

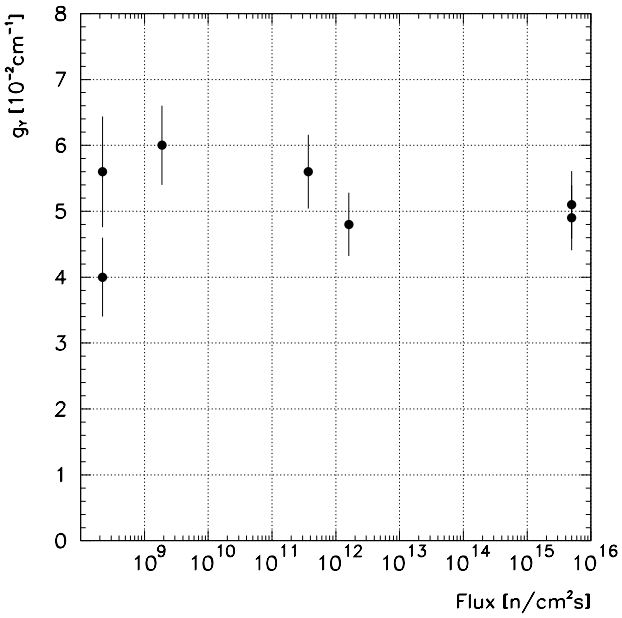

Figure 5.3: Introduction rate of defects, activated during the reverse annealing (g_Y), versus irradiation flux.

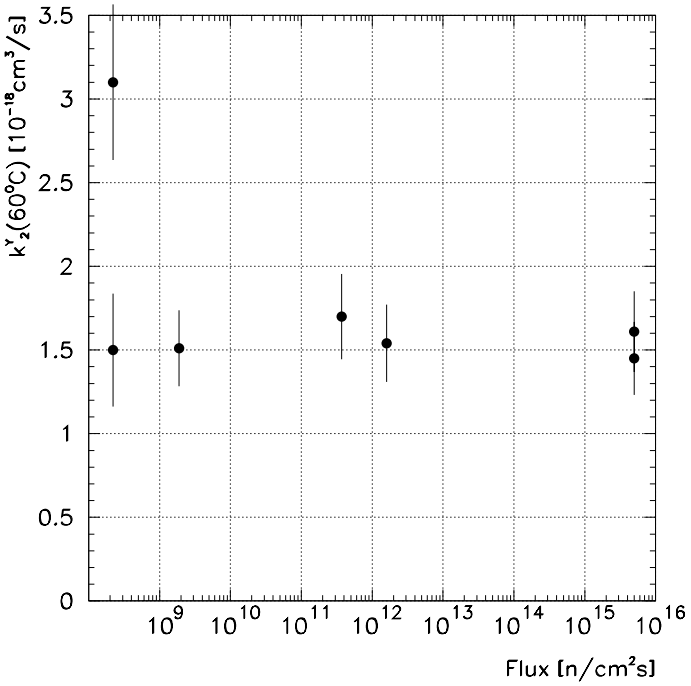

Figure 5.4: Reverse annealing constant k_2^Y versus irradiation flux.

errors on dosimetry. SA and P0 samples also have a larger error on FDV at late stages of reverse annealing. Its source is extrapolation of C^{-2} versus V curve to the plateau value. This was necessary because of breakdown below full depletion voltage.

5.3 Results on Reverse Current

Study of the leakage current could unfortunately not be performed on the full range of dose rates. The reason were problems with guard ring connections that occurred with samples SA and P0. With guard rings not connected it was not possible to separate the bulk generation current from surface current generated on the edge. Since its contribution can be much larger than the bulk generation current (see fig. 3.13), those samples are useless for comparisons of the reverse current. Thus only samples K0, K1 and K3, irradiated with neutron fluxes of $2.3 \cdot 10^{12}$ n/cm^{2}s, $4.2 \cdot 10^{11}$ n/cm^{2}s and $2.1 \cdot 10^9$ n/cm^{2}s are shown in figure 5.5. The reverse currents were fitted according to eq. 4.12 and results are given in table 5.3. Some measured points with bad guard ring connection for sample K1 on that figure indicate the variability of the surface current contribution.

Though one can notice some difference among the samples it is attributed to the measurement error. It is also not correlated with the irradiation flux and could thus

hardly be a flux effect.

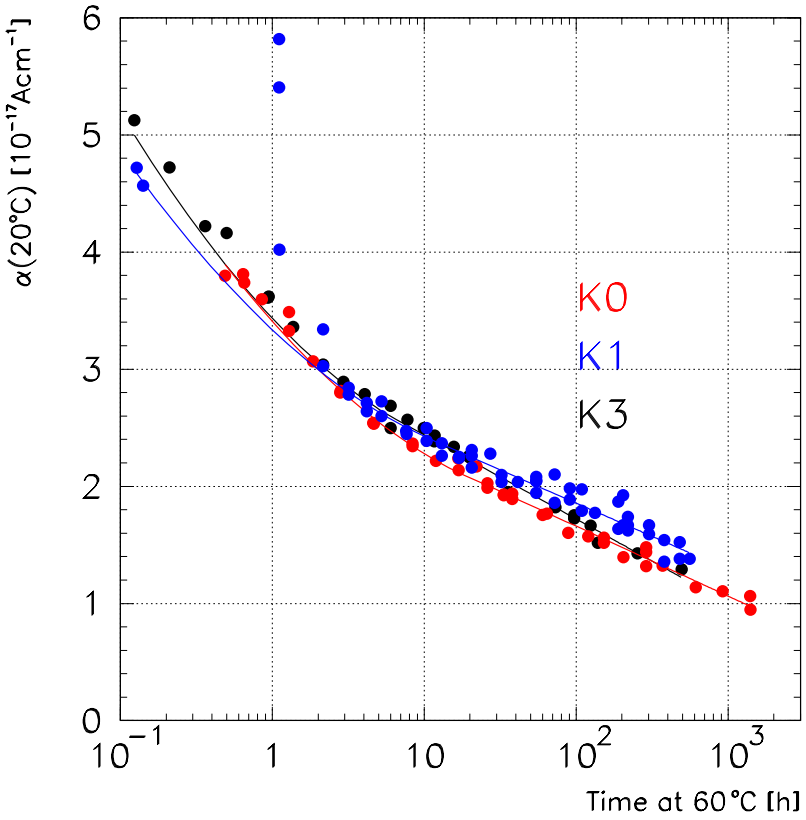

Figure 5.5: Time development of reverse bulk current at 60°C for diodes K0, K1 and K3. The bulk current generation constant α (eq. 2.50) normalised to 20°C is used to compare different samples.

Sample	α_E [10^{-17}Acm^{-1}]	τ_E^α [h]	α_L [10^{-17}Acm^{-1}]	τ_L^α [10^4 h]
K3	1.4	0.7	0.32	2.
K0	1.1	1.8	0.26	6.0

Table 5.3: Results of annealing of bulk current. Errors on α_E, τ_E^α and α_L are about 20% and on τ_L^α around 50%. For sample K1 the fit does not converge properly. The systematic error of dosimetry is not included in the given errors.

5.4 Conclusions

Influence of the flux on radiation induced bulk damage has been studied for 1 MeV neutron equivalent fluxes from $2{\cdot}10^8$ n/cm^{2}s to about $5 \cdot 10^{15}$ n/cm^{2}s. No systematic effect that could be correlated to flux has been observed in this range neither in the effective doping concentration nor in the reverse bulk current. Results from [52] show that a change occurs at fluxes around $10^7 - 10^9$ cm^{-2}s^{-1} for irradiations with heavier elements (Br, Si and C) and that this threshold is increasing with decreasing mass number. For neutrons one would therefore expect a higher threshold, but even up to $5 \cdot 10^{15}$ n/cm^{2}s no effect was observed. It thus seems safe to extrapolate the damage induced by available neutron sources to the expected flux at LHC of about 10^6 n/cm^{2}s.

6

Influence of Bias Voltage

It was a general belief that bias voltage does not affect creation or time development of radiation induced defects in silicon. It also seemed consistent with the first irradiations made in the scope of this work (diodes SA and P0). As we understand so far the reasons that the bias effect was not seen were in only partially biasing the samples and frequent time intervals with no bias at all. This must have reduced the effect of the bias sufficiently to attribute the remaining difference between biased and unbiased samples to other parameters (dosimetry, measurement errors etc). Thus it was rather late before this effect was observerd and systematically studied. This reflects in the results of previous chapters, where most of the samples were only partially biased. Parameters obtained by those measurements are thus a combination of those for biased and those for unbiased samples. Another unfortunate consequence of the late discovery is the fact that time development of the decreasing of the difference in N_{eff} after switching off the bias has not been studied yet to the extent it deserves.

6.1 Influence on N_{eff}

6.1.1 Time Development of Unbiased Samples

To study reverse annealing of unbiased samples a pair of float-zone Micron planar processed 1×1 cm^2 diodes, with initial FDV of about 18 V, were irradiated and stored without bias. Diodes were irradiated in parallel, to a fluence of $4.1 \cdot 10^{13}$ n/cm^2 1 MeV neutron equivalent (irradiation flux $1.8 \cdot 10^9$ n/cm^{2}s). After 1 day at room temperature, time development was accelerated by heating to 60°C. Time development together with a first order (eq. 2.57) and a second order (eq. 2.61) fit for both diodes is shown in fig. 6.1. Results of the fits are given in table 6.1.

Comparison of the fits with measured data (fig. 6.1) shows better agreemet for the

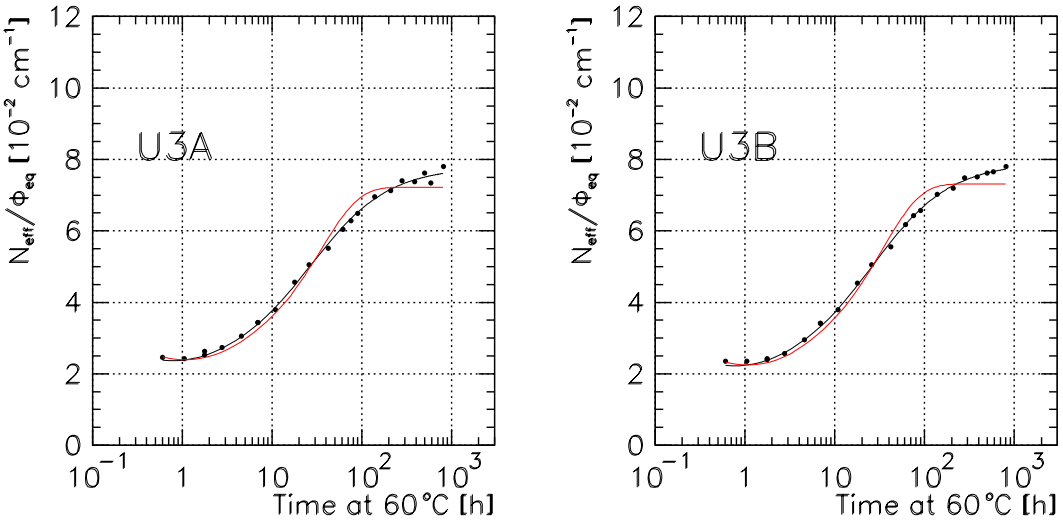

Figure 6.1: First order (red line) and second order (black line) fits for diodes U3A and U3B (unbiased during irradiation and storage). N_{eff}/Φ_{eq} versus heating time at 60°C is displayed.

Sample	g_C [10^{-2}/cm]		g_Y [10^{-2}/cm]		k^Y(60°C)		χ^2/ndf	k_Y^{lin}(60°C)
					[10^{-6}/s]	[10^{-18}cm^3/s]	1^{st} / 2^{nd}	[10^{-7}/cm^{2}s]
	1^{st} o.	2^{nd} o.	1^{st} o.	2^{nd} o.	1^{st} or.	2^{nd} or.	order	
U3A	2.4	2.3	4.8	5.5	8.0	4.6	2.1 / 0.4	3.2
U3B	2.2	2.1	5.0	5.8	8.4	4.5	2.3 / 0.5	3.4

Table 6.1: Fit parameters for reverse annealing of diodes U3A and U3B using first and second order models. Generation rates for defects constant in time (g_C) and for those responsible for reverse annealing (g_Y) are given together with reverse annealing constants k_1^Y and k_2^Y. χ^2/ndf is given for both fits to compare agreement of both models with measured results. Reverse annealing constant k_Y^{lin} was obtained by the linear fit of the ansatz 4.10 during the initial stage of reverse annealing.

second order expression. This is also confirmed by about 5 times lower χ^2/ndf for the second order ansatz (table 6.1). Since complete volume of both samples was undepleted during the treatment, better agreement of the second order expression can not be attributed to partial bias. This indicates that another process becomes significant at a later stage of reverse annealing, with properties still to be determined. They are however not important for the LHC operation, where only the initial stage of reverse annealing will take place.

Slope of the linear fit at the initial stage of reverse annealing can be compared with

the slope for unbiased diodes, annealed at 20°C (table 4.6). Average values of k_Y^{lin} for both sets are

$$k_Y^{lin}(20°\mathrm{C}) = (12.4 \pm 2) \cdot 10^{-10}/\mathrm{cms} \tag{6.1}$$

$$k_Y^{lin}(60°\mathrm{C}) = (3.3 \pm 0.15) \cdot 10^{-7}/\mathrm{cms}\ . \tag{6.2}$$

Comparison shows about 270 times faster reverse annealing at 60°C compared to 20°C, consistent with an activation energy of about 1.17 ± 0.04 eV (eq. 4.5). While it is far from 1.3 ± 0.04 eV [13, 14, 15], giving factor of about 500, it agrees well with 1.18 eV, reported by Z. Li et al. [53]

6.1.2 Comparison of Biased and Unbiased Samples

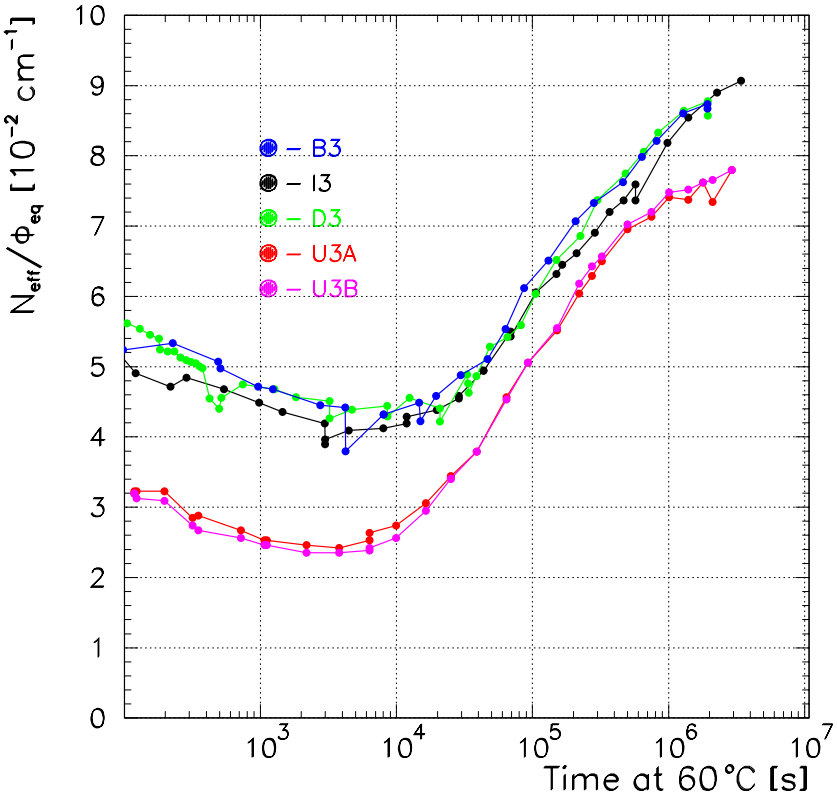

Figure 6.2: Comparison time development of N_{eff} for biased (B3, D3, I3) and unbiased (U3A, U3B) samples. All samples were kept under same conditions except for bias voltage.

Most suitable for comparison with samples U3 are diodes I3, D3 and B3 (fig. 6.2). They were irradiated to the same fluence with the same neutron flux and treated identically except for the bias voltage and storage temperature before the warm-up treatment (table. 4.3). Comparison of plateaus after beneficial annealing shows for a factor about 2 lower values for unbiased samples. Reverse annealing parameters (fig. 4.2, 4.3 and table 4.4) show that the introduction rate of the defects, responsible for reverse annealing (g_Y), is comparable for both biasing conditions. The reaction constants k^Y and k_Y^{lin} are however about twice larger for unbiased samples. This could be a consequence of slow annealing of bias dependent difference. It could also be explained if reverse annealing was caused by reaction of charged defects and consequently slowed down in electric field. Available data however do not allow for unambiguous distinction between these two possibilities. The difference could not be explained by partial bias, since it develops already at an early stage of reverse annealing, when biasing voltage of 200 V was still above FDV of the biased samples. This difference in reverse annealing of biased and unbiased samples also contributes to the error in determination of the reverse annealing reaction constants of the partially biased samples as discussed in section 4.2.

Sample	producer	V_{FD}^0 [V]	T [°C]	ϕ_{eq} [n/cm^{2}s]	Φ_{eq} [10^{14} n/cm^2]	V_{bias} [V]
S3A	Micron	32.	15 $^+$	$1.9{\cdot}10^9$	0.45	200/0 *
S3B	Micron	34.	15 $^+$	$1.9{\cdot}10^9$	0.45	0/200 **
D2A	Micron	17.	15	$1.8{\cdot}10^{10}$	0.42	300
D2B	Micron	17.	15	$1.8{\cdot}10^{10}$	0.42	0
UO6B	Sintef	35.	20	$1.8{\cdot}10^{11}$	1.7	1000/600†
UO6S	Sintef	35.	20	$1.8{\cdot}10^{11}$	1.7	0
BA2B	Sintef	44.	15	$2.1{\cdot}10^{11}$ #	1.0 #	500
BA2S	Sintef	44.	15	$2.1{\cdot}10^{11}$ #	1.0 #	0
BA4B	Sintef	40.	20	$2.1{\cdot}10^{11}$ #	1.0 #	600
BA4S	Sintef	36.	20	$2.1{\cdot}10^{11}$ #	1.0 #	0

Table 6.2: List of diodes used to study the effect of bias voltage on defect development. Thickness of samples was 300±5 μm.

$^+$) Diodes S3 were kept at bout 27°C after transfer to the laboratory to accelerate annealing. When annealed, they were moved to 20° C to study annealing of the difference in N_{eff}.

*) Diode S3A was biased during and unbiased after the irradiation.

**) Diode S3B was unbiased during and biased after the irradiation.

† Diode UO6A was biased to 1000V at the reactor and to 600V at the laboratory. Bias voltage could be reduced due to annealing of FDV.

#) Due to frequent changes in the reactor core at the time of irradiation, the neutron spectrum was not well known. This induced an error on dosimetry, larger than the usual 15%.

For further studies we wished to minimise the influence of any uncontrolled parameters and to avoid errors from fluence measurements. Thus diodes were irradiated and monitored in pairs, with a biased and unbiased diode in each pair. Both diodes were taken from the same wafer to minimise the risk of difference caused by material. Five pairs as listed in table 6.2 were studied this way. Samples S3 and D2 were Micron float-zone p^+-n-n^+ diodes with 3 guard rings and an active area of 1×1 cm^2. Samples UO6, BA2 and BA4 were p^+-n-n^+ planar diodes processed by Sintef. They had a multiple guard-ring structure that was not connectable and thus floating. Samples marked with last letter B had 6×6 mm^2 active area and those marked S 3×3 mm^2 active area. All diodes were 300 μm thick.

Diodes D2A and S3A were used to determine the origin of the difference between biased and unbiased samples. It could originate in bias dependent creation rates or be a consequence of defect reactions being affected by the electric field. To distinguish these two scenaria, D2A was biased during and after irradiation, while diode S3A was biased during and unbiased after irradiation. Time development of N_{eff} at 15° during the first few days after irradiation is shown in figure 6.3. The diode unbiased after irradiation exhibits a lower N_{eff} than the biased one[38].

At later stages of annealing we can also compare those two samples with their partners, unbiased during irradiation (figure 6.4). While diode D2B was unbiased both during and after the irradiation, diode S3B was biased with 200 V after the irradiation. Comparison of N_{eff} for all four samples at the plateau shows that both samples, unbiased after the irradiation (S3A and D2B), annealed to an equal N_{eff}. It also agrees well with the minimal N_{eff} of the U3 samples (fig. 6.2). Plateau of the D2A sample is about two times higher and agrees well with biased samples B3, I3 and D3 (fig. 6.2). The plateau value of the sample S3B is in-between. This can be explained by fast annealing that took place during the irradiation when this sample was unbiased.

This behaviour could be explained by assuming that the presence of electric field does not affect the defect introduction rates, while it influences their time development. This could be easily understood if defects are charged and reactions responsible for time development are diffusion limited. Then the electric field would influence defect movement through the crystal, thus affecting reaction rates responsible for annealing. A reaction of the type

$$A + B \rightarrow C \tag{6.3}$$

where A is an active defect, B a charged, mobile defect and C an inactive defect could

[38]The difference at the end of irradiation can be explained by annealing during irradiation, since the irradiation time was 39 minutes for diode D2A and 6.5 hours for S3A. This difference however becomes irrelevant after a few days of annealing.

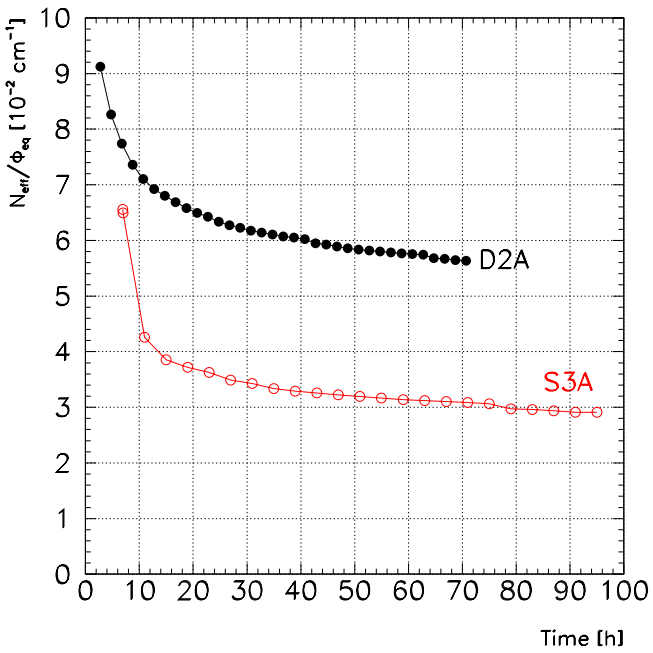

Figure 6.3: Comparison time development of N_{eff} for a sample biased (D2A) and unbiased (S3A) after irradiation. Both samples were biased during irradiation and kept at 15°C.

present a viable model.

6.1.3 Study of a Partially Depleted Diode

Diode I3 was irradiated to 5×10^{13} n/cm^2 and annealed at 60°C for two months. After that it was irradiated to 4.6×10^{13} n/cm^2, followed by three weeks at 60°C. During all this time it was biased to 200 V. This means that at least after the second irradiation the sample was only partially biased during all of the annealing stage, causing part of it to anneal depleted and part undepleted. $1/C^2$ vs. V plot after this procedure is shown in figure 6.5, together with the distribution of N_{eff} through the sample width as determined from the C/V measurement according to equations 2.44 and 2.45. At 200 V a kink in the slope of the $1/C^2$ vs. V curve can be clearly seen. Since the sample was kept at 200 V during all the time, the position of the kink agrees well with the border between the depleted and non-depleted regions. The corresponding difference in N_{eff} is about a factor of two (figure 6.5b).

To confirm the correlation between the difference in N_{eff} and biasing conditions, the bias was switched off. About one third of the difference annealed out in the first day at 20°C (fig. 6.6 red points) but no additional change developed in the following two weeks. To accelerate the processes, the sample was heated to 60°C. Measurements after

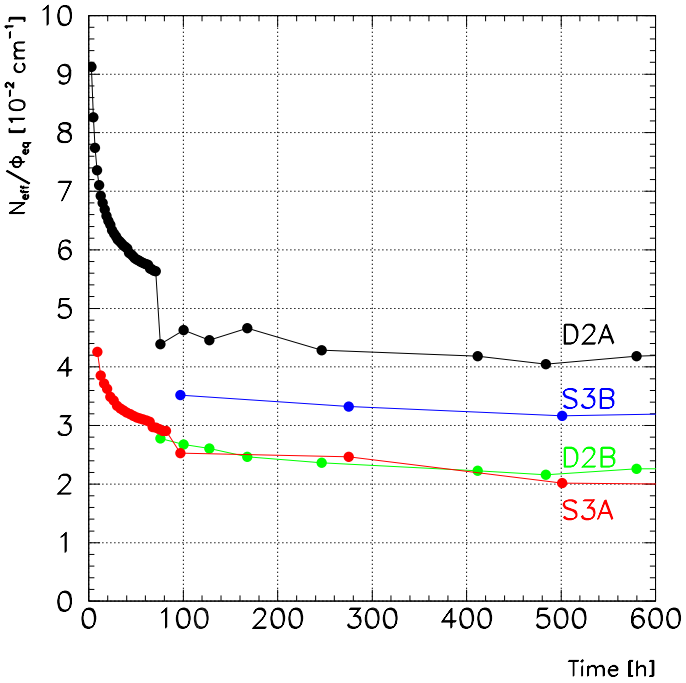

Figure 6.4: Comparison of plateaus of N_{eff}/Φ_{eq} for a sample biased during and after irradiation (D2A), biased during (6.5 h) and unbiased after the irradiation (S3A), unbiased during (6.5 h) and biased after irradiation (S3B) and sample unbiased during and after irradiation (D2B).

7 h (green points), one day (blue points) and 4.5 days (magenta points) are also shown in figure 6.6. One can see that N_{eff} concentration in the region that used to be depleted is slowly decreasing towards the value of the non-depleted region where no significant change in N_{eff} is observed. This shows that defects, whose annealing is inhibited by the electric field, remain in silicon also during long term annealing. They start annealing out, however, upon switching off the bias.

After prolonged heat treatments, in the first few days at 5°C a slight decrease (about 5%) in FDV as determined from C/V measurement has been noticed. To avoid the influence of this effect, C/V measurements at the late stage of reverse annealing were taken about a week after transfer to 5°C, when a stable state was reached.

6.2 Annealing of the Difference in N_{eff}

As shown in section 6.1.2 the minimal value of N_{eff} as reached under bias is about twice larger from the one with no bias applied. In this section results on annealing of this difference are presented.

Samples D2, UO6, BA2 and BA4 were used to determine time constants of annealing

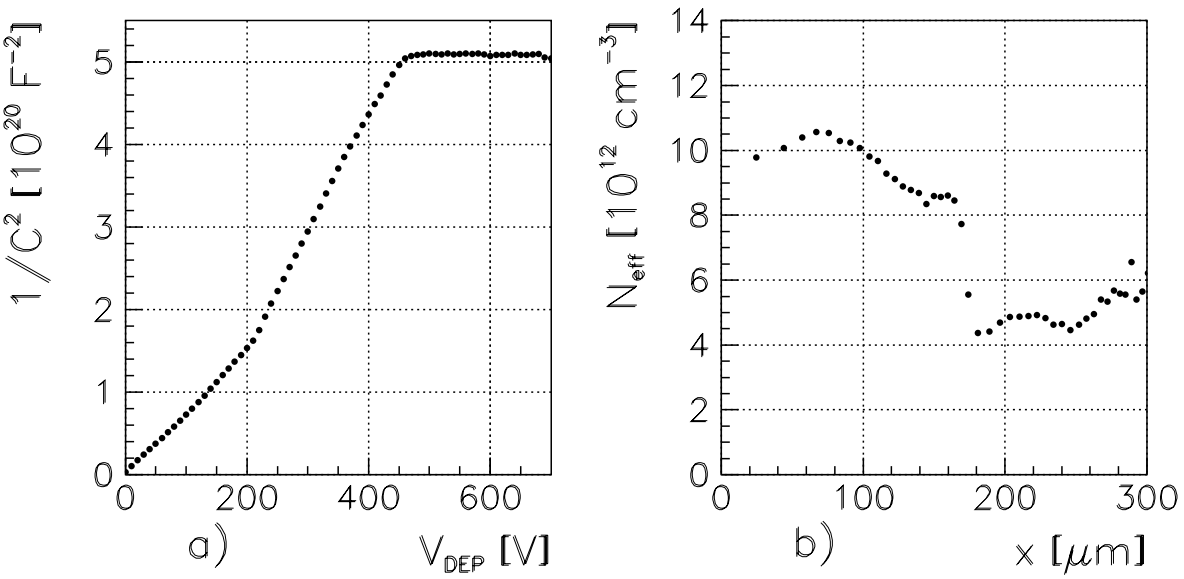

Figure 6.5: a) $1/C^2$ vs. V plot and b) N_{eff} distribution for the sample I3 after the end of heat treatment. Two regions with different N_{eff} , corresponding to different biasing conditions,, can be clearly seen.

of the difference between biased and unbiased samples. In all four pairs biased diodes were kept under bias until the end of beneficial annealing i.e. until the plateau in N_{eff} was reached. During this time they had been kept at 15 or 20°C as indicated in table 6.2. After that they were stored at -7°C (samples BA2), 5°C (samples BA4) and 20°C (samples UO6 and D2). Storage temperatures were chosen to determine time constants of the decrease of bias induced diffrence at the operation (-7°C) and maintenance (≈20°C) temperatures corresponding to the ATLAS operation scenario [6]. The measurement at 5°C provides an additional point for determination of the activation energy. Bias voltage was switched off on the biased samples, except for the diode D2A, where 350V of reverse bias has been replaced by approximately 10V of forward bias[39]. Time development of the difference between the formerly biased and unbiased samples was observed. To reduce the error in determination of the difference, values from a linear fit to the initial stage of reverse annealing were used for the time development of unbiased samples. In figures 6.7a to 6.9a time development of N_{eff} for each pair from the end of irradiation is shown. Figures 6.7b to 6.9b show time development of the difference normalised to the value before the bias was switched off.

One can see that in samples, where the bias voltage was switched off, the difference

[39] 1 mA forward current limit was used.

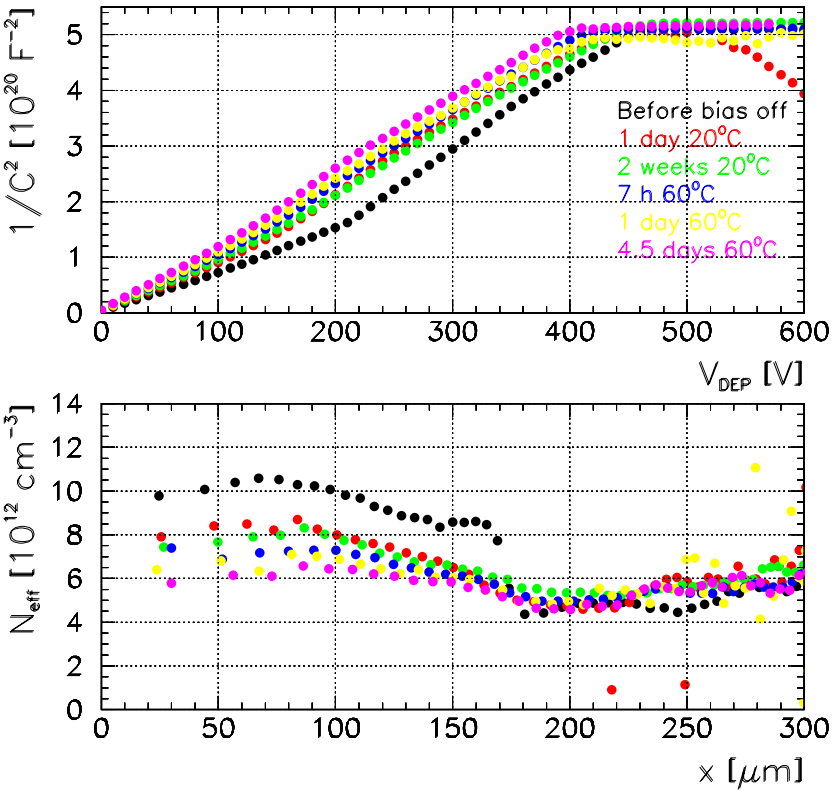

Figure 6.6: a) $1/C^2$ vs. V plot and b) N_{eff} distribution for the sample I3. Black dots show the measurements before switching off the bias. Time development after switching the bias off is shown with coloured circles.

tends to anneal out completely. Time constants for the annealing are increasing with the decreasing temperature (table 6.3). Difference for the forward biased sample (D2) is at the beginning showing the same behaviour as in the unbiased sample kept at the same temperature (UO6). However, after about four days at 20°C, when approximately a half of the difference has annealed out, it starts increasing again. This effect will be further discussed in section 6.2.2.

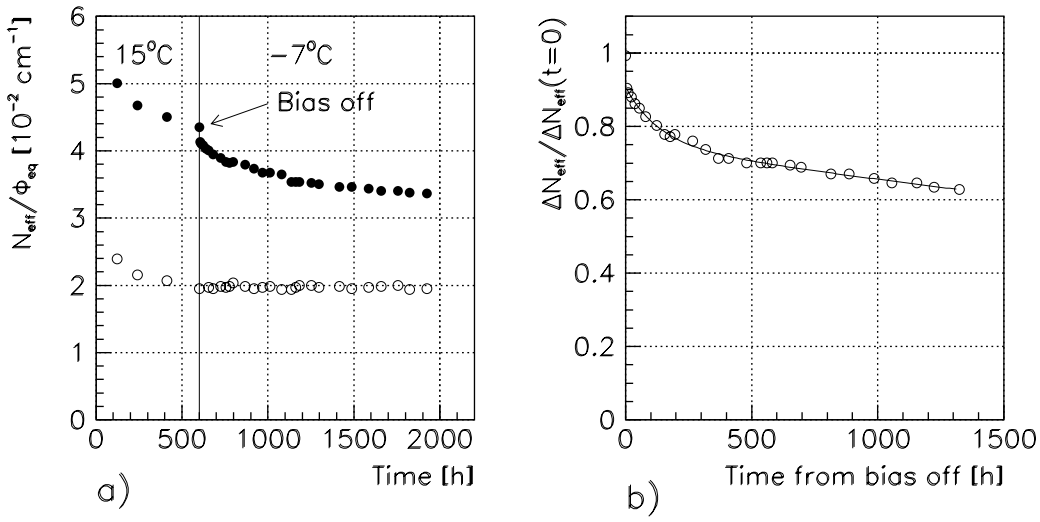

Figure 6.7: a) Time development of N_{eff} for the biased and unbiased diode from the pair BA2. They were kept at 15°C until the end of beneficial annealing. Then they were moved to -7°C and bias of the diode BA2B was switched off. b) Time development of the difference. Difference in N_{eff} normalised to the initial value is shown versus time from switching off the bias. Agreement of a two exponentials fit (eq. 6.4) with the measured data is also shown.

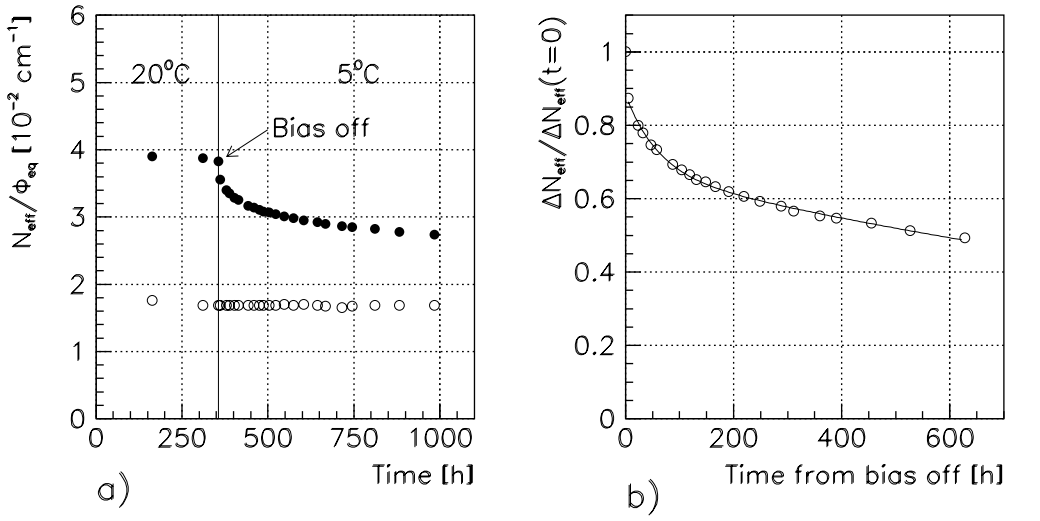

Figure 6.8: a) Time development of N_{eff} for the biased and unbiased diode from the pair BA4. They were kept at 20°C until the end of beneficial annealing. Then they were moved to 5°C and bias of the diode BA4B was switched off. b) Time development of the difference. Difference in N_{eff} normalised to the initial value is shown versus time from switching off the bias. Agreement of a two exponentials fit (eq. 6.4) with the measured data is also shown.

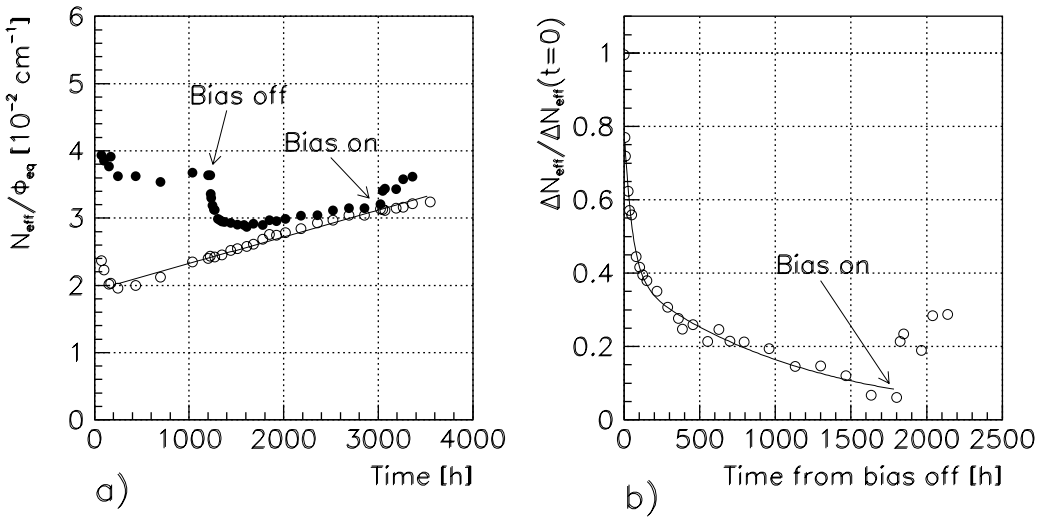

Figure 6.9: a) Time development of N_{eff} for the biased and unbiased diode from the pair UO6. They were kept at 20°C before and after the bias of the diode UO6B was switched off. b) Time development of the difference. Difference in N_{eff} normalised to the initial value is shown versus time from switching off the bias. Agreement of a two exponentials fit (eq. 6.4) with the measured data is also shown.

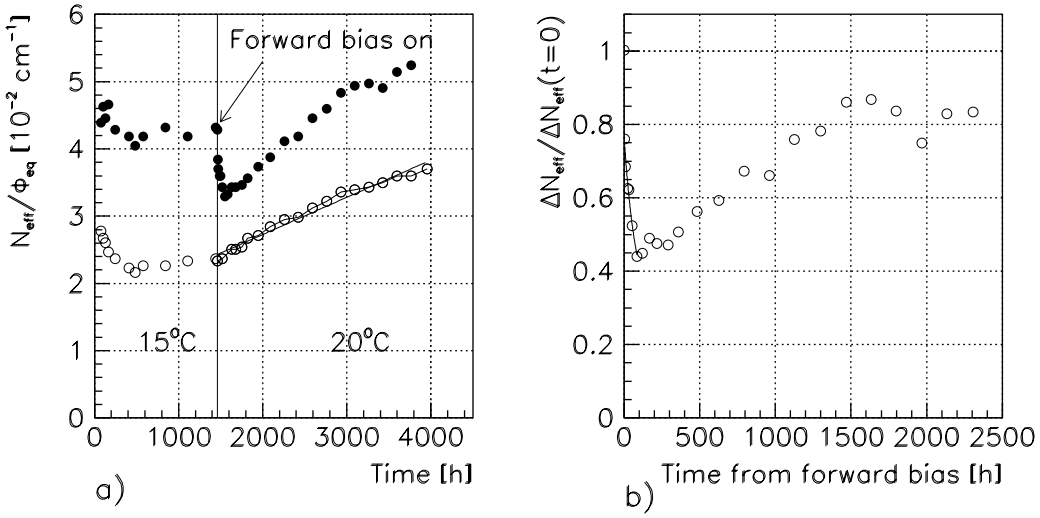

Figure 6.10: a) Time development of N_{eff} for the biased and unbiased diode from the pair D2. They were kept at 15°C until the end of beneficial annealing. Then they were moved to 20°C and 350V of reverse bias of the diode D2A was replaced by approximately 10V of forward bias. b) Time development of the difference. Difference in N_{eff} normalised to the initial value is shown versus time from switching off the bias.

Sample	T [°C]	C_1	τ_1 [h]	C_2	τ_2 [h]
BA2	-7	0.20±0.04	220±20	0.71±0.05	9000±1500
BA4	5	0.22±0.04	60±5	0.65±0.05	2100±200
UO6	20	0.44±0.04	42±10	0.41±0.05	1050±100

Table 6.3: Results of the two exponential fits (eq. 6.4) for samples BA2, BA4 and UO6.

6.2.1 Time Constants and Activation Energy

All samples show a fast[40] annealing of approximately 10% of the initial difference. Annealing of the remaining difference can be described by a two-exponential fit

$$\frac{N_{eff}(t)}{N_{eff}(t_0)} = C_1 e^{-\frac{t-t_0}{\tau_1}} + C_2 e^{-\frac{t-t_0}{\tau_2}} \quad , \tag{6.4}$$

where t_0 is the time of switching the bias off. Agreement of the fit with the measurements can be seen in figures 6.8b to 6.9b and fit results are given in the table 6.3.

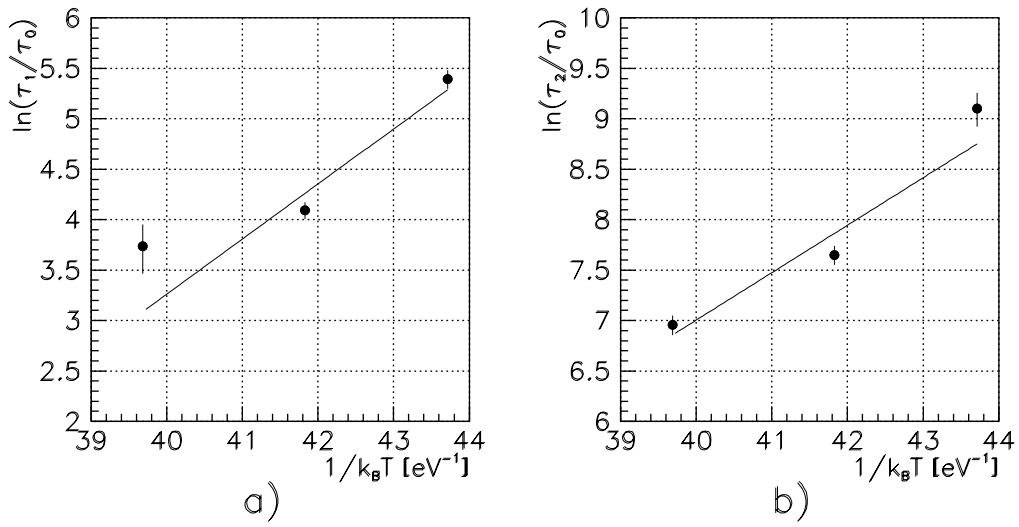

Figure 6.11: Arrhenius plots for a) fast and b) slow component of the annealing of the difference between biased and unbiased samples.

To determine activation energies for both processes, the Arrhenius relation

$$\tau(T) = \tau_0 e^{\frac{E_a}{k_B T}} \tag{6.5}$$

[40] Within the first 4 hours after switching the bias off, that being the time interval between the first measurements.

or

$$\ln \tau(T) = \ln \tau_0 + \frac{1}{k_B T} E_a \tag{6.6}$$

is used. If one plots $\ln(\tau(T))$ versus $1/k_B T$ (Arrhenius plot), the activation energy can be determined as the slope (fig. 6.11). One obtains an activation energy of $E_1 = 0.54 \pm 0.15\,\mathrm{eV}$ for the fast component and $E_2 = 0.47 \pm 0.15\,\mathrm{eV}$ for the slow one. Those are however only very preliminary results and further studies are necessary to obtain proper understanding of the described processes and to determine their parameters with better precision.

The conclusion that the activation energies of bias dependent defects are significantly lower than the activation energy for reverse annealing (about 1.3 eV [13, 14, 15]) can also be seen from figures 6.7a to 6.9a. At 20°C, the effect of decreasing of the slow component of bias-effect annealing is comparable to the effect of reverse annealing (see fig. 6.9a). This is however not the case for the samples at lower temperatures (5°C and -7°C). At those temperatures reverse annealing is frozen on the time scale of bias-effect annealing (figures 6.7a and 6.8a). The decay constant of the slow component at -7°C (about a year) is however still long enough to play an important role for the detector operation in the ATLAS environment. A careful planing of the operation scenario is thus necessary to obtain optimal operation conditions for the vertex detector.

6.2.2 Bistability

Bistability of the defects, responsible for bias dependent annealing, was checked on diodes S3. The test was started about 2 months (at 20°C) after the bias induced influence annealed out (see figure 6.12). There, it can also be seen that both samples have an equal reverse annealing constant after the annealing of bias dependent defects was completed. First the diode S3A (biased during, unbiased after irradiation) was biased with 200 V for about 3 weeks and then the bias was switched off. Then the same procedure was repeated for the diode S3B (unbiased during, biased after irradiation). The results of the test are shown in figure 6.12. One can see that for both samples about a 15% raise in N_{eff} appeared during the biased time interval, that disappeared within a day after the bias had been removed.

A similar behaviour was observed with the sample UO6B. After bias dependent defects annealed out, reverse bias of 500 V was applied again. As shown in figure 6.9, N_{eff} started to increase. However, after two weeks, when the raise amounted to about 30% of the initial difference, an accidental power cut-off caused the sample to remain unbiased. It is thus not possible yet to determine the portion of the initial difference that recovers after restoration of the bias voltage.

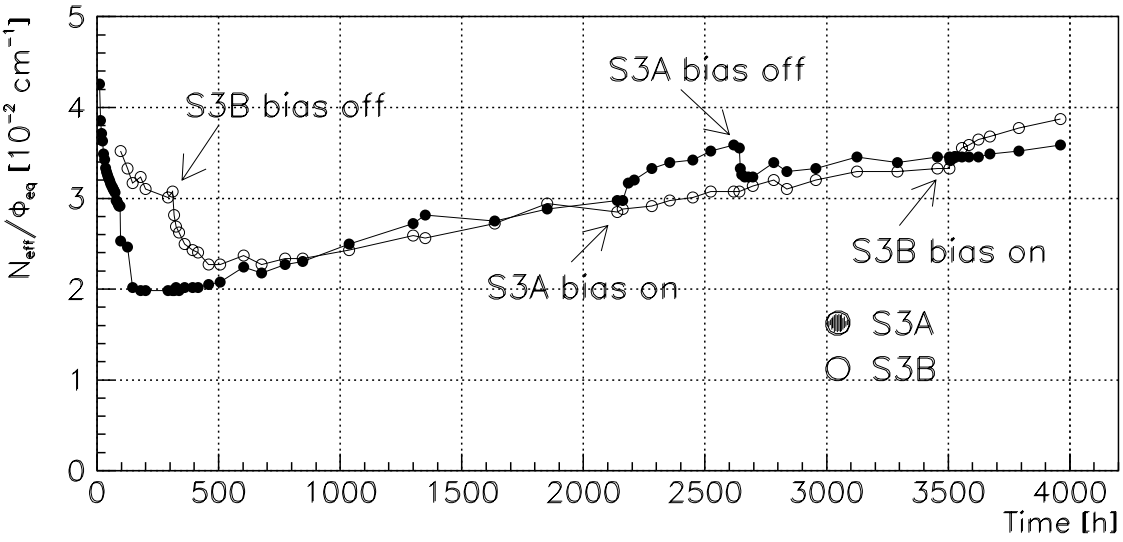

Figure 6.12: Time development of N_{eff} for both diodes from the S3 set. Samples were kept at room temperature.

The bistable nature of the defect is also shown in the time development of the difference of the diode D2A (fig. 6.10), where reverse bias was replaced by a small (about 10 V) forward bias. One can see that the initial difference between the biased (D2A) and unbiased (D2B) sample was annealing out at the beginning, but started to increase again after a few days at 20°C.

Bistable behaviour of all presented samples could also be explained by reaction 6.3, assuming it can proceed both ways

$$A + B \leftrightarrow C \ , \tag{6.7}$$

the equilibrium balance being distorted by the electric field sweeping out the mobile reaction ingredient. Two time constants of the bias effect annealing indicate two reactions responsible for its annealing. In that case results of the sample D2 are consistent with an assumption that the fast one can proceed both ways (reaction 6.7) while the slow one can not be reversed (reaction 6.3) and is, contrary to the fast one, not significantly affected by weak a forward bias.

Bias dependent annealing of bistable defects has also been reported by M. Moll et al. [54]. There are however a few major differences between the observed properties, indicating different defects than those reported in this work. As first, defects reported in [54] are only seen at irradiated samples, activated by heat treatment, charge injection by forward bias or illumination. The effect reported in this work are present since the

irradiation and no special treatment is needed to activate them. As second, though both anneal only if no reverse bias is applied, there is a big difference in time constants. While [54] reports simple exponential annealing with a time constant of about 10h at 20°C and an activation energy of 1.04±0.06 eV we observe annealing with two exponentials. The time constants of the fast component at 20°C is four times higher (40 h) and its activation energy about two times lower (≈0.5 eV). The slow component is even further off (about 1000 h at 20°C) with about the same activation energy as the fast component. All those differences indicate that processes responsible for the reported phenomena are not identical.

6.3 Influence on Reverse Current

Since diodes, dedicated to the study of the difference between biased and unbiased samples, had no connectable guard rings they could not be used to study the bias voltage effect on the reverse current. However, results presented in section 4.4.2, where time development of reverse current is discussed, can give conclusive results also on the bias effect. While no measurements of the short term annealing were performed for the unbiased diodes U3A and U3B, results on annealing at 60°C have been used to study long term annealing of the leakage current. Results presented there show no systematic difference among the samples. They are summed in figure 6.13 where the identical behaviour of biased and unbiased samples is clearly shown.

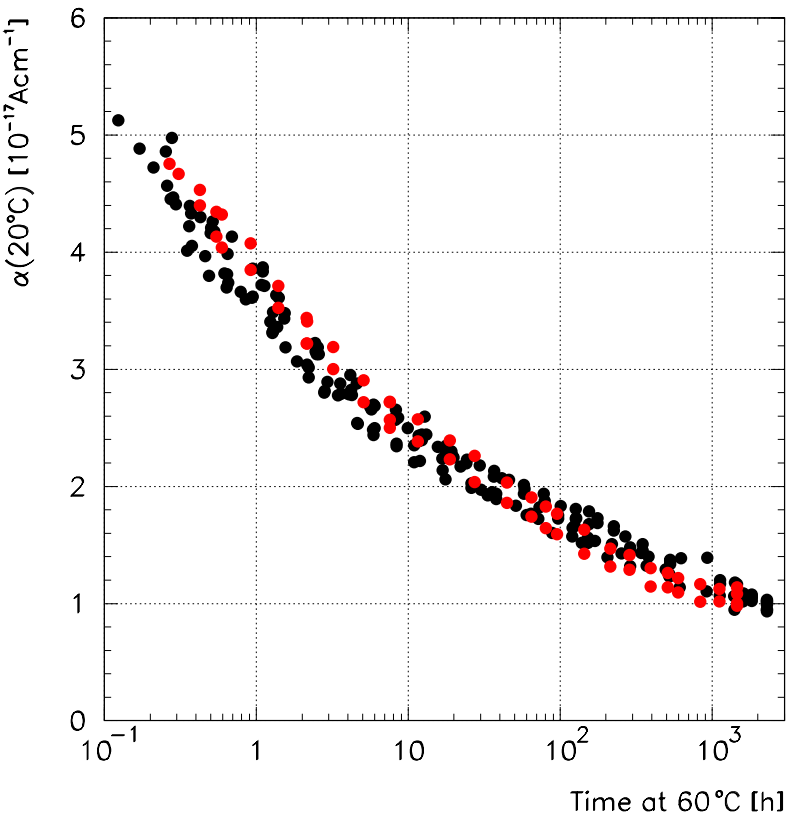

Figure 6.13: Comparison of reverse current time development for biased (black) and unbiased (red) diodes.

6.4 Conclusion

The influence of bias voltage on defect development was studied on neutron irradiated p^+-n-n^+ diodes. It was shown that the presence of electric field affects annealing of N_{eff} while no influence on the reverse current was observed. Difference in N_{eff} between fully biased and unbiased samples amounts to a factor of two after the end of beneficial annealing with the higher value for biased samples. The difference scales with total irradiation fluence and persists also during reverse annealing. Results on comparison of different biasing schemes are consistent with the assumption that electric field influences time development of defects created during the irradiation and not their introduction rates.

When the bias voltage is switched off, the difference starts to anneal. The time dependence is consistent with two exponentially decaying defects. Contributions of each defect type agree for samples annealed at -7°C and 5°C (about 20% for the fast and bout 70% for the slow component). They however differ for the sample annealed at 20°C (about 40% of each component). More systematic studies are therefore necessary before

making firm conclusions on this effect. Decay times at 20°C are about 40h for the fast component and six weeks for the slow one. Time development of the difference can be scaled to other temperatures using activation energies. First measurements of those were performed giving activation energies of $E_1 = 0.54 \pm 0.15$ and $E_2 = 0.47 \pm 0.15$ for the fast and slow component, respectively.

As detectors in the LHC environment can be left unbiased for a significant portion of time, a proper biasing and temperature scheme could reduce the observed effect. Since it takes more than a month at 20°C to anneal out 90% of the difference, the planned 14 days at 17°C will not be sufficient. And since the activation energy for the slow decrease of the bias induced difference is about twice lower than for the reverse annealing, prolonged warm periods would influence reverse annealing stronger than annealing of the bias dependent difference. The remaining 8 months at -7°C when the detector will not be operating and can be kept without bias, amount only to about half of the lifetime of the slow component. Due to long operation time and low irradiation flux this can however suffice to remove most of the effect. The bistable component may, on the other hand, amount to a signifficant increase of the full depletion voltage during the operation periods. A detailed study of the bias voltage effect is thus necessary. The data it will provide should be used to develop a scheme that will minimise the influence of bias effect and reverse annealing.

7

Comparison with Other Groups

While no previous measurements of bias voltage effect and neutron flux influence have been reported, a comparison of defect time development parameters with values, reported by other groups, is given below.

A comparison of reverse annealing parameters as obtained from the second order fit with a global survey, reported by A. Chilingarov et al. [15] and results obtained by S.J. Bates et al. [21] is given in table 7.1. A simmilar comparison was made for the first order

Parameter	biased	unbiased	global	Bates
g_C $[10^{-2}\mathrm{cm}^{-1}]$	4.0±0.6	2.2±0.4	1.77±0.07	2.5±0.3
g_Y $[10^{-2}\mathrm{cm}^{-1}]$	5.4±0.8	5.6±0.9	4.6±0.3	5.9±0.3
$k_2^Y(60°)$ $[10^{-18}\mathrm{cm}^3/\mathrm{s}]$	2.2±0.4	4.6±0.1	7.5^{+15}_{-2}	/

Table 7.1: A comparison of reverse annealing parameters g_C, g_Y and k_2^Y as obtained from the second order fit (eq. 4.7). Values for biased samples is the average of samples I3, D3 and B3, table 4.4. g_Y and k_2^Y are however ambiguous due to partial bias at late stage of reverse annealing. Values for unbiased samples is the average for samples U3A and U3B, table 6.1. In both data 15% systematic error on the dosimetry is included in the quoted error. Results are compared with a recent global survey [15] and results from S.J. Bates et al. [21].

fit, using data reported by H.J. Ziock et al. [45] (table 7.2).

The slope at the initial stage of reverse annealing can be compared with the results from Ziock [45] and ROSE report [13]. While Ziock uses first order model, a second order dynamics with time constant inversly proportional to the fluence is suggested in ROSE report

$$k^Y(\Phi_{eq}) = k_0^Y \cdot \frac{1}{\Phi_{eq}} \cdot e^{-\frac{E_a}{k_B T}} \tag{7.1}$$

Parameter	biased	unbiased	Ziock
g_C $[10^{-2}\mathrm{cm}^{-1}]$	4.1±0.6	2.3±0.4	2.1
g_Y $[10^{-2}\mathrm{cm}^{-1}]$	4.7±0.7	4.9±0.7	7.5
$k_1^Y(60°)$ $[10^{-6}\mathrm{s}^{-1}]$	3.9±0.6	8.2±0.3	12

Table 7.2: A comparison of reverse annealing parameters g_C, g_Y and k_1^Y as obtained from the first order fit (eq. 4.6). Values for biased samples is the average of samples I3, D3 and B3, table 4.4. g_Y and k_1^Y are ambiguous due to partial bias at late stage of reverse annealing. Values for unbiased samples is average for samples U3A and U3B, table 6.1. In both data 15% systematic error on the dosimetry is included in the quoed error. Results are compared with values from Ziock parametrisation [45]. A relative damage factor 0.72 [57] was used to normalise Ziock data (647 and 800 MeV protons) to 1 MeV neutrons. Errors for Ziock data were not given in [45].

with $k_0^Y = (1.9 \pm 1.2) \cdot 10^{16}\mathrm{cm/s}$ and E_a=1.31 eV. From equations 4.9 and 4.10 one obtains $K_Y^{lin} = g_Y^2 k_0^Y$ for the given model. A comparison with K_Y^{lin} for 20°C (from table 4.6) and for 60°C (from table 4.5) is given in the table 7.3.

Parameter	biased	unbiased	Ziock	ROSE
$k_Y^{lin}(20°\mathrm{C})$ $[10^{-10}\mathrm{cm}^{-1}\mathrm{s}^{-1}]$	/	12±3	5.6	12±9
$k_Y^{lin}(60°\mathrm{C})$ $[10^{-7}\mathrm{cm}^{-1}\mathrm{s}^{-1}]$	2.2±0.5	3.3±0.5	2.5	6±4.5

Table 7.3: A comparison of reverse annealing parameters k_Y^{lin} (see equation 4.10) at 20°C and 60°C with results from ROSE report [13] and Ziock et al. [45]. $g_Y = (4.6 \pm 0.3) \cdot 10^{-2}\mathrm{cm}^{-1}$ from the global data (table 7.1) was used with ROSE reverse annealing time constant. A relative damage factor 0.72 [57] was used to normalise Ziock data (647 and 800 MeV protons) to 1 MeV neutrons. Errors for Ziock data were not given in [45]. A 15% systematic error on the dosimetry is included in the error on our data.

Results on long term annealing of reverse current were compared with results from M. Moll et al. [35] (table 7.4). As already shown in section 4.4.2, all parameters agree well within the given errors.

To conclude, in all observed parameters good agreement of values for unbiased samples with results from other sources was found. This is however not the case for the biased samples. For those, the value of g_C is about twice the value from other sources, while reverse annealing constants as obtained by different methods show a systematicaly lower values as compared to data from the literature. Those observations agree well with the effect of bias voltage as reported in this work. Parameters of long term annealing of reverse current agree well with values, reported by M. Moll et al. [35]. OMENIM, DA

	α_E [10^{-17}A/cm]	τ_E^α [h]	α_L [10^{-17}A/cm]	τ_L^α [years]
This work	1.25± 0.3	1.7± 0.6	0.29± 0.08	7± 6
Moll	1.01± 0.38	1.5± 0.4	0.33± 0.026	$6.6^{+45}_{-4.6}$

Table 7.4: A comparison of parameters of the long term annealing of reverse current (eq. 8.1) with results from M. Moll et al. [35]. A 15% systematic error on the dosimetry is included in the error on our data.

SO IMELI OSTALI ALPHA NESKONCNO?

8

Conclusions

A systematic study of radiation damage in silicon bulk was performed under controlled conditions. Two irradiation sites at the TRIGA reactor near Ljubljana were equipped to provide mounting, cooling, biasing and measurements of samples during neutron irradiations. They were used to irradiate a number of high resistivity ($\rho = 3 - 30$ kΩcm) p^+-n-n^+ diodes used in this work. Irradiation flux, sample temperature and bias voltage were carefully controlled during irradiations to obtain good control over irradiation conditions.

The resented results were obtained from more than two years of measurements of the bulk properties of irradiated samples. Full depletion voltage and reverse current were measured in regular intervals both during and after irradiation. To follow defect annealing and reverse annealing under well defined conditions, storage temperature and bias voltage were controlled during irradiation and storage.

In the scope of this work, the first systematic study of the dependence of the radiation induced bulk damage in silicon on the *neutron flux* has been performed. *Fast annealing of N_{eff} and reverse current* were studied at temperatures from 0 to 15°C. Afterwards, most samples were heated to 60°C to accelerate time development. *Long term annealing of reverse current* and *reverse annealing of N_{eff}* were studied and kinematics of the responsible processes was searched for. Finally, the *effect of the bias voltage* on defect development was discovered [55] and first results of its study are presented.

Fast annealing of N_{eff} and reverse current A significant annealing of both N_{eff} and reverse current on a day scale even at 0°C was observed [56]. Though it bears no great importance for LHC experiments, it should be taken into account when results from different groups are compared.

Reverse annealing of N_{eff} A study of the initial phase of reverse annealing of N_{eff} on a set of dedicated samples gave clear evidence for a linear dependence of reverse annealing time constant k_Y^{lin} on irradiation fluence. This means that at least at the initial stage, relevant for the LHC experiments, the reverse annealing rate is governed by a first order process.

Long term annealing of reverse current Study of the long term annealing of reverse current showed no saturation up to a few months at 60°C. An effective ansatz

$$\alpha(t) = \alpha_E e^{-t/\tau_E^\alpha} - \alpha_L \ln(t/\tau_L^\alpha) \tag{8.1}$$

was found to fit the results. Lack of a natural explanation of the logarithmic behaviour however indicates the need for better understanding of the processes responsible.

Effect of neutron flux Irradiation flux was varied from a few times 10^8 n/cm^{2}s to a few times 10^{15} n/cm^{2}s to check for the effect of neutron flux on defect generation. No significant difference among samples irradiated with different fluxes was observed neither in radiation induced change of N_{eff} nor in generated reverse current [56]. The investigated flux range covers all presently available neutron sources and it seems safe to extrapolate results from neutron irradiation studies to the expected flux at LHC of about 10^6 n/cm^{2}s.

Effect of bias voltage Strict control of the biasing condition both during and after irradiation lead to the discovery of bias influence on defect development. Its origin was found not to be in the creation of defects but in their annealing. Fully biased samples gave about a factor of two higher N_{eff} values at the plateau after beneficial annealing as compared to unbiased ones. The difference, however, annealed out if the bias voltage was removed. Decrease of the difference can be described by two exponentials with time constants at 20°C of about 40 h for the fast component ($\approx 45\%$) and six weeks for the slow one ($\approx 40\%$). Activation energy of both reactions is around 0.5 eV. The remaining difference anneals out in less than 4 hours at all measured temperatures (-7, 5 and 20°C). Few ten percents of the difference however recovers if the sample is biased again. No effect of the bias voltage on time development of reverse current was observed.

Comparison with previous results In all parameters, previously studied by other groups (reverse annealing of N_{eff} and long term annealing of reverse current), a good agreement of our results with reported values was found. The first systematic search for an effect of neutron flux on defect creation was performed in this work. Finaly, in the scope of this work the effect of bias voltage on annealing of effective dopant concentration was discovered.

Implications for LHC experiments Significant effect of bias voltage on annealing of effective dopant concentration has to be taken into account when estimatig radiation induced changes of detector properties during LHC operation. Decreasing of the difference after switching off the bias implies that detectors should not be biased except during data taking. Long time constant of the difference annealing (about 1 year at -7°C) and low activation energy for responsible process (≈ 0.5 eV) limits its annealing during intervals with no applied bias. Furthermore, observed bistability of at least some of defects, responsible for the difference, reduces the effect of the difference annealing. Further study of the bias effect are thus necessary. Resulting data should be used in a revised operation scenario to minimise combined influences of bias effect and reverse annealing.

9

Povzetek doktorskega dela

9.1 Uvod

Silicijevi pozicijsko občutljivi detektorji igrajo pomembno vlogo pri sodobnih eksperimentih s področja fizike osnovnih delcev. Zaradi izjemno dobre krajevne ločljivosti[41], hitrega odziva in majhne količine materiala se uporabjajo predvsem kot tako imenovani verteks detektorji. Ti se nahajajo najbliže točki interakcije in so namenjeni čim natančnejši rekonstrukciji točke razpada primarnih in sekundarnih delcev.

V vlogi verteks detektorjev bodo silicijevi detektorji igrali pomembno vlogo tudi v načrtovanih eksperimentih na trkalniku LHC. Ta bo pričel delovati v pričetku naslednjega tisočletje v Evropskem centru za fiziko delcev CERN pri Ženevi. Trkalnik bo omogočal trke med protoni s težiščno energijo 14 TeV in luminoznostjo od 10^{33} do $10^{34}/\mathrm{cm}^2\mathrm{s}$. Razpoložjive energije bodo omogočale študij vrste novih procesov, med katerimi je najpomembnejše iskanje Higgsovega bozona, s katerim bi lahko razložili izvor mase.

Posledica izjemno visoke luminoznosti in razpoložljive energije pa bo visoko sevalno ozadje, še posebej v bližini interakcijske točke, kjer se bodo nahajali verteks detektorji[42]. To bo povzročilo znatne sevalne poškodbe. Da bi omogočili njihovo delovanje tekom desetih let, kolikor bo trajal eksperiment, je potrebno dobro razumevanje nastanka in razvoja sevalnih poškodb. Le dobro načrtavani detektorji in pretehtan scenarij delovanja lahko obdrže posledice sevalnih poškodb na sprejemljivi ravni.

Sevalne poškodbe silicijevih detektorjev se izražajo na dva načina. Poškodbe površine so posledica naboja, zbranega na meji med polprevodnikom in oksidom. Te povečajo površinske tokove in zmanjšajo upornost med pasovi, kar vpliva na zbiranje naboja. Druga

[41] S silicijevimi pasovnimi detektorji so dosegli ločljivosti do 1 μm [1].

[42] Pri eksperimentu ATLAS, v okviru katerega je bilo opravljeno pričujoče delo, se bo silicijev pasovni del verteks detektorja (SCT - Semi-Conductor Tracker) nahajal na radijih od 30 do 52 cm. Pričakovane sevalne poškodbe, nastale v 10 letih delovanja, bodo ekvivalentne poškodbam približno 10^{14} n/cm^2.

vrsta poškodb so globinske poškodbe[43], to so poškodbe po celotni prostornini polprevodnika. Posledica le-teh je povečanje zapornega toka, višja napetost polnega osiromašenja[44] in slabše zbiranja naboja.

Predstavljeno delo je posvečeno študiju globinskih poškodb v siliciju, nastalih pri obsevanju z nevtroni. Novi rezultati so posledica natančnega nadzora pogojev tako med kot po obsevanju. Še posebej je treba omeniti natančen nadzor napajalne napetosti, ki je vodil do odkritja vpliva napetosti na razvoj poškodb. Možnost spreminjanja moči uporabljenega reaktorja[45] je omogočila tudi študij vpliva hitrosti obsevanja na nastanek sevalnih poškodb.

9.1.1 Osnove delovanja

Silicijevi pozicijsko občutljivi detektorji so v osnovi polje diod z izbrano geometrijo na silicijevi ploščici. Kadar je na njih napetost v zaporni smeri delujejo podobno ionizacijski celici. Pare elektron-vrzel, ki nastanejo ob prehodu ionizirajočega delca, zaznamo kot tokovni sunek, segmentacija diod pa omogoči določitev mesta prehoda ionizirajočega delca.

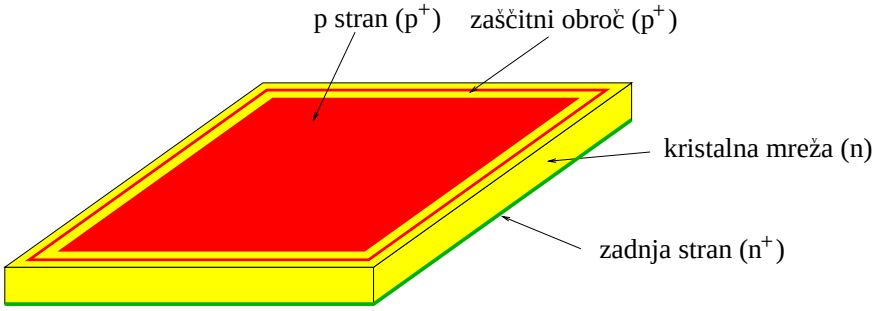

Figure 9.1: Shematični prikaz diod, uporabljanih v tem delu. Prikazana je tudi struktura p strani z zaščitnim obročem. Zaradi visoke koncentracije primesi je p stran označena kot p^+.

Predstavljeno delo je bilo namenjeno šudiju globinskih poškodb silicijeve mreže, zato smo želeli vpliv poškodb površine čim bolj omejiti. V ta namen so preproste diode s površino reda 1 cm^2 mnogo primernejše kot detektorji z integriranimi površinskimi elementi, kot so uporniki in kondenzatorji. Poleg manjšega vpliva površinskih poškodb pa je prednost tudi preprostejša izdelava, saj ta omogoča večjo ponovljivost in nižjo ceno.

[43] bulk damage

[44] Napetost polnega osiromašenja (V_{FD}) je napetost, potrebna za osiromašenje celotne prostornine vzorca.

[45] Vzorci so bili obsevani v reaktorju TRIGA v Podgorici, ki je del reaktorskega centra Instituta Jožef Stefan.

Skica preproste diode, kakršne smo uporabljali v predstavljenem delu, je prikazana na sliki 9.1.

K izmerjenem signalu prispevajo le pari, zbrani v osiromašenem področju diode. Za čim večje razmerje med signalom in šumom je torej porebno osiromašiti celotno prostornino detektorja. Da bi to dosegli s čim nižjimi napetostmi, se na eni strani spoja p-n (običajno n) uporablja šibko dopiran polprevodnik. V tem pimeru velja za globino osiromašenega področja $w(V)$

$$w(V) = \sqrt{\frac{2\epsilon_{Si}\epsilon_0}{e_0\, N_{eff}}\, V} \ . \tag{9.1}$$

kjer je N_{eff} efektivna koncentracija primesi[46], e_0 osnovni naboj, $\epsilon_{Si}\epsilon_0$ dielekričnost silicija in V napetost v zaporni smeri. Napetost polnega osiromašenja V_{FD} je tako določena z enačbo

$$V_{FD} = \frac{e_0 N_{eff} W^2}{2\epsilon_{Si}\epsilon_0}, \ , \tag{9.2}$$

kjer je W debelina diode oz. detektorja. Tipična debelina pozicijsko občutljivih silicijevih detektorjev je 300 μm, napetosti polnega osiromašenja pa se gibljejo med 10 in 100 V.

Napetost polnega osiromašenja merjenega vzorca lahko določimo z merjenjem C/V karakteristike (kapaciteta v odvisnosti od napetosti). Če je N_{eff} konstantna po globini vzorca je odvisnost kapacitete od zaporne napetosti podana z

$$C(V) = \frac{\epsilon_{Si}\epsilon_0 S}{w} = \sqrt{\frac{\epsilon_{Si}\epsilon_0 e_0 N_{eff}}{2V}} S \ , \tag{9.3}$$

kjer je S površina vzorca. Za izpeljavo smo uporabili $C(V_0) = (\frac{dQ}{dV})_{V=V_0}$, enačbo 9.1 in zvezo $Q = e_0 N_{eff} S w$. Iz enačbe 9.3 je razvidno, da dokler ne osiromašimo celotnega vzorca, kapaciteta upada z naraščajočo napetostjo. Za napetosti, višje od napetosti polnega osiromašenja, pa je kapaciteta od napetosti neodvisna. Tako lahko napetost polnega osiromašenja določimo s položajem preloma, N_{eff} pa iz strmine grafa $1/C^2$ proti V

$$\frac{d(1/C^2(V))}{dV} = \frac{2}{e_0\epsilon_{Si}\epsilon_0 N_{eff} S^2} \ . \tag{9.4}$$

9.1.2 Tvorba sevalnih poškodb

Energijske izgube ob prehodu delca skozi silicijev kristal lahko razdelimo na ionizirajoče in neionizirajoče. Zaradi hitre rekombinacije prostih nosilcev naboja ionizirajoče poškodbe

[46] Efektivna koncentracija promesi je določena kot absolutna vrednost razlike med koncentracijo donorjev (N_D) in akceptorjev (N_A) $N_{eff} = |N_D - N_A|$.

ne povzroče dolgotrajnejših sprememb mreže. V nasprotju z njimi pa neionizirajoči del oddane energije (NIEL - non-ionizing energy loss) povzroči trajne poškodbe kristalne mreže in sicer premik atoma iz kristalne mreže in jedrske reakcije. Vpliv sprememb zaradi jedrskih reakcij je pri obsevanjih, ki so del predstavljenega dela, zanemarljiv. Tako je edini za nas pomemben proces premik Si atomov z njihovega mesta v kristalni mreži, pri čemer nastanejo vrzeli (V) in medmrežni silicijevi atomi (I). Večina le teh se rekombinira, del jih medsebojno reagira (npr. tvorba para vrzel-vrzel V_2), del pa jih potuje po mreži in reagira z ostalimi primesmi (npr. tvorba kompleksa vrzel-fosfor VP).

Če k sevalnim poškodbam prispeva le neionizirajoči del oddane energije (tako imenovana NIEL hipoteza), lahko odvisnost od vrste delca popišemo s poškodbeno funkcijo (damage function) $D(E)$. Le ta za izbrano vrsto vpadnega delca in kristala popiše NIEL v odvisnosti od energije vpadnega delca. Za lažjo primerjavo poškodb z različnimi delci se poškodbe običajno primerjajo s poškodbami, ki bi jih povzročili nevtroni z energijo 1 MeV. Tako lahko določimo ekvivalentno fluenco Φ_{eq}, to je fluenco nevtronov z energijo 1 MeV, ki bi povzročila enake sevalne poškodbe kot fluenca Φ_A delcev vrste A z energijsko porazdelitvijo $\frac{d\Phi_A}{dE}$

$$\Phi_{eq} \;=\; \kappa_A \cdot \Phi_A \;, \tag{9.5}$$

kjer je κ_A faktor poškodb (hardness factor)

$$\kappa_A = \frac{\langle D_A \rangle}{D(1MeVn)} \;=\; \frac{1}{D_n(1MeV)} \cdot \frac{\int_{E_{min}}^{E_{max}} D_A(E)\, \frac{d\phi_A}{dE}(E)\, dE}{\int_{E_{min}}^{E_{max}} \frac{d\phi_A}{dE}(E)\, dE}. \tag{9.6}$$

Napake kristalne mreže, ki nastanejo pri obsevanju, lahko vplivajo na njene makroskopske lastnosti na več načinov.

Zaporni tok Zaradi sevanja nastale poškodbe lahko v energijsko režo vnesejo nove energijske nivoje. S tem se poveča verjetnost za zajetje elektrona iz valenčnega pasu in njegovo emisijo v prevodni pas, to je verjetnost za tvorbo para elektron-vrzel. Pri tem k tvorbi parov največ prispevajo energijski nivoji v bližini sredine energijske reže.

Glavni prispevek k zapornemu toku v obsevani diodi je določen z generacijo parov v osiromašenem področju

$$j_{SCR} \;=\; e_0 r^{pair} w \;, \tag{9.7}$$

kjer je j_{SCR} gostota generacijskega toka, e_0 osnovni naboj, w debelina osiromašenega področja in r^{pair} hitrost tvorbe parov. Ker je r^{pair} sorazmerena z gostoto nivojev v bližini

sredine energijske reže, ta pa s fluenco, lahko povezavo med zapornim tokom in fluenco opišemo z enačbo

$$\frac{j_{SCR}}{w} = \frac{I}{V} = \alpha \cdot \Phi_{eq} \ , \tag{9.8}$$

kjer je α količnik naraščanja zapornega toka in V prostornina osiromašenega področja.

Efektivna koncentracija primesi Primesi lahko leže v bližini (reda velikosti $k_B T$) prevodnega oz. valenčnega pasu (plitke primesi) ali pa so od njiju bolj oddaljeni (globoke primesi). Vpliv globokih primesi na efektivno koncentracijo dopantov pa je pomemben le v osiromašenem področju, kjer k prostorskemu naboju prispevajo donorji iz zgornje polovice in akceptorji iz spodnje polovice energijske špranje. Ti torej povečajo efektivno gostoto primesi N_{eff} in s tem zvečajo napetost polnega osiromašenja.

V neobsevanih polprevodnikih je koncentracija globokih primesi običajo zanemarljiva, pomembne so le plitki primesi kot sta P in B. Pri obsevanju pa nastajajo tudi globoki primesi, predvsem akceptorji, njihova koncentracija pa je sorazmerna s fluenco. Pri obsevanju silicija tipa n torej efektivna koncentracija primesi zaradi nastajanja akceptorskih stanj v pričetku upada, v točki inverzije se spremeni v tip p, nato pa N_{eff} zopet narašča. Pri visokih fluencah tako lahko N_{eff} in s tem napetost polnega osiromašenja tako narasteta, da onemogočita normalno delovanje detektorja. To naraščanje je ena najhujših ovir za delovanje silicijevih detektorjev v visoko sevalnem okolju.

Medtem ko je naraščanje koncentracije globokih akceptorjev s fluenco experimentalno dobro potrjeno [14, 20, 29, 30, 46], pa vpliv obsevanja na začetne plitke donorje še ni dokončno razjasnjen. Po nekaterih modelih njihova koncentracija s fluenco eksponentno upada [29, 30], medtem ko se po drugih le kompenzirajo z nastalimi akceptorji [31].

Zbiranje naboja Globoki nivoji, nastali pri obsevanju, zmanjšajo življenjski čas prostih nosilcev naboja in s tem število le-teh. Ker je življenjski čas obratno sorazmeren s koncentracijo globokih nivojev, le ta pa je sorazmerna s fluenco je torej tudi življenjski čas obratno sorazmeren s fluenco. Vendar pa na zbiranje naboja vplivajo le nivoji z emisijskim časom, dolgim v primerjavi s časom zbiranja naboja.

Meritve kažejo, da je padec signala zaradi slabšega zbiranja naboja pri fluencah okoli 10^{14} n/cm^2 približno 10% za zbiralne čase reda 10 ns [13, 34].

9.2 Reaktor, merilni sistem in metode

9.2.1 Reaktor

Vzorci, uporabljeni za predstavljeno delo, so bili obsevani v eksperimentalnem reaktorju TRIGA Instituta Jožef Stefan v Ljubljani. Moč reaktorja je nastavljiva v obsegu od nekaj W do 250 kW, mogoče pa je tudi delovanje v pulznem načinu. Tako je na danem obsevalnem mestu možno obsevanje vzorcev z fluksi nevtronov, ki se razlikujejo za več redov velikosti.

Na reaktorju TRIGA sta bili za študij sevalnih poškodb v siliciju opremljeni dve obsevalni mesti:

Suha celica V suhi celici je mogoče obsevanje vzrocev z dimenzijami do 10×15 cm^2. Mogoče je hlajenje do -20°C, napajanje ter C/V in I/V meritve[47] med in po obsevanju. Kljub uporabi fisijske plošče, ki zveča flux hitrih nevtronov (nad 0.1 MeV), pa le-ta ne preseže $4 \cdot 10^8$ n/cm^{2}s.

Faktor sevalnih poškodb κ je bil določen na osnovi obstoječih meritev nevtronskega spektra [36] na

$$\kappa_{SC} = 0.99 \pm 0.06 \ . \tag{9.9}$$

Skupaj z napako na meritvi fluence, ki je okoli 15%, je torej ekvivalentna fluenca 1 MeV nevtronov določena s približno 17% napako.

Obsevalni kanal F19 V obsevalnem kanalu F19 je mogoče obsevanje vzorcev z dimenzijami do približno 15×50 mm^2. Z vodnim hlajenjem lahko hladimo vzorce do 0°C. Tudi tu je poskrbljeno za napajanje vzorcev ter C/V in I/V meritve.

Ob normalnem obratovanju reaktorja je fluks hitrih nevtronov (nad 0.1 MeV) pri polni moči reaktorja (250 kW) približno $2 \cdot 10^{12}$ n/cm^{2}s in je sorazmeren z močjo. V pulznem načinu lahko dosežemo fluenco hitrih nevtronov okoli 10^{14} n/cm^2 v pulzu dolžine približno 20 ms, čemur ustreza povprečni fluks okoli $5 \cdot 10^{15}$n/cm^{2}s.

Spekter nevtronov je bil določen z meritvijo in s simulacijo. Vrednost faktorja sevalnih poškodb je

$$\kappa_{F19} = 0.90 \pm 0.03 \ . \tag{9.10}$$

Sistematska napaka na meritvi fluence je okoli 15%, dodatna napaka posamezne meritve pa okoli 5%.

[47] Meritve odvisnosti kapacitete C in zapornega toka I od napajalne napetosti V.

9.2.2 Merilni sistem

Merilni sistem v laboratoriju Glavni komponenti laboratorijskega merilnega sistema sta HP4284A LCR meter in KEITHLEY 237 visoko-napetostni izvor in merilnik toka. Njuna povezava z merjenim vzorcem je prikazana na sliki 9.2. Kondenzatorji in upori ščitijo LCR meter pred visoko napetostjo in spremembami impedance napetostnega izvora. Tako HP4284A kot KEITHLEY 237 sta povezana z osebnim računalnikim, ki vodi meritev ter bere in hrani rezultate. Program vzporedno spremlja tudi temperaturo vzorca. To merimo s toplotnim senzorjem Pt100, povezanim s temperaturnim kontrolerjem Yokogawa UT15. Med meritvami so vzorci v hladilni skrinji, stabilizirani na 5°C. Temperaturno stabilizirane omare uporabljamo tudi za shranjevanje vzorcev. Za pospeševanje časovnega razvoja pooškodb smo vzorce segrevali v pečici pri 60°C, s temperaturo stabilizirano na ±2°C.

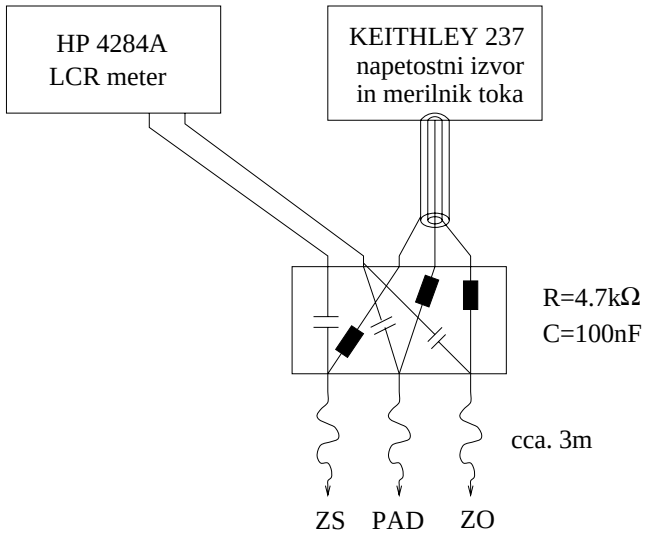

Figure 9.2: Povezava laboratorijskega merilnega sistema z merjenim vzorcem. Oznake merilnih žic pomenijo: ZS - zadnja (n^+) stran, ZO - zaščitno obroč, PAD - p^+ stran diode.

Merilni sistem na reaktorju Merilini sistem na reaktorju je v osnovi enak sistemu, ki smo ga uporabljali v laboratoriju. Glavna razlika je v tem, da je KEITHLEY 237, ki je hkrati izvor napetosti in merilnik toka, nadomeščen z dvema enotama in sicer KEITHLEY 617 kot merilnikom toka in visoko-napetostnim izvorom Wentzel. Poleg tega je HP4284A nadomeščen z preprostejšo izvedbo HP4263B, ki omogoča meritve le pri štirih vnaprej določenih frekvencah merilne napetosti (100 Hz, 1 kHz, 10 kHz in 100 kHz). Vendar te razlike nimajo opaznega vpliva na potek meritev in analizo podatkov.

9.2.3 Opis meritve in analize podatkov

C/V meritve Kapaciteto vzorca merimo z Hewlet-Packard LCR metrom. Ta meri amplitudo in fazni zamik toka kot odziv na izmenično merilno napetost. Tako določeno kompleksno impedanco lahko po enem od vgrajenih modelov ekvivalentnih vezij pretvori v druge parametre. Ker merjene diode blizu polnega osiromašenja najbolje opišeta paralelno vezana kondenzator in upor, smo za pretvorbo izbrali paralelni RC model.

Pri meritvah odvisnosti kapacitete od zaporne napetosti naložimo izmenično merilno napetost[48] na enosmerno zaporno napetost visoko-napetostnega izvora. Merilni program v izbranih korakih dviga napetost in pri vsaki izmeri kapaciteto vzorca. Rezultat meritve poda v obliki krivulje $C^{-2}(V)$ (slika 9.3, barvne točke). Napetost polnega osiromašenja določimo iz presečišča premic, prilagajanih na naraščajoči del pred prelomom in ravni del po njem (slika 9.3). Ker je tako določena napetost odvisna od frekvence merilne napetosti in temperature [16, 17], so vse laboratorijske meritve potekale pri referenčni temperaturi (5°C). Kapaciteta je bila merjena pri sedmih različnih frekvencah (1 kHz, 3 kHz, 10 kHz, 30 kHz, 100 kHz, 300 kHz in 1 MHz), za dolčitev napetosti polnega osiromašenja pa smo uporabljali meritev pri 10 kHz.

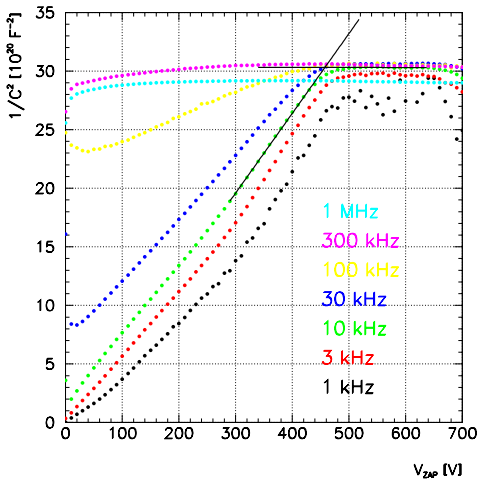

Figure 9.3: C/V meritev pri različnih frekvencah merilnega signala. Napetost polnega osiromašenja (455 V) je določena kot presečišče premic, prilagajanih na naraščajoči del pred prelomom in ravni del po njem.

Glavni vir napake uporabljene metode je sistematska napaka zaradi izbora merilne

[48] Amplituda merilne napetosti je nastavljiva v območju med 5 mV in 2 V, običajno smo uporabljali 1 V.

frekvence in temperature, ki smo jo ocenili na pod 10%. Tako k napaki na konstantah hitrosti tvorbe poškodb (g) največ prispeva sistematska napaka dozimetrije (15%).

Meritve zapornega toka Medtem ko je prispevek generacijskega toka sorazmeren s korenom zaporne napetosti (glej enačbi 9.7 in 9.1) in narašča sorazmerno s fluenco, je površinski tok močno odvisen od zunanjih pogojev in izdelave[49]. Zato smo raziskave omejili na študij generacijskega toka. Vendar pri invertiranih vzorcih ločevanje obeh prispevkov ni preprosto, saj so zaščitni obroči polno učinkoviti šele pri polnem osiromašenju [51]. To se v I/V krivulji izraža kot hrbet, ki se zravna pri napetosti polnega osiromašenja (slika 9.4). Tako je generacijski tok določen kot vrednost zapornega toka v minimumu za hrbtom. Pri diodah z dobro delujočimi zaščitnimi obroči je napaka opisane metode nekaj odstotkov. Napaka parametra α je tako določena z napako dozimetrije (okoli 15%).

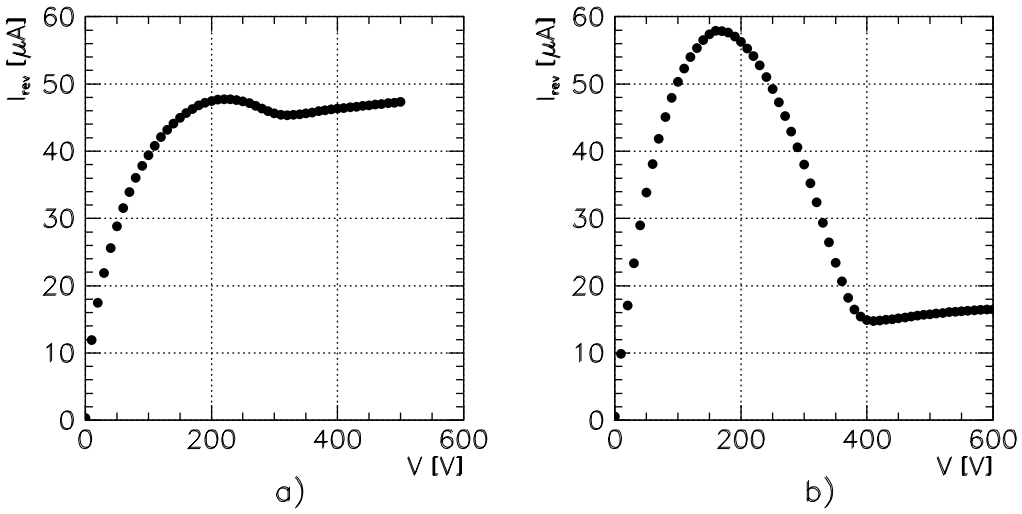

Figure 9.4: Primer I/V meritve diode a) v začetni fazi (po 5 dneh pri 5°C) in b) v pozni fazi (po 5 dneh 60°C) okrevanja zapornega toka. Generacijski tok je določen kot vrednost zapornega toka v minimumu za hrbtom.

9.3 Časovni razvoj poškodb

9.3.1 Uvod

Časovni razvoj poškodb, nastalih pri obsevanju, lahko poteka po treh scenarijih:

[49] Vlage, načina rezanja diode itd.

- Poškodbe so lahko časovno stabilne.
- Električno aktivne poškodbe se lahko spremene v neaktivne (okrevanje).
- Električno neaktivne poškodbe se lahko spremene v električno aktivne (obratno okrevanje).

Vzrok za spremembo poškodbe je lahko njen razpad ali pa reakcija z drugo poškodbo. Od vrste reakcije, ki je odgovorna za spremembo, je odvisen njen časovni razvoj.

V primeru razpada $X \rightarrow Y$ lahko spreminjanje koncentracije poškodbe X po končanem obsevanju opišemo kot proces prvega reda

$$-\frac{dN_Y}{dt} = \frac{dN_X}{dt} = -k_1^Y N_X \ , \tag{9.11}$$

z rešitvijo

$$N_X(t) = N_X^0 e^{-k_1^Y t} \tag{9.12}$$

$$N_Y(t) = N_X^0 (1 - e^{-k_1^Y t}) \ . \tag{9.13}$$

Če pa je za spremembo odgovorna reakcija dveh poškodb, $X_A + X_B \rightarrow Y$, jo lahko opišemo z enačbo

$$-\frac{dN_Y}{dt} = \frac{dN_{X_A}}{dt} = \frac{dN_{X_B}}{dt} = -k_2^Y N_{X_A} N_{X_B} \ . \tag{9.14}$$

V primeru $N_{X_A}^0 > N_{X_B}^0$ je rešitev

$$N_Y(t) = N_{X_B}^0 \frac{1 - e^{-k_2^Y t (N_{X_A}^0 - N_{X_B}^0)}}{1 - (N_{X_B}^0 / N_{X_A}^0) e^{-k_2^Y t (N_{X_A}^0 - N_{X_B}^0)}} \ . \tag{9.15}$$

Če imata obe poškodbi enaki začetni koncentraciji, $N_{X_A}^0 = N_{X_B}^0$, ali pa gre za rekcijo med dvema poškodbama iste vrste, $X_A = X_B$, sledi

$$N_X(t) = \frac{N_X^0}{1 + N_X^0 k_2^Y t} \tag{9.16}$$

$$N_Y(t) = N_X^0 - N_X(T) = N_X^0 (1 - \frac{1}{1 + N_X^0 k_2^Y t}) \ . \tag{9.17}$$

Enačba 9.17 opisuje proces drugega reda. V primeru, da koncentracija ene vrste poškodb mnogo večja od koncentracije druge ($N_{X_A}^0 \gg N_{X_B}^0$), pa lahko časovni razvoj zopet opišemo z enačbo prvega reda kjer velja $k_1^Y = k_2^Y N_{X_A}^0$.

V gornjih enačbah je bila N_X^0 začetna koncentracija poškodb tipa X, k_1^Y in k_2^Y pa reakcijski konstanti za reakcijo prvega oz. drugega reda. Enačbi 9.11 in 9.14 kažeta, da je pri reakcijah prvega reda hitrost reakcije sorazmerna s koncentracijo poškodb, pri procesih drugega reda pa je odvisnost kvadratična.

Zaporni tok Običajno je časovni razvoj zapornega toka opisan z nastavkom

$$I(t) = I(0)[A_0 + \sum_i A_i e^{-t/\tau_i^\alpha}] \ , \tag{9.18}$$

kjer je A_0 prispevek stabilnih poškodb, A_i pa popisujejo poškodbe, ki s časom razpadajo (okrevanje poškodb). Da bi izločili vpliv velikosti vzorca in fluence se namesto toka običajno podaja parameter $\alpha = \frac{I}{V \cdot \Phi_{eq}}$ (en. 9.8). Z njim enačbo 9.18 prepišemo v

$$\alpha(t) = \alpha_0 + \sum_i \alpha_i e^{-t/\tau_i^\alpha} \ . \tag{9.19}$$

Gornji enačbi opisujeta okrevanje in stabilno komponento zaporega toka, saj obratno okrevanje le tega ni bilo opaženo.

Novi rezultati [35] in meritve predstavljene v tem delu pa kažejo, da tudi domnevno stabilna komponenta (α_0) s časom počasi upada. Časovo odvisnost lahko opišemo z logaritemskim nastavkom

$$\alpha(t) = \alpha_E e^{-t/\tau_E^\alpha} - \alpha_L \ln(t/\tau_L^\alpha) \ . \tag{9.20}$$

Zavedati pa se je treba, da logaritemski nastavek nima smiselnega fizikalnega ozadja, ampak je le uporaben opis časovnega razvoja počasne komponente.

Efektivna koncentracija primesi V časovnem razvoju N_{eff} so opazne vse tri prej naštete komponente: časovno stabilne poškodbe, okrevanje in obratno okrevanje (slika 9.5). Tudi pri N_{eff} lahko okrevanje opišemo z vsoto eksponentnih funkcij, kar kaže na reakcije prvega reda, medtem ko dinamika obratnega okrevanja se ni nedvoumno določena. Tako lahko časovni razvoj N_{eff} opišemo z nastavkom

$$N_{eff}(t) = N_C + \sum_i N_i e^{t/\tau_i} + N_Y(t) \ , \tag{9.21}$$

kjer so N_C časovno stabilne poškodbe, N_i poškodbe, odgovorne za okrevanje, τ_i časovne konstante okrevanja in N_Y poškodbe, odgovorne za obratno okrevanje. Glede na vrsto reakcije, časovni potek $N_Y(t)$ popisujejo enačbe 9.13, 9.15 ali 9.17.

Meritve Poglavje o časovnem razvoju sevalnih poškodb vključuje študij razvoja napetosti polnega osiromašenja oziroma efektivne koncentracije primesi (N_{eff}) in študij razvoja zapornega toka. Pri tem sem se ločeno posvetil hitremu okrevanju na časovni skali do nekaj

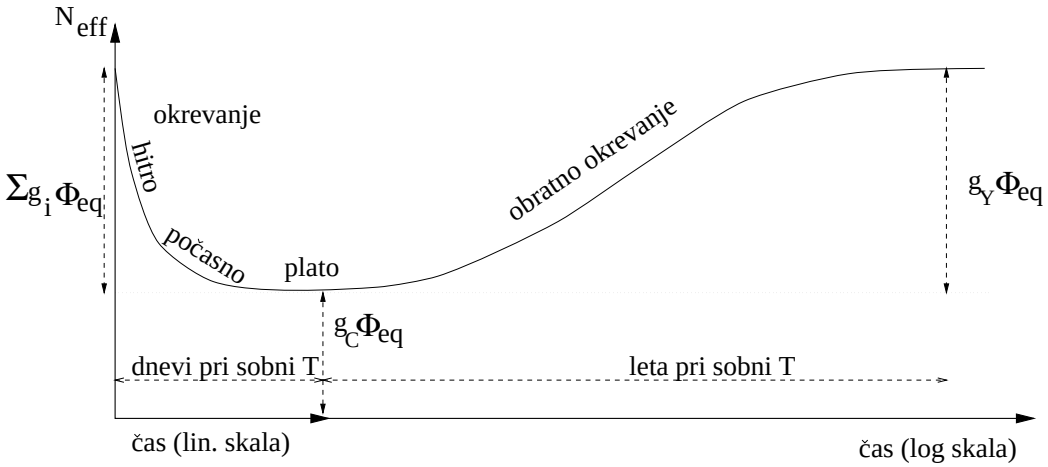

Figure 9.5: Shematski prikaz časovnega razvoja efektivne koncentracije primesi.

dni in počasnenu delu razvoja zapornega toka oziroma obratnemu okrevanju v primeru N_{eff} (časovna skala nekaj mesecev pri 60°C)[50].

Ločeno obravnavanje okrevanja in obratnega okrevanja N_{eff} je možno zato, ker so časovne konstante obeh procesov bistveno različne. Medtem ko je tipični čas okrevanja pri sobni temperaturi nekaj dni, je časovna konstanta obratnega okrevanja približno leto pri sobni temperaturi. Tako je prispevek obratnega okrevanja v času okrevanja zanemarljiv.

9.3.2 Hitro okrevanje N_{eff}

Pri študiju okrevanja N_{eff} sem se posvetil predvsem zelo hitrim komponentam (reda velikosti nekaj ur). Študij le teh namreč zahteva možnost C/V meritev med in takoj po obsevanju, tako da so meritve teh komponent dokaj redke. Analizirane so bile meritve sedmih diod pri temperaturah 0, 5 in 15°C. Meritve hitre komponente so potekale približno teden dni.

Časovni potek razvoja efektivne koncentracije primesi za vzorce B3, I3 in D3 med in po obsevanju je prikazan na sliki 9.6. Zaradi dolgega časa obsevanja (6.5 ur) je prišlo do delnega okrevanja poškodb že med samim obsevanjem, zato odvisnost N_{eff} od fluence oz. časa obsevanja ni linearna. Združen vpliv obsevanja in okrevanja lahko opišemo z

[50] Temperaturna odvisnost reakcijskih konstant je podana z enačbo $k(T) = k_0 e^{-E_a/k_B T}$, kjer je E_a aktivacijska energija. Vrednost E_a za obratno okrevanje N_{eff} v literaturi je 1.3 eV [13, 14, 15] in za počasno okrevanje zapornega toka 1.1 eV [15]. Tako je razvoj N_{eff} pri 60°C približno 500-krat hitrejši kot pri 20°C , za zaporni tok pa je to razmerje približno 190.

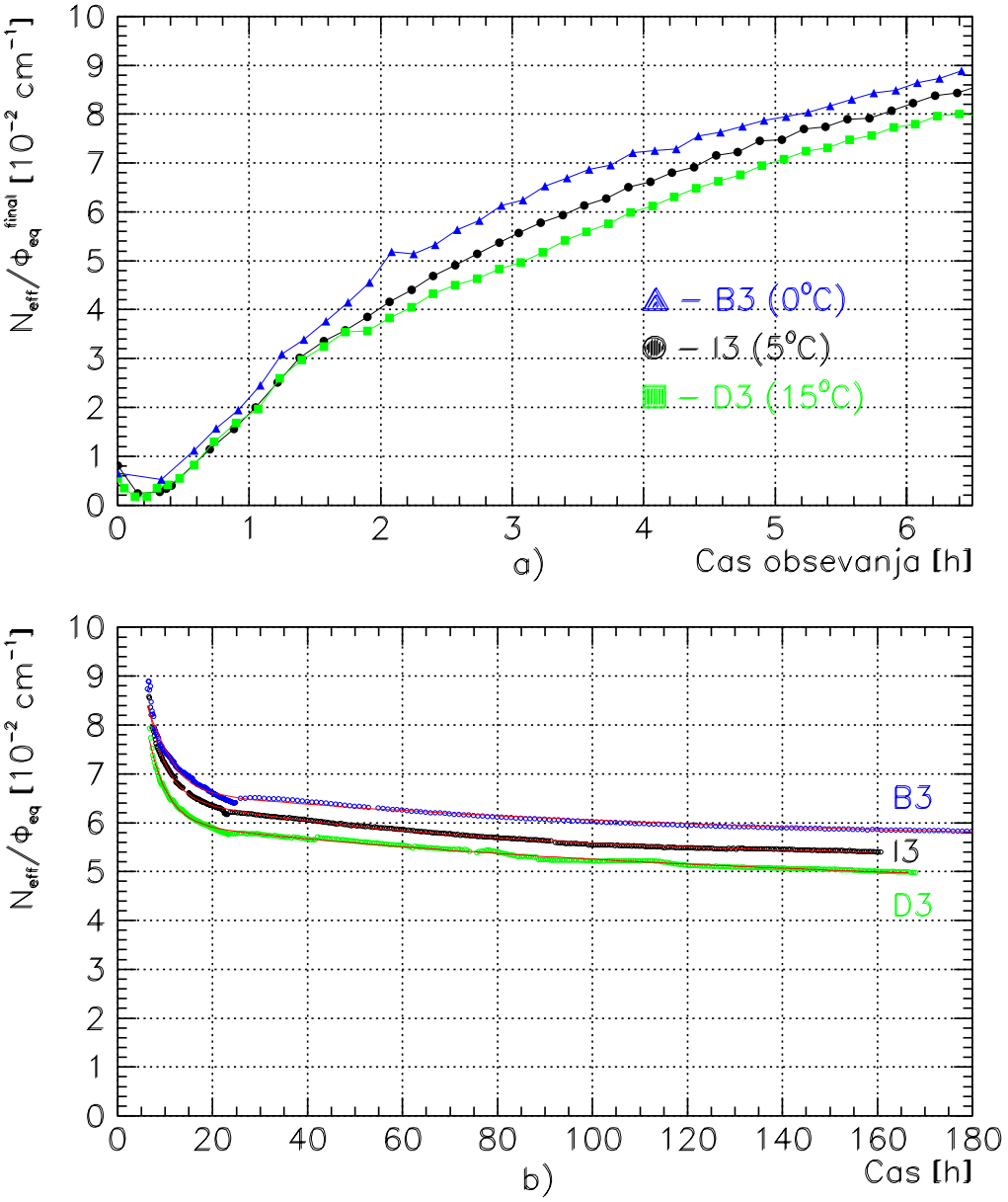

Figure 9.6: Časovni razvoj N_{eff} a) med obsevanjem in b) po obsevanju. Prikazani so vzorci D3, I3 and B3, ki so bili obsevani pod enakimi pogoji z izjemo temperature. Rdeča kkrivulja na sliki b) prikazuje rezultate prilagajanja z nastavkom 9.23.

enačbo

$$N_{eff}(t) = [g_C t + \sum_i g_i \tau_i (1 - e^{-t/\tau_i})] \cdot \phi_{eq} \ ; \ t < t_{irr} \ . \tag{9.22}$$

Vzorec	Φ_{eq} [n/cm^2]	T [°C]	g'_C [10^{-2}cm^{-1}]	g_1 [10^{-2}cm^{-1}]	τ_1 [h]	g_2 [10^{-2}cm^{-1}]	τ_2 [h]
D3	$4.2 \cdot 10^{13}$	15°C	4.3	3.6	4.0	1.7	170
D1	$4.5 \cdot 10^{13}$	15°C	4.5	2.5	3.9	1.3	37
K3	$1.03 \cdot 10^{14}$	5°C	4.3	1.7	9.3	1.1	79
I3	$4.4 \cdot 10^{13}$	5°C	5.1	3.9	3.7	1.3	68
B3	$4.4 \cdot 10^{13}$	0°C	5.5	4.1	4.4	1.1	110
G3	$8.3 \cdot 10^{12}$	0°C	6.4	7.3	3.5	4.3	16
G2	$8.7 \cdot 10^{12}$	0°C	4.3	8.0	3.8	4.9	47

Table 9.1: Rezultati prilagajanja nastavka 9.23 meritvam hitre komponente časovnega razvoja N_{eff}. Ob vsakem vzorcu sta podani še fluenca normalizirana na 1 MeV nevtrone in temperatura obsevanja in shranjevanja.

Vendar pa prilagajanje enačbe 9.22 merjenim vrednostim ni dalo smiselnih rezultatov. To je lahko tako posledica izločanja začetnih primesi kot tudi vpliva napajalne napetosti, ki jo bom obravnaval v podpoglavju 9.5.

Analiza razvoja N_{eff} po obsevanju je pokazala, da lahko njen časovni razvoj v prvem tednu po končanem obsevanju lepo popišemo s konstantnim členom in dvema eksponentoma

$$N_{eff}(t) = [g_0 t_{irr} + \sum_{i=1,2} g_i \tau_i (e^{t_{irr}/\tau_i} - 1) e^{-t/\tau_i}] \cdot \phi_{eq} \ ; \ t_{irr} < \ t \ . \tag{9.23}$$

Rezultati prilagajanja nastavka 9.23 so podani v tabeli 9.1. Medtem ko za vse vzorce dobimo časovno konstanto hitre komponente okoli 4 ure, pa pri ostalih vrednostih ni jasne sistematike. To lahko delno pripišemo relativno kratkemu času merjenja. Bolj pomemben pa je verjetno tedaj še neznan vpliv napajalne napetosti na časovni razvoj poškodb, ki vplivajo na napetost polnega osiromašenja. Tako so pogoste meritve in le delno osiromasenje vzorca vplivali na časovni razvoj.

Iz dobljenih meritev lahko zaključimo, da hitro okrevanje efektivne koncentracije primesi vodi do znatnih sprememb N_{eff} v prvem dnevu po obsevanju in to tudi pri 0°C. Čeprav hitro okrevanje N_{eff} za delovanje eksperimentov na trkalniku LHC ni pomembno, pa je njegov vpliv pomemben pri primerjavi rezultatov, izmerjenih kmalu po obsevanju.

9.3.3 Obratno okrevanje N_{eff}

Analiza obratnega okrevanja je bila usmerjena predvsem v določanje dinamike odgovorne reakcija (prvi ali drugi red). V ta namen sta bili uporabljeni dve metodi. Pri prvi sem

Vzorec	Φ_{eq} [10^{14} n/cm^2]	g_C [10^{-2}cm^{-1}]	k_Y^{lin} [10^{-8}cm^{-1}s^{-1}]
R02B	0.21	0.42	9.1
R02M	0.21	0.57	11.3
R05B	0.53	1.4	13.5
R05M	0.53	1.2	12.0
R10B	1.06	1.4	15.3
R10M	1.06	1.8	14.9
R20B	2.1	1.6	11.1
R20M	2.1	1.6	11.8

Table 9.2: Fluenca in rezultati prilagajanja po enačbi 9.26 za diode, namanjene študiju dinamike obratnega okrevanja.

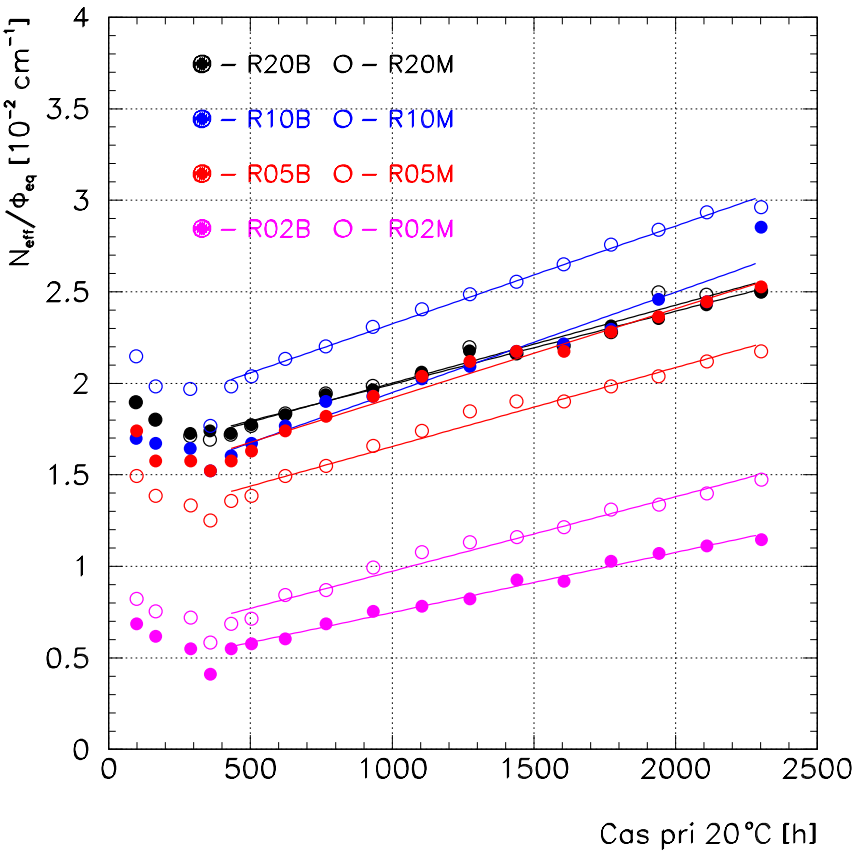

Figure 9.7: Razvoj $Neff/\Phi_{eq}$ v začetni stopnji obratnega okrevanja za diode brez napajalne napetosti pri 20°C.

enačbi za prvi in drugi red prilagajal časovnemu poteku obratnega okrevanja do pozne faze le tega. Pri tem sem opazoval tako ujemanje napovedi z meritvami kot tudi odvisnost od fluence. V primeru procesa prvega reda je namreč hitrost spreminjanja efektivne koncentracija primesi pri obratnem okrevanju sorazmerna s fluenco, v primeru procesa drugega reda pa z njenim kvadratom (enačbi 9.11 in 9.14). Vendar pa meritve vzorcev, hranjenih pod napajalno napetostjo, niso omogočile jasne določitve tipa reakcije. To je bila posledica le delnega osiromašenja vzorcev in vpliva napajalne napetosti na časovni razvoj poškodb, ki bo opisan v podpoglavju 9.5.

Pri drugi metodi sem opazoval le začetni del obratnega okrevanja. Omejil sem se na čase, majhne v primerjavi s časovno konstanto obratnega okrevanja in časovni potek (enačbi 9.13 in 9.17) linearizíral. Tedaj lahko časovni razvoj efektivne koncentracije primesi opišemo z enačbama

$$\frac{N_{eff}(t)}{\Phi_{eq}} = g_C + g_Y k_1^Y t \tag{9.24}$$

za prvi red in

$$\frac{N_{eff}(t)}{\Phi_{eq}} = g_C + g_Y^2 \Phi_{eq} k_2^Y t \tag{9.25}$$

za proces drugega reda. Tu sta g_C hitrost tvorbe stabilnih poškodb, g_Y pa hitrost tvorbe poškodb, odgovornih za obratno okrevanje. Enačbi lahko posplošimo v obliko

$$\frac{N_{eff}(t)}{\Phi_{eq}} = g_C + k_Y^{lin} t \ , \tag{9.26}$$

kjer je k_Y^{lin} za reakcije prvega reda neodvisen od fluence ($g_Y k_1^Y$), za reakcije drugega reda pa sorazmeren s fluenco ($g_Y^2 k_2^Y \Phi_{eq}$). Tako lahko z meritvami odvisnosti parametra k_Y^{lin} od fluence določimo tip reakcije.

Tudi po tej metodi analiza vzorcev, hranjenih pod zaporno napetostjo, ni dala nedvoumnih rezultatov, kar je posledica že omenjenega vpliva napajalne napetosti na razvoj poškodb. Zato je bila tej študiji namenjena posebna skupina diod (skupina RAN). Ta je bila sestavljena iz štirih parov, obsevanih do štirih različnih fluenc (tabela 4.6). Vseh 8 diod je bilo obsevanih in hranjenih brez napajalne napetosti pri 20°C. Da bi se izognili vplivu neznanih parametrov, so bile diode ves čas hranjene pod enakimi pogoji.

Meritve obratnega okrevanja RAN diod so prikazane na sliki 9.7, rezultati prilagajanja nastavka 9.26 pa v tabeli 9.2. Iz prikazanih rezultatov je razvidno, da hitrost naraščanja N_{eff}/Φ_{eq} ni odvisna od fluence. To kaže, da vsaj v začetni fazi, ki je pomembna za delovanje detektorjev v načrtovanih eksperimentih, obratno okrevanje dobro popišemo zreakcijo prvega reda.

9.3.4 Okrevanje zapornega toka

Hitro okrevanje zapornega toka nekaterih diod iz tabele 9.1 je prikazano na sliki 9.8. Zaradi visokega sevalnega ozadja meritve zapornega toka med obsevanjem niso uporabne. Časovni razvoj v začetni fazi po obsevanju pa lahko, tako kot okrevanje efektivne koncentracije primesi, lepo popišemo z nastavkom

$$\alpha(t) = [\alpha_0 t + \sum_{i=1,2} \alpha_i \tau_i (e^{t_{irr}/\tau_i^\alpha} - 1) e^{-t/\tau_i^\alpha}] \cdot \phi_{eq} \ ; \ t_{irr} < \ t \ . \tag{9.27}$$

Kot pri razvoju N_{eff}, tudi tu rezultati prilagajanja ne kažejo sistematičnega obnašanja. Pomanjkanje sistematike in razlike med vzorci lahko razložimo s prispevki površinskih tokov, visokim sevalnim ozadjem in dolgimi merilnimi kabli. Pomembna pa je ugotovitev, da je tudi pri 0°C opazno znatno okrevanje zapornega toka že v prvem dnevu po obsevanju. Meritve v laboratoriju po ekvivalentu nekaj tednov pri 20°C (ure pri 60°C) in pri ugodnjejših merilnih pogojih pa kažejo, da imajo tokovi vseh diod z delujočimi zaščitnimi obroči enake vrednosti (slika 9.9).

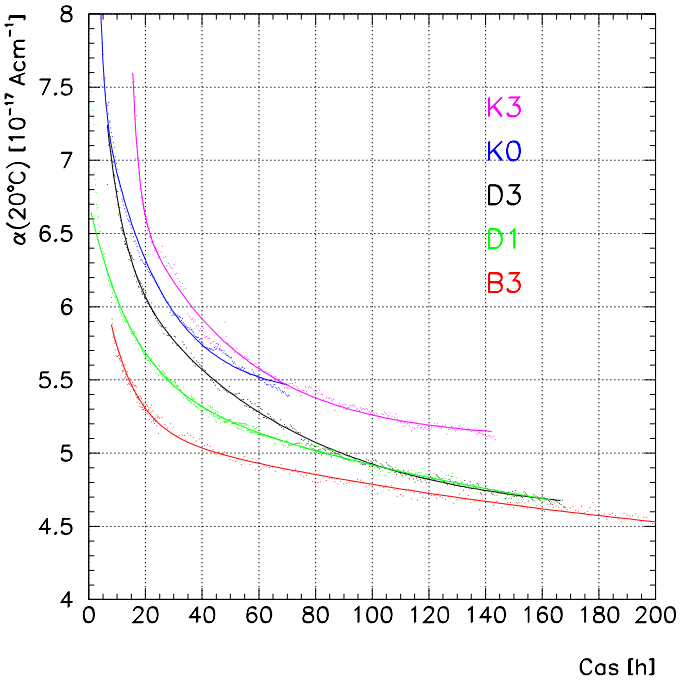

Figure 9.8: Hitro okrevanje zapornega toka. Vrednosti parametra α so normalizirane na 20°C po enačbi $j(T_2) = j(T_1) \left(\frac{T_2}{T_1}\right)^2 e^{-\frac{E'_g}{2k_B}(T_2^{-1} - T_1^{-1})}$. Za E'_g je bila uporabljena vrednost 1.2 eV [14]. Opozoriti velja, da se na sliki ordinatna os ne začne pri ničli.

Za študij razvoja počasnih komponent zapornega toka je bil razvoj poškodb pospešen s segrevanjem vzorcev na 60°C. Medtem ko je v prvih desetih urah še opazen znaten

prispevek eksponentno razpadajoče komponente (enačba 9.27), pa je pri daljših časih segrevanja upadanje zapornega toka linearno v semilogaritemski skali (slika 9.9). Ta kaže na efektivno logaritemsko časovno odvisnost, tako da smo rezultate skušali popisati z nastavkom

$$\alpha(t) = \alpha_E e^{-t/\tau_E^\alpha} - \alpha_L \ln(t/\tau_L^\alpha) \ . \tag{9.28}$$

Primerjava rezultatov prilagajanja z merjenimi vrednostmi (slika 9.9) kaže dobro ujemanje meritev z rezultati prilagajanja nastavka 9.28. Vrednosti parametrov po prilagajanju so podane v tabeli 9.3. O enakih meritvah počasnih komponent poroča tudi [35], s sledečimi vrednostmi parametrov: $\alpha_E = (1.01 \pm 0.38) \cdot 10^{-17}$ A/cm, $\tau_E = 93 \pm 24$ min, $\alpha_L = (5.03 \pm 0.09) \cdot 10^{-17}$ A/cm in $\tau_L \approx 6.6^{+45}_{-4.6}$ let. Razen časovnih konstant logaritemske komponente se vrednosti iz [35] dobro ujemajo z vrednostmi iz tabele 9.3. Potrebne pa so nadaljne raziskave, ki bi razkrile fizikalno ozadje logaritemske komponente.

Sample	Φ_{eq} [n/cm^2]	α_E [10^{-17}A/cm]	τ_E^α (60°C) [h]	α_L [10^{-17}A/cm]	τ_L^α (60°C) [leta]
K3	$1.03 \cdot 10^{14}$	1.4	0.7	0.32	2.
K0	$1.04 \cdot 10^{14}$	1.1	1.8	0.26	6.
I3	$4.4 \cdot 10^{13}$	1.3	1.8	0.26	14.
B3	$4.4 \cdot 10^{13}$	1.4	1.3	0.29	8.
G3	$8.3 \cdot 10^{12}$	1.2	1.6	0.28	9.
G2	$8.7 \cdot 10^{12}$	1.2	1.9	0.24	12.
U3A	$4.1 \cdot 10^{13}$	1.2	2.1	0.31	2.
U3B	$4.1 \cdot 10^{13}$	1.2	2.1	0.32	3.

Table 9.3: Časovni razvoj počasnih komponent zapornega toka. V tabeli je navedena fluenca in rezultati prilagajanja po enačbi 9.28. Vrednosti parametra α so normalizirane na 20°C. Napake na α_L, α_E in τ_E^α so okoli 20% in na τ_L^α okoli 50%.

9.4 Vpliv fluksa nevtronov

Medtem ko bo obsevanje detektorjev v novih eksperimentih zelo počasen proces[51], je tipičen čas obsevanja vzorcev za študij sevalnih poškodb nekaj ur. Zato je bilo potrebno preveriti, kako hitrost obsevanja z nevtroni vpliva na tvorbo poškodb. O vplivu hitrosti obsevanja pri ionski implantaciji poroča [52], medtem ko za nevtrone ti podatki niso bili znani. Rezultati [52] za obsevanje z Br, Si in C kažejo znatno upadanje hitrosti tvorbe

[51] Ekvivalentna fluenca 1 MeV nevtronov reda 10^{14} n/cm^2 bo dosežena v desetih letih obsevanja, čemur ustreza ekvivalenten fluks 10^6 n/cm^{2}s.

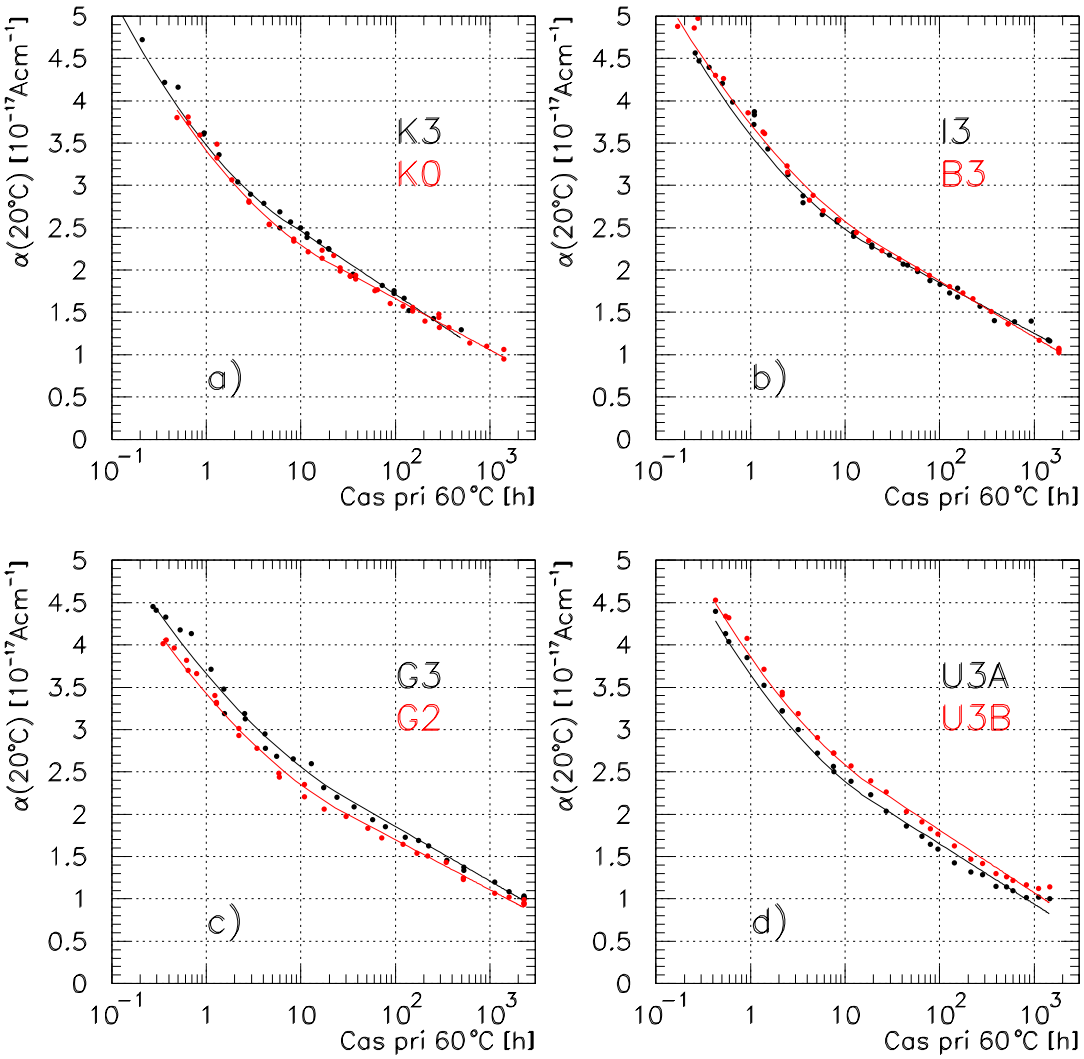

Figure 9.9: Časovni razvoj počasnih komponent zapornega toka. V tabeli so navedeni pogoji obsevanja in rezultati prilagajanja po enačbi 9.28. Vrednosti parametra α so normalizirane na 20°C.

poškodb pri ionskih fluksih nad 10^7 cm^{-2}s^{-1}, 10^8 cm^{-2}s^{-1} in nekajkrat 10^8 cm^{-2}s^{-1}. Opazno je upadanje mejnega fluksa z naraščajočo maso, tako da lahko za nevtrone pričakujemo mejo nad 10^9 n/cm^{2}s.

Za študij vpliva nevtronskega fluksa je bilo uporabljenih sedem vzorcev, obsevanih s fluksi od $2 \cdot 10^8$ do približno $5 \cdot 10^{15}$ n/cm^{2}s (tabela 9.4). Razvoj efektivne koncentracije primesi (slika 9.10) in zapornega toka (slika 9.11) pri 60°C ni kazal sistematskih razlik, ki

bi jih lahko povezali z hitrostjo obsevanja. Na osnovi teh rezultatov lahko domnevamo, da je varna ekstrapolacija sevalnih poškodb z razpoložljivih nevtronskih izvorov na pogoje v eksperimentih na LHC.

Vzorec	ϕ_{eq} [n/cm^{2}s]	Φ_{eq} [n/cm^2]
SA1	$2.2 \cdot 10^8$	$1.3 \cdot 10^{14}$
SA2	$2.2 \cdot 10^8$	$1.3 \cdot 10^{14}$
K3	$1.9 \cdot 10^9$	$1. \cdot 10^{14}$
K1	$3.7 \cdot 10^{11}$	$1. \cdot 10^{14}$
K0	$1.6 \cdot 10^{12}$	$1. \cdot 10^{14}$
P0A	$\approx 5 \cdot 10^{15}$	$1.1 \cdot 10^{14}$
P0B	$\approx 5 \cdot 10^{15}$	$1.1 \cdot 10^{14}$

Table 9.4: Seznam diod uporabljenih za študij vpliva nevtronskega fluksa in pogoji obsevanja.

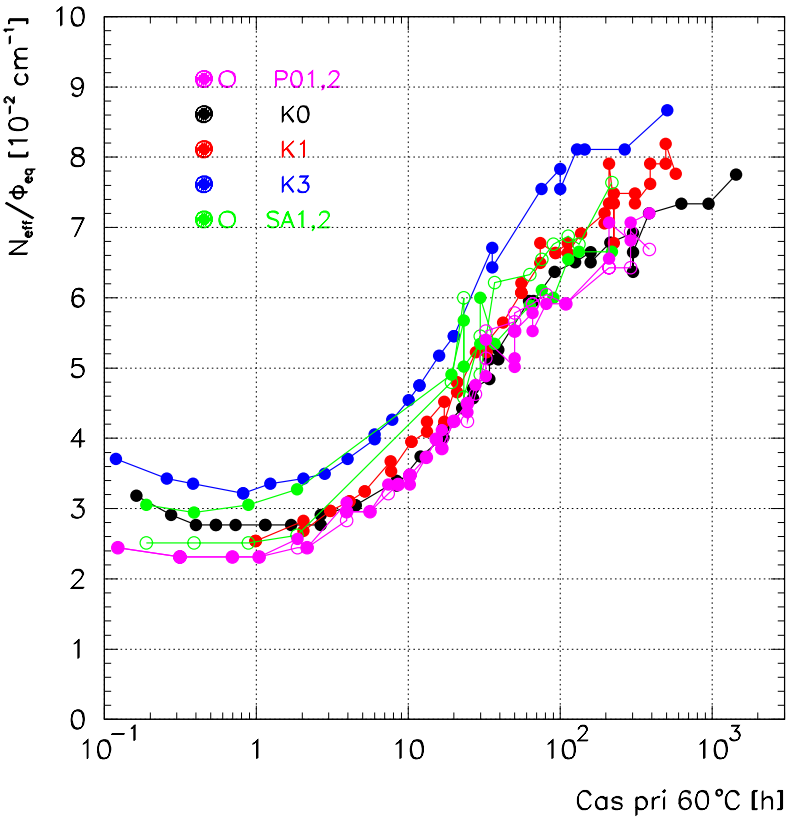

Figure 9.10: Časovni razvoj efektivne koncentracije primesi pri 60°C za diode, obsevane z različnimi fluksi nevtronov.

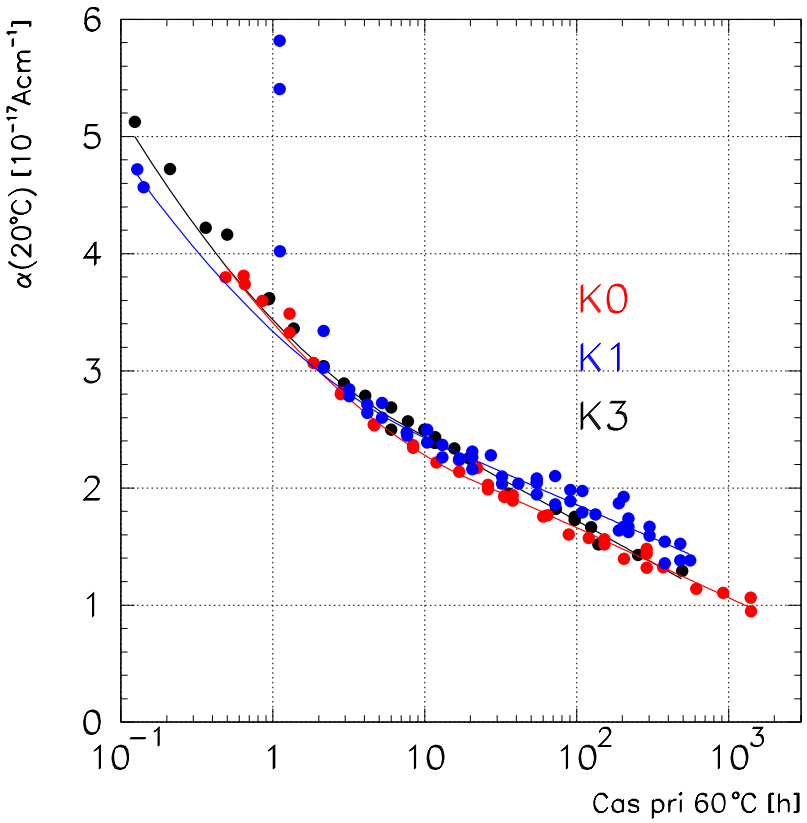

Figure 9.11: Časovni razvoj zapornega toka pri 60° C za diode, obsevane z različnimi fluksi nevtronov. Vrednosti parametra α so normalizirane na 20° C.

9.5 Vpliv napajalne napetosti

Do nedavnega je veljalo splošno prepričanje, da je nastanek in razvoj sevalnih poškodb neodvisen od napajalne napetosti. Natančen nadzor nad pogoji obsevanja in shranjevanja v okviru meritev tega dela, ki je vključeval tudi napajalno napetost, pa je pokazal nasprotne rezultate. Vzorci s polno napajalno napetostjo kažejo po končanem okrevanju približno za faktor 2 večjo efektivno koncentracijo primesi od tistih brez napetosti (slika 9.12).

Izvor razlike v N_{eff} med vzorci z in brez zaporne napetosti je lhako v tvorbi poškodb ali pa v njihovem časovnem izvoru. Da bi ločili med tema dvema možnostima, smo primerjali štiri diode, obsevane in hranjene pod različnimi pogoji napajanja. Prva (D2A) je bila pod napetostjo tako med kot po obsevanju, druga (S3A) je bila med obsevanjem pod napetostjo, po njem pa ne, tretja (S3B) med obsevanjem ni bila pod napetostjo, po

njem pa in zadnje (D2B) ni bila pod napetostjo ne med ne po obsevanju. Primerjava okrevanja vseh štirih vzorcev (slika 9.13) je za vzorca S3A in D2B (oba brez napetosti po obsevanju) dala enako N_{eff} po končanem okrevanju, medtem ko imata vzorca S3B in D2A višjo N_{eff}. Razliko med vzorcema S3B in D2A lahko pripišemo okrevanju med obsevanjem (6.5 ure brez zaporne napetosti za vzorec S3B). Iz predstavljenih rezultatov lahko sklepamo, da razlika med vzorci nastane med okrevanjem, torej, da zaporna napetost ne vpliva na nastajanje ampak na okrevanje poškodb.

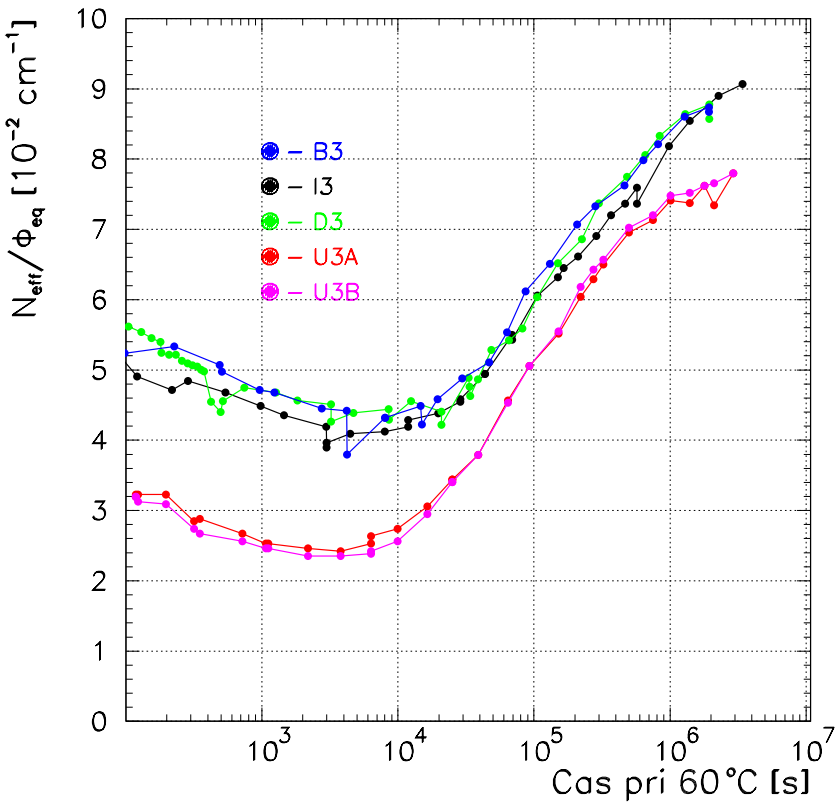

Figure 9.12: Primerjava časovnega razvoja efektivne koncentracije primesi za vzorce z (B3, D3, I3) in brez napajalne napetosti (U3A, U3B). Razen napajalne napetosti so bili vzorci hranjeni pod enakimi pogoji.

Za vpliv odkritega pojava na delovanje silicijevih detektorjev v bodočih eksperimentih pa je pomembno tudi obnašanje nastale razlike po izklopu napajalne napetosti. Kot je razvidno s slike 9.14, po izklopu napajalne napetosti razlika upada. Upadanje lahko dobro popišemo s hitrim padcem ob izklopu (okoli 10% razlike) in vsoto dveh eksponentnih

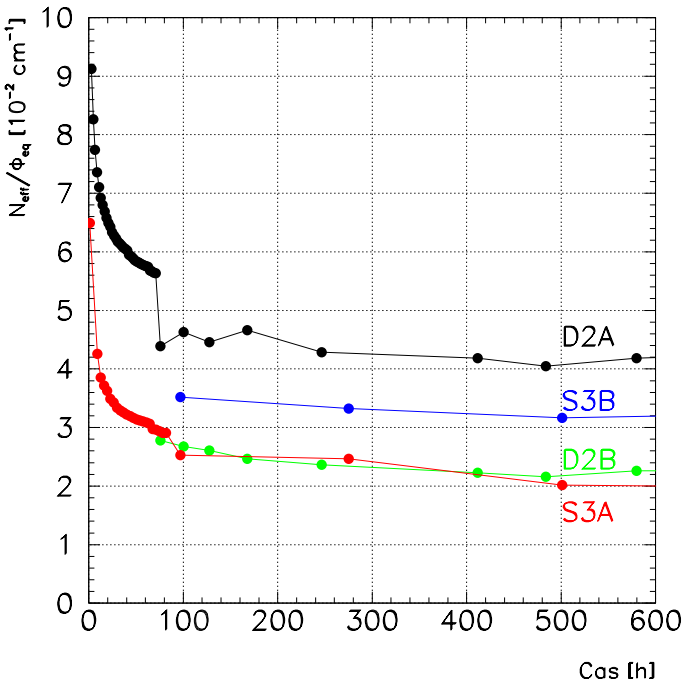

Figure 9.13: Primerjava vrednosti N_{eff}/Φ_{eq} za vzorce z različnimi pogoji napajanja. Vzorec D2A je bil pod napetostjo med in po obsevanjem, vzorec S3B le po obsevanju (6.5 ure), vzorec S3A le med obsevanjem in vzorec D2B ne med ne po obsevanju.

funkcij

$$\frac{N_{eff}(t)}{N_{eff}(t_0)} = C_1 e^{-\frac{t-t_0}{\tau_1}} + C_2 e^{-\frac{t-t_0}{\tau_2}} \ . \tag{9.29}$$

Da bi določili vpliv temperature, smo upadanje razlike opazovali na treh vzorcih pri različnih temperaturah in sicer pri -7°C, 5°C in 20°C. Časovni razvoj razlike smo prilagajali z nastavkom 9.29, rezultati prilagajanja pa so podani v tabeli 9.5. Iz izmerjenih vrednosti smo ocenili aktivacijsko energijo obeh komponent na 0.5 ± 0.15 eV.

T [°C]	C_1	τ_1 [h]	C_2	τ_2 [h]
-7	0.20±0.04	220±20	0.71±0.05	9000±1500
5	0.22±0.04	60±5	0.65±0.05	2100±200
20	0.44±0.04	42±10	0.41±0.05	1050±100

Table 9.5: Rezultati prilagajanja nastavka 9.29 upadanju razlike med vzorcema z in brez napajalne napetosti.

Meritve so pokazale, da ob ponovnem priklopu napajalne napetosti efektivna koncentracija naboja zopet narašča (slika 9.14). Tovrstno obnašanje kaže, da je vsaj del

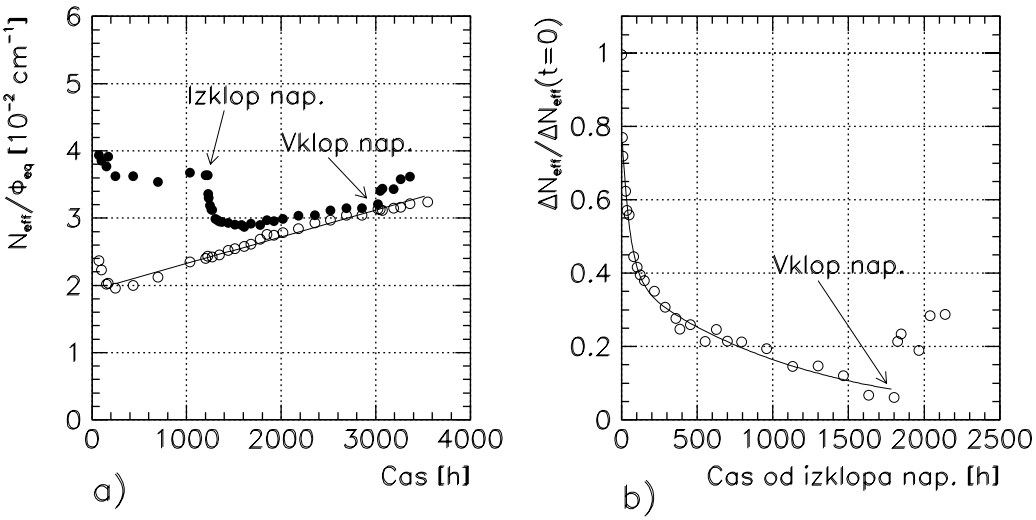

Figure 9.14: a) Časovni razvoj N_{eff} za diodo z (polni krogci) in brez (prazni krogci) napajalne napetosti. Razen napajalne napetosti sta bili diodi obsevani in hranjeni pod enakimi pogoji pri temperaturi 20°C. b) Časovni razvoj razlike v N_{eff} po izklopu napajalne napetosti. Razlika je normalizirana na vrednost tik pred izklopom. Upadanje razlike lahko lepo popišemo z dvema eksponentnima funkcijama (polna črta).

odgovornih poškodb bistabilen, oziroma da reakcija, ki pretvarja aktivno stanje v neaktivno, poteka v obe smeri.

Predstavljeno odkritje ima lahko pomembne posledice za delovanje silicijevih detektorjev v bodočih eksperimentih z visoko luminoznostjo. Medtem ko morajo biti v času zbiranja podatkov (približno 4 mesece letno) detektorji pod napetostjo pa to v preostalem času ni potrebno. Zato je pomembo, da bo v tem času temperatura detektorjev izbrana tako, da bo doseženo optimalno razmerje med upadanjem N_{eff} po izklopu napetosti in obratnim okrevanjem.

Primerjava zapornega toka diod pod napajalno napetostjo in brez nje ni pokazala nobenih sistematskih razlik. Tako zaključujemo, da vpliv napajalne napetosti omejen na poškodbe, ki vplivajo na efektivno koncentracijo primesi.

9.6 Zaključek

Delo predstavlja študijo sevalnih poškodb silicijevih detektorjev pod kontroliranimi pogoji. Za obsevanje z nevtroni sta bili prilagojeni dve obsevalni mesti na reaktorju TRIGA Instituta Jožef Stefan. Tako sta bila nadzorovana temperatura in napajalna napetost, razvoj poškodb pa je bil spremljan tako med kot tudi po obsevanju.

Del doktorskega dela je bil posvečen časovnemu razvoju efektivne koncentracije primesi in zapornega toka. Hitre komponente so bile izmerjene pri temperatirah med 0 in 15°C, pri čemer je bilo opaženo znatno okrevanje v prvih dneh že pri 0°C. Razvoj počasnih komponent je bil pospešen z gretjem vzorcev na 60°C. Pri tem so bili dobljeni jasni dokazi, da lahko obratno okrevanje N_{eff} vsaj v začetni fazi opišemo z reakcijo prvega reda.

Meritve zapornega toka so pokazale, da v nekaj mesecih pri 60°C (ekvivalent približno 50 let pri 20°C) ni prišlo do nasičenja le-tega. Časovni razvoj lahko popišemo z efektivnim nastavkom

$$\alpha(t) = \alpha_E e^{-t/\tau_E^\alpha} - \alpha_L \ln(t/\tau_L^\alpha) \ . \tag{9.30}$$

Pri tem za logaritemski člen, ki nastopa v nastavku, ni znanega fizikalnega ozadja.

Primerjava vzorcev, obsevanih z nevtronskimi fluksi od nekajkrat 10^8 n/cm^{2}s do nekajkrat 10^{15} n/cm^{2}s ni pokazala vpliva hitrosti obsevanja ne na efektivno koncentracijo primesi ne na zaporni tok. Tako domnevamo, da lahko rezultate, dobljene z razpoložljivimi nevtronskimi izvori, ekstrapoliramo na flukse v detektorjih na trkalniku LHC.

Natančen nadzor nad napajalno napetostjo med in po obsevanju je vodil do odkritja vpliva le-te na razvoj efektivne koncentracije primesi. Tako imajo vzorci, hranjeni pod napetostjo polnega osiromašenja, po končanem okrevanju dvakrat večjo efektivno koncentracijo primesi kot vzorci, hranjeni brez napetosti. Ob izklopu napajalne napetosti se razlika počasi zmanjšuje, vendar se je ob ponovnem vklopu vsaj del ponovno vzpostavi. Da bi lahko natančneje ocenili posledice tega pojava za eksperimente na trkalniku LHC, so potrebne še natančnejše raziskave.

Primerjava vrednost nekaterih parametrov, izmerjenih v predstavljenem delu, z rezultati drugih skupin je predstavljena v tabelah 9.6 do 9.9. Primerjave kažejo dobro ujemanje vseh parametrov za vzorce brez napajalne napetosti, medtem ko za vzorce pod napetostjo vrednosti bistveno odstopajo. Ti rezultati se ujemajo z odkritim vplivom napajalne napetosti na časovni razvoj poškodb (podpoglavje 9.5).

Parameter	nap.	ni nap.	globalni	Bates
g_C $[10^{-2}\mathrm{cm}^{-1}]$	4.0±0.6	2.2±0.4	1.77±0.07	2.5±0.3
g_Y $[10^{-2}\mathrm{cm}^{-1}]$	5.4±0.8	5.6±0.9	4.6±0.3	5.9±0.3
$k_2^Y(60°)$ $[10^{-18}\mathrm{cm}^3/\mathrm{s}]$	2.2±0.4	4.6±0.1	7.5^{+15}_{-2}	/

Table 9.6: Primerjava parametrov obratnega okrevanja, dobljenih s prilagajanjem časovnega poteka za proces drugega reda (enačba 9.17, $N_X = g_X \Phi_{eq}$). Navedene so vrednosti za vzorce pod napetostjo (B3, D3 in I3, 200 V), brez napetosti (U3A in U3B), vrednosti iz globalnega pregleda [15] in rezultati S.J. Bates-a et [21]. Zaradi delnega osiromašenja ob koncu obratnega okrevanja sta vrednosti za g_Y in k_2^Y za vzorce pod napetostjo vprašljivi. Podana napaka na naših vrednostih vključuje 15% sistematsko napako dozimetrije.

Parameter	nap.	ni nap.	Ziock
g_C $[10^{-2}\mathrm{cm}^{-1}]$	4.1±0.6	2.3±0.4	2.1
g_Y $[10^{-2}\mathrm{cm}^{-1}]$	4.7±0.7	4.9±0.7	7.5
$k_1^Y(60°)$ $[10^{-6}\mathrm{s}^{-1}]$	3.9±0.6	8.2±0.3	12

Table 9.7: Primerjava parametrov obratnega okrevanja, dobljenih s prilagajanjem časovnega poteka za proces prvega reda (enačba 9.17, $N_X = g_X \Phi_{eq}$). Navedene so vrednosti za vzorce pod napetostjo (B3, D3 in I3, 200 V), brez napetosti (U3A in U3B), in vrednosti dobljene z Ziockovo parametrizacijo [45]. Zaradi delnega osiromašenja ob koncu obratnega okrevanja sta vrednosti za g_Y in k_2^Y za vzorce pod napetostjo vprašljivi. Podana napaka na naših vrednostih vključuje 15% sistematsko napako dozimetrije. Za normalizacijo podatkov v [45] (podani za protone s kinetično energijo 647 in 800 MeV) na 1 MeV protone je bil uporabljen normalizacijski faktor 0.72 [57]. Napake na Ziockovih parametrih v [45] niso podani.

Parameter	ni nap.	nap.	Ziock	ROSE
$k_Y^{lin}(20°\mathrm{C})$ $[10^{-10}\mathrm{cm}^{-1}\mathrm{s}^{-1}]$	/	12±3	5.6	12±9
$k_Y^{lin}(60°\mathrm{C})$ $[10^{-7}\mathrm{cm}^{-1}\mathrm{s}^{-1}]$	2.2±0.5	3.3±0.5	2.5	6±4.5

Table 9.8: Primerjava strmine obratnega okrevanja v začetni fazi k_Y^{lin} (enačba 9.26). Primerjane so vrednosti za vzorce pod napetostjo (B3, D3 in I3, 200 V) in brez napetosti (U3A in U3B), vrednost dobljena iz Ziockove parametrizacije [45] in iz parametrov iz ROSE poročila [13], kombinirani z $g_Y = (4.6 \pm 0.3) \cdot 10^{-2}\mathrm{cm}^{-1}$ is globalnega pregleda (tabela 9.6). Kot v tabeli 9.7 so bile Ziockove vrednosti normalizirane s faktorjem 0.72.

	α_E [10^{-17}A/cm]	τ_E^α [h]	α_L [10^{-17}A/cm]	τ_L^α [years]
to delo	1.25± 0.3	1.7± 0.6	0.29± 0.08	7± 6
Moll	1.01± 0.38	1.5± 0.4	0.33± 0.026	$6.6^{+45}_{-4.6}$

Table 9.9: Primerjava parametrov počasnega okrevanja zapornega toka (enačba 9.30) z vrednostmi skupine M. Molla [35]. Podana napaka na naših vrednostih vključuje 15% sistematsko napako dozimetrije.

10

Appendix: List of Symbols and Abbreviations

A	atomic number
C	depletion layer capacitance
$D(E)$	damage function
$D_n(E)$	neutron damage function
E_C	energy at bottom of conduction band
E_F	Fermi level
E_F^T	quasi Fermi level for a trap in the SCR
E_T	energy of a trap level
E_V	energy at top of valence band
E_a	activation energy
E_g	energy gap $E_C - E_V$
E_i	intrinsic Fermi level
ΔE_C	$E_C - E_T$
ΔE_V	$E_T - E_V$
I	electrical current
J_h	total current of holes
J_e	total current of electrons
J_h^{gen}	generation current of holes
J_h^{rec}	recombination current of holes
L_e	electron diffusion lenght
L_h	hole diffusion lenght
N_A	acceptor concentration
N_A^0	initial acceptor concentration
N_{Av}	Avogadro number
N_C	density of states in the conduction band
N_D	donor concentration
N_D^0	initial donor concentration
N_{eff}	effective dopant concentration

N_{Si}	concentration of Si atoms in the crystal
N_T	concentration of traps T
N_V	density of states in the valence band
N_X	concentration of defect X
N_X^0	initial concentration of defect X
Q	charge
S	sample area
R_P	phosphorus introduction rate
T	temperature
V	voltage
V_{FD}	full depletion voltage
V_{bi}	built-in voltage
W	detector thickness

c_A	acceptor removal constant
c_D	donor removal constant
e_0	electron charge magnitude
e_e	emission probability for electrons from a trap
e_h	emission probability for holes from a trap
f_T	probability for a trap to be occupied
g	defect generation rate
g_C	generation rate of stable defects
g_Y	generation rate of defects responsible for reverse annealing
h	Planck constant
j_{dif}	diffusion current
j_{sat}	saturation current
j_{SCR}	generation current density in SCR
k_B	Boltzmann constant
k_1^Y	first order reaction constant
k_2^Y	second order reaction constant
k_Y^{lin}	slope of reverse annealing at initial stage
m_e^*	effective mass of electrons
m_h^*	effective mass of holes
n	concentration of electrons in the conduction band
n_i	intrinsic carrier concentration
n_{p0}	equilibrium electron density on p side
n_T	concentration of occupied traps
p	concentration of holes in the valence band
p_{n0}	equilibrium hole density on n side
r_c^e	electron capture rate by a trap
r_c^h	hole capture rate by a trap
r^{pair}	electron-hole pair creation rate

v_e	electron thermal velocity
v_h	hole thermal velocity
x_n	depth of the depleted region on n side
x_p	depth of the depleted region on p side
w	total depth of the depleted region
α	leakage current damage constant
ϵ_{Si}	dielectric constant od silicon
κ	hardness factor
ρ	specific resistivity
ρ_e	charge density
ρ_{Si}	density of silicon
σ_e	electron capture cross-section of a trap
σ_h	hole capture cross-section of a trap
σ_γ	radiative capture cross-section
τ_e	electron lifetime
τ_h	hole lifetime
τ_i	N_{eff} annealing time constants
τ_i^α	reverse current annealing time constants
τ_e^{tr}	electron trapping time constant
τ_h^{tr}	hole trapping time constant
ϕ	flux
Φ	fluence
Φ_{eq}	equivalent fluence
FDV	full depletion voltage
SCR	space charge region
C/V	capacitance vs. voltage
I/V	current vs. voltage
NIEL	non-ionising energy loss

References

[1] J. Straver et al., Nucl. Instr. Meth. **A348** (1994) 485.

[2] The LHC Conceptual Design Report - The Yellow Book, CERN/AC/95-05 (LHC) (1995).

[3] ATLAS Letter of Intent for a General Purpose pp Experiment at the Large Hadron Collider at CERN, CERN/LHCC/92-4, LHCC/I2 (1992).

[4] ATLAS Technical Proposal for a General Purpose pp Experiment at the Large Hadron Collider at CERN, CERN/LHCC/94-43, LHCC/P2 (1994).

[5] CMS Technical Proposal, CERN/LHCC/94-38, LHCC/P1 (1994).

[6] ATLAS Inner Detector Technical Design Report, CERN/LHCC/97-16, ATLAS TDR 4, (1997).

[7] G. Gorfine et al., ATLAS Internal Note INDET-NO-030, UM-P-93/103 (1993).

[8] S.M. Sze: *Physics of Semiconductor Devices*, John Wiley & Sons (1981).

[9] A. Peisert: *Silicon Microstrip Detectors* (1992)

[10] N.A. Ashcroft, N.D. Mermin: *Solid State Physics*, Holt, Rinehard and Winston (1976).

[11] W. Shockley et al., Phy. Rev. **87** (1952) 835.

[12] G. Hall, IC/HEP/96-1 (1996).

[13] V. Angelli et al., (ROSE Collab.): *RD48 StatusReport*, CERN/LHCC 97-39, June 1997.

[14] T. Schulz: *Investigation on the Long term Behaviour of Damage Effects and Corresponding Defects in Detector Grade Silifon after Neutron Irradiation*, Ph.D. Thesis, DESY 96-027 (1995).

[15] A. Chilingarov et al., Nucl. Instr. Meth. **A 360** (1995) 432.

[16] L. Beattie et al., ROSE Technical Note 97/4 (1997).

[17] A. Chilingarov et al, 3^{rd} ROSE Workshop on Radiaton Hardening of Silicon Detectors, DESY-PROCEEDINGS-1998-02 (1998).

[18] A. Chilingarov et al., Nucl. Instr. Meth. **A 360** (1995) 432.

[19] R. Wunsdorf, *Systematische Untersuchungen zur Strahelenresitenz von Silizium-Detektoren für die Verwendung in Hochenergiephysik-Experimenten*, Ph.D. thesis, DESY FHIK-92-01 (1992).

[20] H. Feick: *Radiation Tolerance of Silicon Particle detectors for High-Energy Physics Experiments*, Ph.D. Thesis, DESY F35D-97-08 (1997).

[21] S.J. Bates et al., CERN-ECP/95-26 (1995).

[22] P.A. Aarnio et al., Nucl. Instr. Meth. **A360** (1995) 521,
Rogalla, M. et al.:*Radiation damage to neutron and proton irradiated GaAs particle detectors*, (1997) to be published in Nucl. Instr. Meth.,
K. Riechmann et al., Nucl. Instr. Meth **A377** (1996) 276,
S.J. Bates et al., CERN-ECP/95-03 (1995),
J.A.J. Matthews, ATLAS Internal note INDET-NO-118 (1995),
M. Huhtinen et al., Nucl. Instr. Meth **A335** (1993) 580,
A. Van Ginneken, FN-522 (1989).

[23] B.R. Gossick, Journal of Applied Physics 30 (1959) 6.
L.S. Smirnov *A Survey of Semiconductor Radiation Techniques*, Mir Publishers, Moscow, 1983.

[24] G. Kinchin et al., Rep. Prog. Phys. Vol. 18., (1959).

[25] M.S.Lazo et al.: *Silicon and silicon dioxide neutron damage functions*, Proc. Fast Burt. React. Workshop, Sandia National Laboratories 1987, SAND-87-009 8 Vol.1 85-103.

[26] Annual Book of ASTM Standards, Vol 12.02, chapter ASTM E722-85, pages 324-329. ASTM Commitee E-10 on Nuclear Technology and Application, May 1985.

[27] A.M. Ougang et al.: *Differential displacement kerma cross sections for neutron interactions in Si and GaAs*, IEEE Transactions on Nuclear Science, NS-37 (1990) 2219-2228.

[28] K. Hill et al., CERN-PPE/97-11 (1997).

[29] R. Wunstorf et al., Nucl. Instr. Meth. **A 377** (1996) 228.

[30] S.J. Bates et al.: *Proton Irradiation of Silicon Detectors with Different Resistivities*, Fourth International Workshop on Vertex Detectors, Ein Gedi 1995, WIS-96/18/June-PH (1996).

[31] J. Matheson et al., RD 20 Techincal Report RD20/TN/36 (1995).

[32] B. Dezillie et al., 3^{rd} ROSE Workshop on Radiaton Hardening of Silicon Detectors, DESY-PROCEEDINGS-1998-02 (1998).

[33] G.C. Messenger, IEEE Trans. Nucl. Sci. 391 (1992) 468-473.

[34] V. Cindro, G. Kramberger, M. Mikuž, D. Žontar: *Readout of non irradiated and irradiated strip detectors with fast analogue electronic* presented at 8^{th} European Symposium on Semiconductor Detectors Jun, Schloss Elmau, Germany, 1998, to be published in Nucl. Instr. Meth.

[35] M. Moll et al.: *Leakage current of hadron irradiated silicon detectors - material dependence* (Presented at 2^{nd} International Conference on Radiation Effects on Semiconductor Materials, detectors and Devices, Florence 1998, submitted to Nucl. Instr. Meth.).

[36] E.S. Krištof, private communication

[37] J.J. Duderstadt,L.J. Hamilton: *Nuclear Reactor Analysis*, J. Wiley & Sons, 1976.

[38] M. Maučec, private communication

[39] V.F. Briemeister, Ed.: *MCNP - A General Monte Carlo N - Particle Transport Code*, Los Alamos National Lab. Report LA-12625-M (1997).

[40] R. Jeraj et al., Nucl. Technol. Vol. 120 (1997) 179.

[41] I. Mele et al., Nucl. Technol. Vol. 105 (1994) 37.

[42] M. Maučec: *Varnostna analiza kritičnosti bazenov za izrabljeno gorivo*, Magistrsko delo (1996).

[43] E.S. Krištof, *Characterization of Neutron Flux in the Exposure Channel F19 of the TRIGA Mark II Reactor in Ljubljana*, Presented at Nuclear Energy in Central Europe '98, Terme Čatež, Slovenia, 1998, to be published in conference proceedings.

[44] P. Griffin (SANDIA), data from ENDF/B-VI, unpublished,
A. Vasilescu, INPE Bucharest, Romania, private communication.

[45] H.J. Ziock et al., Nucl. Instr. Meth. A342 (1994) 96

[46] F. Lemeilleur et al., CERN-ECP/94-8 (1994).

[47] A. Ruzin et al: Presented at 2^{nd} International Conference on Radiation Effects on Semiconductor Materials, Detectors and Devices, Florence 1998, submitted to Nucl. Instr. Meth..

[48] G. Casse et al, 3^{rd} ROSE Workshop on Radiaton Hardening of Silicon Detectors, DESY-PROCEEDINGS.-1998-02 (1998).

[49] L. Beattie et al., 3^{rd} ROSE Workshop on Radiaton Hardening of Silicon Detectors, DESY-PROCEEDINGS-1998-02 (1998).

[50] M. Moll et al., 3^{rd} ROSE Workshop on Radiaton Hardening of Silicon Detectors, DESY-PROCEEDINGS-1998-02 (1998).

[51] P.Fischer et al., ATLAS Internal Note INDET-NO-086 (1994),
A. Brandl et al., CDF Internal Note CDF/DOC/SEC-VXT/PUBLIC/3512,
G. Gorfine et al., ATLAS Internal Note, INDET-No-139 (1996).

[52] B.G.Swensson et al., 2^{nd} ROSE Workshop on Radiaton Hardening of Silicon Detectors, CERN 1997, unpublished.

[53] Z. Li et al., IEEE Trans. Nucl. Sci. Vol. 42 (1995) 219

[54] M. Moll et al., Nuclear Phy. B 44 (1995) 468-474.

[55] V. Cindro, G. Kramberger, M. Mikuž, D. Žontar: *Bias-Dependent Annealing of Radiation Damage in Neutron-Irradiated Silicon p^+-n-n^+ diodes*, accepted for publication in Nucl. Instr. Meth..

[56] V. Cindro, G. Kramberger, M. Mikuž, D. Žontar: *Time Development and Flux Dependence of Neutron-Irradiation Induced Defects in Silicon Pad Detectors*, (Presented at 2^{nd} International Conference on Radiation Effects on Semiconductor Materials, detectors and Devices, Florence 1998, submitted to Nucl. Instr. Meth.).

[57] M. Huhtinen et al, HU-SEFT-R-1993-02 (1993)

Izjavljam, da je disertacija rezultat samostojnega raziskovalnega dela.

Dejan Žontar

Ljubljana, september 1998